THE EFFECT OF CLAY PARTICLES IN PORE WATER ON THE CRITICAL SHEAR STRESS OF SAND

By

KEVIN M. BARRY

A DISSERTATION PRESENTED TO THE GRADUATE SCHOOL
OF THE UNIVERSITY OF FLORIDA IN PARTIAL FULFILLMENT
OF THE REQUIREMENTS FOR THE DEGREE OF
DOCTOR OF PHILOSOPHY

UNIVERSITY OF FLORIDA

ACKNOWLEDGMENTS

First of all, I would like to express my gratitude to my advisor and committee chairman, Professor Ashish J. Mehta, for his continuous guidance and encouragement during my years of study in the Civil and Coastal Engineering Department at the University of Florida. This study has been a challenging experience in my life.

I also would like to express my appreciation to Professor Robert G. Dean, Professor Daniel M. Hanes, Professor Clay L. Montague, and Professor Robert J. Thieke for serving on my committee, for their advice, comments, and patience in reviewing this thesis.

Thanks to Becky Hudson for both her help and her kindness which helped directly and indirectly in the completion of this study. Deep appreciation goes to Viktor Adams, Jim E. Joiner, Vernon Sparks, and Sidney Schofield for their years of guidance, friendship, and assistance with experimentation at the Coastal Engineering Laboratory.

My final acknowledgement is reserved for my friends and family, especially my father, Heather N. Riegle, and my two sons, Brendan and Kieran. I deeply appreciate their years of love, support, and encouragement, without which I couldn't have accomplished any of this.

TABLE OF CONTENTS

page

ACKNOWLEDGMENTS ii

LIST OF TABLES v

LIST OF FIGURES vi

CHAPTER

1 INTRODUCTION 1

1.1 Problem Statement 1
1.2 Problem Approach 4
1.3 Outline of Chapters 5

2 LITERATURE REVIEW 7

2.1 Introduction 7
2.2 Einstein and El Samni (1949) 7
2.3 Benedict and Christensen (1972) 9
2.4 Christensen (1975) 9
2.5 Wiberg and Smith (1987) 13
2.6 Dade and Nowell (1991) 14
2.7 Dade et al. (1992) 15
2.8 Nalluri and Alvarez (1992) 17
2.9 Mehta and Lee (1994) 18
2.10 Mitchener and Torfs (1996) 20
2.11 Huygens and Verhoeven (1996) 21
2.12 Panagiotopolous et al. (1997) 22
2.13 Torfs et al. (2000) 24
2.14 Sharif (2002) 27

3 CRITICAL STRESS FOR SAND BED WITH INTERSTITIAL CLAY PARTICLES30

3.1 Introduction 30
3.2 Incipient Motion of Cohesionless Particles 30
3.3 Critical Stress of Cohesionless Sediment with Clay Particles in the Pore Water ... 32

4 EXPERIMENTAL SETUP AND PROCEDURES 48

4.1 Introduction 48
4.2 Flume 48
4.3 Simulator of Erosion Rate Function 52
4.4 Schulze Ring Shear Tester 55
4.5 Materials 58
4.6 Flume Calibration and Experimental Procedure 66
4.7 SERF Calibration and Experimental Procedure 68
4.8 Schulze Ring Shear Tester Calibration and Experimental Procedure 74

5 EXPERIMENTAL RESULTS 78

5.1 SERF Experiments 78
5.2 Flume Experiments 80
5.3 Schulze Shear Tester Experiments 92
5.4 Comparison of SERF and Flume Data 99

6 ANALYSIS OF RESULTS 102

6.1 Introduction 102
6.2 Quasi-Hydrodynamic Model for Sand Lubrication 104
6.3 Effect of Pore Water Salinity 118
6.4 Shear Resistance Model for Clay Lubrication 124
6.5 Comparison of Model Concepts 132

7 SUMMARY AND CONCLUSIONS 135

7.1 Summary 135
7.2 Conclusions 136
7.3 Recommendations for Future Work 138

LIST OF REFERENCES 141

BIOGRAPHICAL SKETCH 146

LIST OF TABLES

Table page

4.1 Composition of commercially prepared clays in order of predominance 60

5.1 SERF experimental conditions 78

5.2 Density, erosion rate constant, and shear strength values for 15 clay samples 79

5.3 Summary of flume experimental conditions 81

5.3 (continued) 82

5.4 Critical shear stress, Reynolds number, and critical Shields parameter for sand beds .. 85

5.5 Schulze Shear Tester experimental conditions 92

5.5 (continued) 93

5.5 (continued) 93

5.6 Schulze Shear Tester results for fresh kaolinite series 95

5.7 (continued) 96

5.8 Shulze Shear Tester results for saline kaolinite 96

6.1 Summarized data for τ_{co}, $\psi_{\min}$, τ_{cs}, and ψ_r 103

6.2 Comparison of model concepts 132

LIST OF FIGURES

Figure page

3.1 Force balance on a particle at the surface of a bed.. 34

3.2 Velocity as a function of non-dimensional height above the bed. Equation of Reichardt (1951)... 38

3.3 Turbulent time mean velocity distribution in proximity of rough bed, rough range. Profile of Christensen (1972). 40

3.4 Comparison of four velocity profiles with the data of Nikuradse (1933). 42

3.5 Comparison of profiles for critical bottom shear with the data of Shields (1936).......... 43

3.6 Relationship between the particle packing angle and the ratio of particle size to bed roughness scale, D/ks, where D is the grain diameter. In this representation the bottoms of the almost-moving grains are at the zero level of the bed, indicated by arrows at z = 0 (Wiberg and Smith, 1987). 45

3.7 Critical shear stress for erosion of kaolinit/sand and scheldt mud/sand mixtures versus fine grain weight fraction: data (Torfs, 1995). 47

3.8 Critical shear stress for erosion of Montmorillonite/sand mixture versus fine grain weight fraction: data (Torfs, 1995) 47

4.1 Schematic drawing of flume. 49

4.2 Kent propeller type current meter and its mount.. 51

4.3 Manometer and sampling locations.. 52

4.4 Schematic drawing of flume detailing sampling points and false bottom. 52

4.5 Schematic of SERF. 54

4.6 Front-view of SERF showing the rotating cylinder assembly, speed control panel (lower left) and digital readouts (lower right) for the torque cell and the load cell. 55

4.7 Schulze Ring Shear Tester. 56

4.8 Cross-sectional view of sample inside upper annular disk and lower annular tray. 56

4.10 Schematic of upper annular disk. 57

4.11 Fin schematic........ 57

4.12 Cumulative size distribution plot of Bennett Pottery Supply Clay #10. 60

4.13 Cumulative size distribution plot of Bennett Pottery Supply Clay #20. 61

4.14 Cumulative size distribution plot of Bennett Pottery Supply Clay #75. 61

4.15 Cumulative size distribution plot of Feldspar F 8-20 sand. 62

4.16 Cumulative size distribution plot of Feldspar sand sieved through a #20 screen. 62

4.17 Cumulative size distribution plot of Feldspar 20-30 sand........ 63

4.18 Cumulative size distribution plot of Feldspar sand sieved through a #30 screen. 63

4.19 Cumulative size distribution plot of Feldspar sand sieved through a #40 screen. 64

4.20 Picture of sand grains of Feldspar sand sieved through a #40 screen. 64

4.21 Picture of sand grains of Feldspar 20-30 sand. 65

4.23 Relationship for discharge calculation for gate height of 3.18 cm........ 67

4.24 Relationship for discharge calculation for gate height of 3.81 cm........ 67

4.25 Comparison of calculated and measured surface elevations for Run 20-1. 67

4.26 Comparison of calculated and measured surface elevations for Run 20-2. 68

4.27 Calibration curve for large aluminum cylinder (dia.=7.6 cm). 70

4.28 Calibration curve for medium aluminum cylinder (dia.=7.2 cm). 70

4.29 Calibration curve for small aluminum cylinder (dia.=6.8 cm)........ 71

4.30 Plot of the shear stresses with time illustrating the data collection process, and the corresponding yield locus........ 75

4.31 Yield locus. 77

5.1 Dimensionless erosion rate as a function of dimensionless shear stress for the clay samples run in SERF. 80

5.2 Erosion rate plot for Bennett Pottery Supply Clay #20........ 83

5.3 Erosion rate plot for Bennett Pottery Supply Clay #75 83

5.4 Erosion rate plot for Bennett Pottery Supply Clay #2 84

5.5 Comparison of critical Shields parameter of sand beds with the results of other researchers and with the Shields curve. 86

5.6 Plot of the behavior of the critical shear stress of the Feldspar F 8-20 and kaolinite with fresh pore water series of beds. 87

5.7 Plot of the behavior of the critical shear stress of the Feldspar F 20-30 and kaolinite with fresh pore water series of beds. 87

5.8 Plot of the behavior of the critical shear stress of the Feldspar F 20-30 and clay mixture #1 with 3 ppt. saline pore water series of beds. 88

5.9 Plot of the behavior of the critical shear stress of the Feldspar F 20-30 and clay mixture #2 with 3 ppt. saline pore water series of beds. 88

5.10 Plot of the behavior of the critical shear stress of the Feldspar F 20-30 and kaolinite with 3 ppt. saline pore water series of beds 89

5.11 Plot of the behavior of the critical shear stress of the Sand #2 and kaolinite with fresh pore water series of beds. 89

5.12 Variation of the normalized critical shear stress with fine weight fraction for three different sands. 90

5.13 Variation of the critical shear stress with fine weight fraction for 20-30 sand and different clays. 90

5.14 Comparison of the critical Shields parameter of sand beds with kaolinite calculated using Equation 3.3.34 compared with the results of Mehta and Partheniades (1979) and with the critical Shields parameter of sand beds without kaolinite calculated using Equation 3.3.17 91

5.15 Comparison plot of the shear stress at incipient flow, τ_c, for the Sand #2 with fresh kaolinite series of beds. 97

5.16 Plot of the friction factor at a consolidation stress of 1000 Pa as a function of ψ for the Sand #2 with saline kaolinite series of beds. 98

5.17 Comparison plot of the shear stress at incipient flow, τ_c, for the Sand #2 with saline kaolinite series of beds. 98

5.18 Plot of the friction factor at a consolidation stress of 1000 Pa as a function of ψ for the Sand #2 with saline kaolinite series of beds. 99

5.19 Comparison of values for shear strength for Clay #10. 100

5.20 Comparison of values for shear strength for Clay #20. 100

5.21 Comparison of values for shear strength for Clay #75. 101

5.22 Summary plot of the comparison of the shear strength values. 101

6.1 Schematic drawing of the effect of clay fraction on the critical shear stress for sand (Data of Sharif, 2002)... 102

6.2 Schematics of the layered flow of a clay film between the surfaces of two sand grains where δ_1 and δ_2 are the roughness of the two surfaces (Heshmat and Brewe, 1995). 104

6.3 Lubrication regimes... 106

6.4 Quasi-hydrodynamic model of sand lubrication film. 107

6.5 Slider bearing moving to right at speed *U* above stationary pad (a), and transformed to stationary block and pad moving to the left at speed *U* (b). 107

6.6 Flow of interstitial clay suspension viewed as slider bearing. 108

6.7 Plot of Equation 6.2.27 applied to the data of Heshmat and Brewe (1996)................... 115

6.8 Comparison plot of both series of kaolinite and 20-30 sand tests.................................. 115

6.9 Freshwater flocculation in pore water with edge-to-face contacts................................. 119

6.10 Saltwater flocculation with particle orientation approaching parallelism................... 119

6.11 Face-centered cubic unit cell... 121

6.12 Microscopic view of frictional resistance. 125

6.13 Sand grain arrangement for calculation of shear resistance example. 127

6.14 Plot comparing the results from the Schulze cell for the saline kaolinite and fresh kaolinite series of sand beds.. 131

7. 1 Stribeck Curve with new dimensionless parameter. 139

Abstract of Dissertation Presented to the Graduate School
of the University of Florida in Partial Fulfillment of the
Requirements for the Degree of Doctor of Philosophy

THE EFFECT OF CLAY PARTICLES ON THE CRITICAL SHEAR STRES OF SAND

By

Kevin M. Barry

May 2003

Chair: Dr. Ashish J. Mehta
Cochair: Dr. Robert G. Dean
Department: Department of Civil and Coastal Engineering

An equation for τ_{cr} of sand beds in the presence of interstitial clay particles was developed based on the balance of forces on a sand particle at the surface of the bed. The equation was applied to data collected from a series of laboratory flume experiments on medium sand beds in order to examine the variation of τ_{cr} with clay weight fraction ψ. A quasi-hydrodynamic model of interstitial clay flow, possessing some of the features of hydrodynamic lubrication, was developed to explain the experimental results through changes in the lubricating effect of the clay suspension between the sand grains as the clay fraction increased.

Based on the application of the equation for τ_{cr} to experimental data, insight was gained on the behavior of $\psi_{\min}$, the weight fraction at which the minimum τ_{cr} occurs at the point of maximum lubrication. It was shown that $\psi_{\min}$ was affected by the frictional resistance offered by the clay suspension and by pore water salinity, but not sand size.

For a bed of 0.83 mm sand to which kaolinite in fresh water was added in varying amounts, measurements yielded $\psi_{min} = 0.04$. This result was explained through ψ_{min} being the fine weight fraction at which the thickness of the clay layer is close to the size of sand grain asperities (~ 20 μm) at which a transition from thin-film to boundary layer lubrication occurs. It was thus shown that ψ_{min} is not the space-filling clay weight fraction as postulated by previous investigators.

The space-filling clay weight fraction was found to be ψ_r, the weight fraction at which the shear stress once again equals τ_{co}, and the point at which the sediment starts to be dominated by the cohesive component. For a bed of 0.83 mm sand to which kaolinite in fresh water was added in varying amounts, measurements yielded $\psi_r = 0.13$ which was found to be the point at which the pore volume not occupied by clay becomes negligible (< 1% of the total volume).

Through the application of a shear resistance model to the experimental data collected in a Schulze ring shear tester, it was concluded that the strongest lubricating effect occurred when the over-all confining stress was carried by both the sand matrix and the thin interstitial clay suspension.

The effect of salinity on τ_{cr} and ψ_{min} was explained through a change in flocculation and a consequent change in the number of edge-to-face, particle-particle contacts.

The two models for clay lubrication presented in this study gave differing values for ψ_{min}, and this discrepancy warrants further study. The quasi-hydrodynamic model for clay lubrication predicted a value for ψ_{min} for kaolinite of 0.04, and the shear resistance model for clay lubrication predicted a value for ψ_{min} for kaolinite of 0.01. A possible cause of this discrepancy is that while the dimensional analysis that leads to the Stribeck curve is reasonable for the "thick-film" lubrication regime where the grains are not in contact, it is quite possible that, in the lower region of the curve where the grain asperities become significant, other variables such as grain asperity size and the load carried by an individual grain might become contributing factors. Consequently, the application of normal loads over grains with differing asperities needs to be conducted to determine the effect of normal load on ψ_{min}.

CHAPTER 1
INTRODUCTION

1.1 Problem Statement

For a proper management of coastal and estuarine waters it is essential for engineers and scientists to accurately predict the movement of mixtures of cohesionless and cohesive material. There are reliable methods for predicting the erosion of sand, but not for mixed sediments. A practical problem one faces with sandy beds is that whereas engineers and scientists typically use the Shields' diagram to predict the critical shear stress for erosion, recent studies have shown that the presence of even small fractions of clay in the sandy bed can measurably alter the critical shear stress. For example, Mitchener and Torfs (1996) attempted to characterize the erosional behavior of mixed sediments in a way that could be used for predictive models and in so doing made some important observations:

(1) The critical shear stress for erosion increases when mud is added to sand, and also when sand is added to mud (mud is $< 62.5\ \mu m$). The addition of up to 50% sand to a mud bed can typically increase critical erosion shear stress by a factor of 2. Conversely, the addition of 30% mud to a sand bed can increase the critical shear stress by as much as a factor of 10.

(2) The addition of mud to sand significantly increases the critical erosion shear stress with a maximum value occurring at a sand content between 50% and 70% by weight (corresponding to a 30% to 50% mud content).

(3) The addition of mud to sand not only delays the onset of erosion by increasing the threshold conditions required for sediment motion, it also diminishes the erosion rates once this occurs. Similarly, the erosion rate of mud decreases with increasing sand content. The erosion rate of a mixed bed can be reduced by a factor of 10 if more than 20% sand is added to a mud bed.

The above findings were primarily descriptive in nature, but provided a very thorough characterization of the erosional behavior of sediment mixtures.

Panagiotopolous et al. (1997) looked at the erosion threshold (i.e., critical shear stress) of mixed sediment deposits under the action of unidirectional currents and attempted to establish the critical erosion conditions, in terms of near-bed current speed and bed shear stress necessary to erode each sediment mixture, and to examine the influence of clay content on the established erosion threshold conditions. The results suggested that the critical stress for erosion of a mixed bed increases with increased mud content. The authors argued that two regimes could be identified: one regime for mud content less than 30% and another for contents greater than 30%. Under steady flow conditions, a linear increase in the threshold shear stress occurred for low mud contents (< 30%). These observations agreed with the observation that a clay mineral content of 5-10% (by weight) is high enough to dominate sediment erodibility characteristics.

The authors applied the analysis of Wiberg and Smith (1997) to mixed sediment beds and used this application to suggest that at low mud contents (< 30%) the sand particles continue to be in contact with each other so that pivoting is the main mechanism of initiation of motion. However, they noted that mud fills the voids as the fine fraction is increased, and in particular the spaces on either side of the contact point of the two sand particles and that this results in slightly altering the pivoting characteristics and consequently the value of the internal friction angle. At higher mud content (> 30%), a matrix of clay particles is formed which incorporates the sand and silt grains at which point the individual sand particles are no longer in contact with each other and pivoting stops to be the main mechanism for initiation of motion. As a result, erosion is then controlled mainly by the resistance of the clay fraction.

Torfs et al. (2000) developed a formula for the critical stress for mixture erosion, τ_{cm}, and the rate of erosion of the fine fraction through a diagnostic evaluation using data on the erosion of selected clay/sand and mud/sand mixtures, and in so doing made some additional important observations:

(1) The critical shear stress of the mixture, τ_{cm}, was found to vary non-monotonically with the fine sediment weight fraction, ψ. Starting with a sandy bed, as ψ increased, at first τ_{cm} seemingly decreased from its value for sand and reached a minimum at a weight fraction $\psi_{\min}$, then increased.

(2) It appeared that $\psi_{\min}$, the fine grain weight fraction at which the minimum value of critical shear stress occurred, may be a measure of the space-filling concentration of fine particles within the pores of the sandy bed matrix.

(3) The logarithm of the rate of erosion was shown to vary linearly with the logarithm of the excess bed shear stress, and this variation depended on ψ.

(4) It was their opinion that the highly non-linear dependence of the critical shear stress on the fine-grained weight fraction was indicative of the interactive role of the mixture components in controlling erosion, and suggested a potential route for improvement in modeling erosion by accounting for these interactions. In that context, they considered

additional experimental observations on the erosion of mixtures in the vicinity of space-filling weight (or volume) fraction to be essential.

1.2 Problem Approach

It was the goal of this study to develop a physics-based explanation for the behavior of the critical shear stress of sand beds, τ_{cr}, in the presence of interstitial clay particles. As suggested by the previous works on this subject, there exists a definite trend in the behavior of sand beds containing pore water clay particles with fine fractions less than ~0.15. Starting with pure sand, as the weight fraction of clay in the pore water increases the critical shear stress decreases and reaches a minimum value at a characteristic weight fraction, then increases. This work has attempted to both further quantify and explain this behavior, so that the behavior of τ_{cr} could be predicted. This goal was accomplished by experimental observations on the erosion of sand beds in the vicinity of the aforementioned range of clay weight fraction.

To accomplish this goal, several tasks were completed. First, an expression, based on a force-balance for a sand grain at the surface of a bed, was developed for the critical shear stress of sand beds in the presence of interstitial clay particles, τ_{cr}, in the range of fine fraction, ψ, from 0.0 to 0.15.

Second, a narrow, unidirectional flow flume with a false bottom designed for emplacing sediments beds, was used to determine the relationship of the critical shear stress of the sand beds as a function of clay weight fraction. This flume was calibrated by comparing clay erosion data obtained in it with analogous data obtained in a cylindrical apparatus in which the shear stress on the bed could be measured directly.

Third, the expression for the critical shear stress of sand beds in the presence of interstitial clay particles was applied to the results from the flume tests to determine the effect of the fine grain fraction on the effective particle packing angle, Φ_{eff}.

Fourth, a quasi-hydrodynamic model of clay lubrication, a mechanism of interstitial clay flow which possesses some features of hydrodynamic lubrication, was developed to explain the interaction between sand grains and the fine fraction.

Fifth, a Schulze ring shear tester was modified for use with clays and then used to explain the behavior of τ_{cr} of sand at low values of ψ.

Finally, a shear resistance model, which relates to the nature of shear resistance between particles, was developed to explain the dependence of τ_{cr} on the fine grain fraction.

1.3 Outline of Chapters

This study is presented in the following order.

Chapter 2 is devoted to a discussion of an analytical and experimental background of subjects related to critical shear stress of non-cohesive sediments, cohesive sediments, and mixtures of the two.

Chapter 3 first defines incipient motion for both cohesionless and cohesive sediments, then develops an expression for incipient motion of cohesionless sediment, and finally presents in detail the derivation of an expression describing incipient motion of mixtures of both cohesive and non-cohesive sediment.

In Chapter 4, the experimental equipment, material, and procedures are discussed in detail.

In Chapter 5, the results for each of the three types of equipment used in this study are presented. This chapter is organized into a section for each device, with each section giving first a table of the results, plots if pertinent, and then an analysis of the results from that device.

In Chapter 6, the results from each of the three types of equipment used in this study are analyzed. This chapter is organized into three sections. The first two describe two different experimental models used, and the final section gives a comparison of these models.

In Chapter 7, conclusions from this study and recommendations for future research are presented.

CHAPTER 1
LITERATURE REVIEW

2.1 Introduction

Selected studies on the critical shear stress and erosion of cohesionless, cohesive and mixed cohesionless/cohesive soil beds are reviewed here in chronological order to provide the background for the mechanisms that underlie the physical processes germane to the present study.

2.2 Einstein and El Samni (1949)

The purpose of this study was to measure the drag and lift forces acting on particles in the surface layer of a bed. Spherical plastic balls, 6.9 cm in diameter, were used as the roughness elements in a recirculating, unidirectional flume. In order to prevent the seepage of water between these balls and the bottom of the flume, only the upper halves of the spheres were used by gluing the hemispheres in a hexagonal pattern to the bottom of the flume. The drag and lift components of the average dynamic forces on this rough surface were then measured.

Drag is the resultant force in the direction of velocity, and lift is the resultant force in the direction of the normal to velocity. These resultants of shear stress and pressure distributions can be obtained by integrating the effect of these two quantities on the body surface:

$$\begin{aligned} F_D &= \int P\cos\theta \, dA + \int \tau_w \sin\theta \, dA \\ F_L &= -\int P\sin\theta \, dA + \int \tau_w \cos\theta \, dA \end{aligned} \tag{2.1}$$

where F_D is the drag force, F_L is the lift force, τ_w is the shear stress along the bed, P = pressure at any point on the surface of the body, dA = differential element of surface area for the body, and θ is the angle to the tangent of the body surface. The lift and drag coefficients are defined as:

$$C_L = \frac{F_L}{\frac{1}{2}\rho_w U^2 A_x} \qquad C_D = \frac{F_D}{\frac{1}{2}\rho_w U^2 A_x} \tag{2.2}$$

In these, the two effects are considered together -- net drag is produced by both pressure and shear effects, and so is net lift. ρ_w = mass density of the fluid, U = average fluid velocity over the cross sectional area of the particle, and A_x = average cross sectional area of the particle. To determine C_L the measured pressure difference between flume side wall above the hemispheres and the flume floor between the hemispheres was described in the following form:

$$\Delta P = C_L \left(\frac{\rho_w}{2}\right) u_{0.35}^2 \tag{2.3}$$

where $u_{0.35}$ was measured 0.35 hemisphere diameters from the theoretical bed, assumed to be a distance of $0.2k_s$ below the plane tangent to the top of the spheres whose diameter was taken as k_s. The coefficient, C_L, was found to have a constant value of 0.178 when and only when the flow velocity was measured at a distance of 0.35 diameters from the theoretical bed.

To determine F_D, hence C_D, the investigators used a logarithmic velocity profile:

$$\frac{\bar{u}}{u_*} = C_2 + 5.75 \log\left(\frac{R}{k_s}\right) \qquad (2.4)$$

where $\bar{u}$ is the average velocity over the hydraulic radius R and C_2 is a constant. The friction velocity u_* was obtained from the above profile and then $\tau_b = \rho_w u_*^2$. This shear stress was then integrated over the entire bed. The results for the average shear stress matched previous results. The coefficient C_2 was found to have the value, 8.50, as previously determined by Keulegan (1938). Tests were also conducted of the applicability of Equation 2.4 to turbulent flow over a natural gravel bed. In these experiments, very close agreement was achieved if the roughness k_s was chosen to equal 6.1 cm.

2.3 Benedict and Christensen (1967)

The objective of this work was to develop a physical understanding of the lift force in the hydrodynamically rough range of flow. The investigators developed an analytical approach for the lift force on idealized beds composed of hemispheres. A potential flow solution was obtained for the bed and linked to the actual velocity profile over the bed to predict pressure and hence lift. The integration of the theoretical solution for the closely packed hemispheres yielded a value of $C_L = 0.259$.

2.4 Christensen (1975)

This work was meant to assign a probability of erosion to the critical shear stress of a cohesionless sediment bed. Bed scour is usually considered to begin when the local time-mean bed shear stress exceeds the critical shear stress of the bed material. This leads to the definition of the critical bed shear stress as the time-mean value of the shear stress when erosion is initiated. However, the forces that cause a grain to move are of a stochastic nature due to the turbulent flow. Therefore, it is possible to observe local bed failure due to an instantaneous velocity fluctuation causing these forces to exceed the failure condition when the time-mean bed shear stress is less than the critical shear stress. It is therefore appropriate to assign a probability of erosion to the critical shear stress.

The investigator started with the criterion for incipient motion of a grain,

$$\frac{|F_D|}{W_b - F_L} = \tan\varphi \tag{2.5}$$

where

$$F_D = \tau_b \alpha_1 d_e^2 \tag{2.6}$$

$$F_L = \lambda \alpha_1 d_e^2 \tag{2.7}$$

and

$$W_b = (\gamma_s - \gamma)\alpha_2 d_e^3 \tag{2.8}$$

in which F_D is the hydrodynamic drag force, F_L is the hydrodynamic lift force, W_b is the buoyant weight, γ_s is the specific weight of the sediment grain, γ is the specific weight of the fluid, φ is the angle of repose, τ_o is the instantaneous value of the fluctuating bed shear stress, and λ is the instantaneous value of the fluctuating lift per unit bed area; both τ_o and λ correspond to incipient motion. α_1 and α_2 are shape factors; the first is the bed area associated with one grain divided by the grain size squared and the other is the grain volume divided by the grain size cubed. It is important to note that drag force in Equation 2.5 is the absolute value because it is possible for the instantaneous flow to be from right to left even though the time-mean flow is from left to right. Consequently, two failure conditions need to be considered.

Equations 2.6, 2.7, and 2.8 were substituted into Equation 2.5 resulting in

$$|\tau_b| = \frac{\alpha_1}{\alpha_2} \cdot \frac{(\gamma_s - \gamma)\alpha_2 d_e}{\frac{\lambda}{|\tau_b|} + \cot\varphi} \tag{2.9}$$

The instantaneous lift to shear stress ratio was then replaced by the ratio of the corresponding time-mean values, since λ and τ_b both are proportional to the same instantaneous velocity squared. The absolute value of the instantaneous bed shear stress corresponding to incipient motion may be written

$$|\tau_b| = C_D \, \rho_w \frac{u^2}{2} \tag{2.10}$$

where C_D is assumed constant. The instantaneous velocity u is measured at the top of the grain, which, according to Einstein and El Samni (1949) is located at approximately $0.2d_e$ height above the theoretical bed. When the velocity u is expressed by its time-mean and fluctuating component, $\bar{u}$ and u', the corresponding absolute value of the bed shear stress becomes

$$|\tau_b| = \frac{\bar{\tau}_b}{1 + S_u^2} (1 + S_u \, n)^2 \tag{2.11}$$

with the time-mean value

$$\bar{\tau}_b = C_D \, \rho_w \frac{\bar{u}^2}{2} \left(1 + \left(\frac{\sigma_u}{\bar{u}} \right)^2 \right) \tag{2.12}$$

where S_u is the dimensionless value of the standard deviation of the velocity fluctuation σ_u, defined as $\sigma_u / \bar{u}$, and n is the normalized velocity fluctuation u'/σ_u.

An analogous treatment was done for the time-mean value of lift and substituted into Equation 2.9 along with Equation 2.11 to obtain

$$\frac{\bar{\tau}_b}{1+S_u^2}(1+nS_u)^2 = \frac{\alpha_2}{\alpha_1}\frac{(\gamma_s-\gamma)d_e}{\frac{\bar{\lambda}}{\bar{\tau}_b}+\cot\varphi} \tag{2.13}$$

From Equation 2.13 it is seen that the critical shear stress of a horizontal bed may be written

$$\bar{\tau}_{cr} = \frac{\alpha_2}{\alpha_1}\frac{(\gamma_s-\gamma)d_e}{\frac{\bar{\lambda}}{\bar{\tau}_b}+\cot\varphi}\frac{1+S_u^2}{(1+nS_u)^2} \tag{2.14}$$

The investigator then introduced an expression for the ratio of the time-mean values of lift and shear based on Einstein's (1943) observations to obtain an expression for critical shear stress

$$\bar{\tau}_{cr} = \theta_{cr}(\gamma_s - \gamma)d_e \tag{2.15}$$

where

$$\theta_{cr} = \frac{\alpha_2}{\alpha_1}\frac{1 + S_u^2}{\cot\varphi + 0.556\left[\ln\left(1 + \frac{10.4}{r}\right)\right]^2}\frac{1}{(1 + nS_u)^2} \tag{2.16}$$

The symbol *r* in Equation 2.16 is the roughness/grain-size ratio defined as the equivalent sand roughness k_s divided by the effective grain-size d_e.

Equations 2.15 and 2.16 were found to be in good agreement with most observations, with $S_u = 0.164$ and $n = 3.09$ corresponding to the probability or erosion *Pr* = 0.001 related to the Gaussian distribution of u'.

2.5 Wiberg and Smith (1988)

Expressions were derived for the critical shear stress for beds of both uniform and heterogeneous sediment under unidirectional flow. The investigators start by developing a relationship for the critical shear stress for a sediment particle at the surface of a uniform bed:

$$\tau_{cr} = \frac{2}{C_D \alpha_3} \cdot \frac{1}{\left\langle f^2\left(z/z_o \right) \right\rangle} \cdot \frac{\left(\tan\Phi \cos\theta_b - \sin\theta_b \right)}{\left[1 + \left(F_L/F_D \right)_{cr} \tan\Phi \right]} \qquad (2.17)$$

where α_3 is a parameter representing the geometry of the grain, $f^2(z/z_o)$ comes from the expressions for F_D and F_L and represents the cross-sectional averaged velocity profile function, z = height above the bed, z_o = bottom roughness parameter, Φ is the particle packing angle (or bed pocket geometry angle), a measure of the difficulty of moving a sediment grain up and out of the pocket in which it is resting, and θ_b is bed slope. The investigators use the following expression of Reichardt (1951) for the velocity profile, which provides a transition between the viscous sub-layer and the logarithmic flow above, and is in agreement with measurements (Schlichting, 1979):

$$u(z) = u_* \left[\frac{1}{\kappa} \ln\left(1 + \kappa z^+ \right) - c\left(1 - e^{-z^+ - 11.6} - \frac{z^+}{11.6} e^{-0.33 z^+} \right) \right] \qquad (2.18)$$

where $z^+ = u_* z_o / \nu = R_* z / k_s$, $z_o^+ = u_* z_o / \nu = R_* z_o / k_s$ and R_* is the roughness Reynolds number $R_* = u_* k_s / \nu$, where k_s is the scale length for the bed roughness. It should be noted that, with this expression, all of the terms in Equation 2.17 can be either measured or calculated with the exception of the particle packing angle, Φ.

The investigators then develop an expression for the critical shear stress for heterogeneous beds. They argue that there are two lengths scales for such beds while there is only one (the grain diameter) for homogeneous beds. The diameter of the particle size fraction of interest is the length scale for lift, drag, and gravity, specifically as it governs how far into the flow the grain protrudes. The flow velocity, however, also depends on the roughness scale k_s of the surrounding bed. The presence of these two length scales is primarily responsible for the difference between the computed critical shear stress for sediment on uniform versus heterogeneous beds. The investigators bridge this gap using an expression for Φ. They argue that the particle angle of repose changes for a bed composed of mixed sizes. For example, it is easier for a large grain to roll over a bed composed of smaller particles than for a small grain to roll over a bed of larger particles. This is indicated by an increase in the value of Φ as the ratio of grain diameter to bed roughness length, d/k_s, decreases. The investigators use an expression derived from the work of Miller and Byrne (1966):

$$\Phi = \cos^{-1}\left[\frac{d/k_s + z_*}{d/k_s + 1}\right] \tag{2.19}$$

where z_* is the average level of the bottom of the almost moving grain.

2.6 Dade and Nowell (1991)

It was the purpose of this work to develop an expression for critical bed shear stress using the force balance of Wiberg and Smith (1988), but substituting a term for the inter-particle cohesive force to obtain an equation for entrainment from flat cohesive mud beds:

$$\tau_{cr} = \frac{40\rho_w \upsilon^2}{\tan\Phi\, d^2}\left[\sqrt{\frac{g\rho_s' d^3}{\rho_w \upsilon^2}\frac{\tan^2\Phi}{240}\left(1+3(1-\cos\Phi)\frac{\tau_b}{g(\rho_s-\rho_w)d}\right)+1}\;-1\right] \quad (2.20)$$

where τ_b is the interfacial mud shear stress, ρ_s is the particle density, υ is the fluid kinematic viscosity, ρ_w is the fluid density, g is the acceleration due to gravity, and the average particle packing angle, Φ is 65°. Relative contributions of either particle cohesion or submerged weight to mud erosion resistance are embodied in the dimensionless term $\tau_b/(g\rho_s d)$.

2.7 Dade et al. (1992)

It was the purpose of this work to define the critical bed shear stress required to initiate particle-by-particle entrainment of cohesive sediment. The investigators start their development with a force balance similar to that of Wiberg and Smith (1988). The only difference is the inclusion of a net inter-particle force, F_A, which includes the effect of both cohesion and adhesion acting in the same direction as gravity. Their balance is

$$W_b + F_A = F_D \cot\Phi + F_L \quad (2.21)$$

where W_b is the immersed weight of the grain, and F_D and F_L are the drag and lift forces due to the overlying flow. This equation can be manipulated to take the form

$$\frac{F_D}{W_b} = \frac{\tan\Phi}{1+\frac{F_L}{F_D}\tan\Phi}\left(1+\frac{F_A}{W_b}\right) \tag{2.22}$$

It is important to note that the particle packing angle Φ, first proposed by Wiberg and Smith (1988), is analogous to a coefficient of static friction when the incipient force balance is expressed as it is in Equation 2.22. The modifications then proposed by the authors were an explicit inclusion of the cohesion term and appropriate expressions for F_D and F_L.

The investigators assume the mud bed component particles to be spheres that are small relative to the thickness of the near-bed viscous dominated region of overlying turbulent flows. Consequently, under these conditions flat beds of fine sediment are said to be hydrodynamically smooth and particle Reynolds number is around unity. Turbulent stress then makes up only a fraction of total near-bed stress. The resulting near-viscous flow exhibits a relatively constant, linear velocity profile. Under these conditions it is appropriate then to use existing expressions for F_D and F_L acting on spheroidal particles. These expressions are substituted into Equation 2.22. Ultimately the following relation for θ_{cr}, the Shields parameter, is obtained:

$$\theta_{cr} = \frac{1}{\Xi}\left[\frac{5\mathrm{X}}{\tan\Phi}\,\frac{\sqrt{\frac{4}{\mathrm{X}}-3}-1}{1-\mathrm{X}}\right]^2 \tag{2.23}$$

where

$$\Xi = \frac{g\left(\rho_s-\rho_w\right)d_n^3}{\rho_w \upsilon^2} \tag{2.24}$$

and

$$\mathrm{X} = \Xi\left(1 + \frac{F_A}{W_b}\right)\frac{\pi}{4800 b_1}\tan^3\Phi \tag{2.25}$$

where b_1 a shape factor relating viscous forces acting on actual spherical particles to that acting on nominal spheres, d_n is the nominal spherical particle diameter, and Ξ is referred to as the Yalin (1972) parameter which is a dimensionless submerged-particle weight. Thus the critical shear stress is a function of submerged weight and shape of bed-component particles, relative particle protrusion (embodied in tanΦ), and cohesion relative to submerged particle weight (F_A/W_b). This ratio is obtained from

$$\frac{F_A}{W_b} = 3b_2(1 - \cos\Phi)\frac{\tau_y}{g(\rho_s - \rho_w)d_n} \tag{2.26}$$

where b_2 is a shape factor that adjusts the ratio of particle surface area-to-volume as a function of platy-ness.

The strength of this approach lies in its attempt to extend non-cohesive sediment transport theory to mud beds by including an additional parameter for adhesion/cohesion force F_A in a standard force balance. Calculations were found to be in good agreement with the observations of Migniot (1968) and Ohtsubo and Muraoka (1986).

2.8 Nalluri and Alvarez (1992)

The objective of this work was to identify the influence of cohesive additives to the erosion threshold of non-cohesive sediments. The investigators conducted experiments using both a pipe-flow and a unidirectional flume.

They started with a determination of the frictional properties of both flow systems. Once both systems were calibrated, they prepared sand beds in both systems and compared the mean friction coefficients (f_m) with the bed friction coefficients (f_b) computed by the Einstein-Vanoni's separation technique (Vanoni and Brooks, 1957). Tests were then run to determine the influence of additives such as china clay, oil, and petroleum jelly.

Based on a rheological study of sewer sediments, the investigators used the following test ranges:

Concentration of laponite clay gel: 18 - 40 g/l
Sand/clay gel ratio: 0 - 100% by weight
Sand sizes (d_{50}): 0.12 - 2.9 mm

The study led to the following main conclusions:

1. Even a low level of cohesion can increase the critical shear stress significantly when compared with equivalent non-cohesive sediments.
2. The size of sand has no significant effect on the critical shear stress of cohesive sediment.
3. For a given sand mixed with a given laponite concentration, there was an optimum sand to clay gel ratio for which a maximum resistance to erosion was obtained.

2.9 Mehta and Lee (1994)

In this study, the threshold condition for the incipient transport of cohesionless grains was linked to cohesive particles. The investigators start by stating the well-known condition for incipient transport

$$\tan\varphi = \frac{F_D}{W_b + F_c - F_L} \tag{2.27}$$

where F_D represents the hydrodynamic drag force acting on a grain, W_b is the buoyant weight of the grain, F_L is the hydrodynamic lift force acting on a grain, and F_c is the active cohesive force. Therefore, given τ_{cr} is equal to the threshold or critical bed shear,

d is a representative grain size, α_1 is an area shape factor, α_2 is equal to $\alpha_1 C_l/C_D$, where C_L and C_D are the lift and drag coefficients, we have $F_D = \alpha_1 t_{cs} d^2$, and $F_L = \alpha_2 t_{cs} d^2$. The buoyant weight, $W = \alpha_3 g(\rho_{sf}-\rho_w)d^3$, where α_3 is a volumetric shape factor, g is the acceleration due to gravity, ρ_{sf} is the grain (or floc) density, and ρ_w is the fluid (water) density. Substituting for these quantities in Equation 2.27, the following relationship is obtained:

$$\frac{\tau_{cr}}{g(\rho_{sf}-\rho_w)d} = \frac{\alpha_3 \tan\varphi}{(\alpha_1+\alpha_2\tan\varphi)} + \frac{F_c \tan\varphi(\alpha_1+\alpha_2\tan\varphi)}{g(\rho_{sf}-\rho_w)d^3} \qquad (2.28)$$

where the term on the left hand side is Shields' parameter, ψ, representing the ratio of drag force to buoyancy. The first term on the right hand side is seen to be a sediment-dependent parameter, and the second term is essentially the ratio of cohesive force to buoyancy. When cohesion is unimportant then, this term is essentially zero and Equation 2.28 becomes a representation of Shields' entrainment relationship for coarse sediment.

Further, it is evident from Equation 2.28 that Shields' relationship is not applicable to situations involving flocculated sediments, and there is further implication that extrapolation of this relationship into the cohesive size range can not be achieved unequivocally without including some measure of cohesion as a behavior-governing parameter.

The investigators point out that an evaluation of several previous laboratory studies suggests that τ_s reasonably correlates with the solids volume fraction ϕ_a. In general,

$$\tau_s = \alpha_4 \left(\phi_a - \phi_{ac}\right)^{\beta} \tag{2.29}$$

where ϕ_{ac} is the critical solids volume fraction such that for all $\phi_a < \phi_{ac}$ the soil does not possess a measurable structural integrity (even though it does have cohesion), and is thus not a bed but is essentially a fluid-supported slurry. The coefficients α_4 and β depend on sediment-specific properties.

The investigators also point out that it should be recognized: (1) for cohesionless soils the threshold condition for transport is specified by a particular value of the applied stress that causes the grain on the bed surface to be entrained, and (2) the threshold condition for a cohesive soil bed occurs when the applied stress equals the shear strength, associated with the bed surface flocs. In the latter case the floc is detached from its neighbors, to which it is otherwise linked by cohesion, and is entrained.

2.10 Mitchener and Torfs (1996)

The paper describes the results on the erosion of sediment mixtures of sand and mud based on laboratory and field tests. The investigators used the following expression to calculate the erosion rate for each shear stress step:

$$\frac{dm}{dt} = m_c \left(\tau_b - \tau_{cr}\right) \tag{2.30}$$

where dm/dt is the rate of change of suspended sediment mass, m_c is the erosion constant, τ_b is the applied bottom shear stress, and τ_{cr} is the critical shear stress for erosion. The following are the main conclusions of this study:

1. The critical shear stress for erosion increases when mud is added to sand, and consequently the onset of erosion is delayed. The authors found that the addition

of 30% mud to a sand bed can increase the critical shear stress by as much as a factor of 10.

2. The addition of mud to sand diminishes the erosion rates once sediment movement does occur.
3. The results in this work agree with the theory of Dade and Nowell (1991) and indicate that the transition from cohesionless to cohesive erosion occurs between 3% to 15% mud by weight. Consequently, cohesive type sediment transport equations should be used where the sediment bed contains more than 15% mud by weight.

2.11 Huygens and Verhoeven (1996)

It was the aim of these experiments to examine similarities and differences in the behavior of mixtures of cohesionless and cohesive sediment, in relation to the well-established cohesionless sediment transport approach.

Using well-known non-cohesive sediment transport experiments as a starting point for research of partly cohesive material, the investigators conducted a series of experiments in a straight semi-cylindrical flume which was 11.2 m long and had an inner diameter of 390 mm. The inner wall was covered with a sand paper whose wall roughness was evaluated to be $k_s = 0.54$ mm.

In all the tests sediment mixtures of four basic materials were used: two non-cohesive materials (a fine white sand and a medium beach sand) and two cohesive materials (kaolinite and montmorillonite). To calculate the bed shear stress, the investigators used the Vanoni-Brooks technique for removing the effect of the side walls of the flume (Huygens and Tito, 1994). Using this technique, it was found that the critical shear stresses corresponding to the incipient motion of the pure sand beds was compatible with the traditional Shields values. The critical bed shear stress of the partly cohesive sediment mixtures varied linearly with the clay content up to a clay content of 30%. For sediment mixtures with clay content greater than 30%, a slight decrease of the critical bed shear was noticed. The investigators noted that the cohesive clay particles cause a significant increase in the resistance to erosion.

In an effort to quantify the bed load transport of mixtures, the investigators developed an expression for the bed load transport of partly cohesive mixtures that was analogous to well-known formula for cohesionless sediment previously found to be successful (Einstein, 1943; Ackers-White, 1993; Van Rijn, 1984). They determined the bed load transport of non-cohesive and partly cohesive sediment to be related to the dimensionless bed shear stress τ_{b*}, the dimensionless Chézy coefficient C_{b*}, and the dimensionless unit stream power US_f / u_*, where u_* is the critical shear velocity obtained from the Shields diagram for pure sand but varies with clay content for mixtures, U is the mean flow velocity and S_f is the energy slope. They found a general bed load transport calculation that covered all mixtures to be

$$\phi_t = 0.002 \tau_{b*}^{1.67} C_b^{0.95} \left(\frac{US_f}{u_*} \right) \tag{2.31}$$

where the dimensionless bed shear stress is given by

$$\tau_{b*} = \frac{\tau_b}{g(\rho_s - \rho)d_{50}} \tag{2.32}$$

and the dimensionless Chézy coefficient is given by

$$C_{b*} = \frac{C_b}{\sqrt{g}} \tag{2.33}$$

2.12 Panagiotopolous et al. (1997)

The objective of this study was to establish the critical erosion condition necessary to erode a sediment mixture, and to examine the influence of clay content on the erosion threshold.

The sediments were tested in a recirculating flume (5.00 m long, 0.30 m wide and 0.45 m deep) with an open top and glass-sided walls. A video camera system was used to observe and record critical erosion condition. Time-averaged (2 min) current speeds at threshold were obtained 0.4 cm above the bed using a laser-Doppler velocimeter operated at a sampling frequency of 20 Hz and measuring velocities to within plus or minus 0.2 cm/s.

The sand component of the examined soils was angular, fine-grained with d_{50} equal to 153 and 215 □m. The cohesive component was Combwich mud, a natural estuarine silt-clay. The two sands were mixed separately with various proportions of Combwich mud.

Two series of experiments were conducted in unidirectional flow, referred to as set 1 and set 2. In set 1 the erodibility of 14 sediment deposits was examined. The threshold condition was reached within 2 min. of increasing the flow from zero. Following each test the water content of the mixture was determined. In set 2 the sediment samples were first subjected to various pre-threshold flow speeds (70%, 80%, and 90% of the critical values defined by set 1), over different times (5 min, 10, and 20 min) and then tested like set 1. These experiments focused on examining the erosion of the sediment beds, after the samples were exposed to current-induced shear stresses at values lower than the critical one.

The results suggest that the critical stress for erosion of a mixed bed increases with increasing mud content. Overall, two regimes can be identified: one for mud content less than 30% (clay mineral content 10%), and another for greater than 30%. For mud contents < 30%, under a steady flow a slight linear increase in the critical stress occurs. For mud contents > 30%, the resistance to erodibility increases significantly, once the mud content exceeds 30%. These observations agree with earlier findings (Dyer, 1986; Raudkivi, 1990) that a clay mineral content of 5-10% is high enough to dominate sediment erodibility.

In tests on the erosion of the mixtures after the samples were exposed to current-induced shear stresses at values lower than the critical one, it was found that the critical stress increased with increased pre-threshold speed. This is to be expected because the bed becomes more compact and resistant to erosion as the sub-threshold velocity is increased. Grains or aggregates that do not satisfy the threshold criterion adjust to more stable positions within the bed.

2.13 Torfs et al. (2000)

The objective of this work was to a develop formula for the critical stress for mixture erosion, τ_{cm}. Following the work of Mehta and Lee (1994) reviewed in Section 2.9, the investigators noted that Equation 2.28 is strictly applicable to erosion of a bed of single-sized grains, even as it allows this size to vary from fine to coarse. When fine grain aggregates occur in a mixture with coarse grains, the interpretation of this equation becomes complex, especially because the two particle populations, having different sizes, densities and cohesion (equal to zero for coarse grains), do not necessarily entrain at the same rate.

Therefore, the investigators assume that the entrainment of this fine/coarse mixture can be characterized by size, d_m, and granular density, ρ_{sm}, the latter being an indirect measure and approximate substitute for fine sediment aggregate density. For the composite (mixture) bed, the corresponding angle of repose will be φ_m, and the critical stress, τ_{cm}. Further, for fine grains, F_c must be replaced by a composite force, F_m, which depends not only on cohesion, but also on the influence of the inter-bedded coarse grains. Such an influence can either enhance the effect of cohesion, e.g., by a "hiding," or sheltering effect, or reduce cohesion by decreasing inter-particle bonding. Thus, the investigators consider $F_m = KF_c$, where K depends on bed composition. Hence, Equation 2.28 becomes

$$\frac{\tau_{cm}}{g(\rho_{sm}-\rho_w)d_m} = \frac{\alpha_3 \tan\varphi_m}{(\alpha_1+\alpha_2\tan\varphi_m)} + \frac{KF\tan\varphi_m/(\alpha_1+\alpha_2\tan\varphi_m)}{g(\rho_{sm}-\rho_w)d_m^3} \tag{2.34}$$

in which α_1, α_2 and α_3 now relate to d_m. For a uniform, cohesive bed K=1, and the first term on the right hand side loses meaning because, as noted, φ_m is not definable for such a bed. Accordingly, equating τ_{cm} with the bed shear strength against erosion, τ_s (Parchure and Mehta, 1985), from Equation 2.34 we obtain

$$\tau_s = \frac{K_1 F}{d_{ag}^2} \tag{2.35}$$

where K_1 is a lumped, sediment-specific parameter and d_{ag} is the aggregate diameter. An analysis of cohesive bed erosion experiments has yielded the following relation (Mehta and Parchure, 2000):

$$\tau_s = \zeta(\phi_v - \phi_{vc})^{\xi} \tag{2.36}$$

in which ϕ_{vc} is the fine solids volume fraction obtained by dividing the dry density of solids, i.e., sediment dry weight per unit volume of fine sediment-water mixture, by the granular density of the fine particles. The quantity ϕ_v is the "threshold" value of ϕ_v below which the bed matrix is not fully particle-supported and is therefore fluid-like, and ζ and ξ are coefficients which depend on bed composition and the degree of consolidation. From Equations 2.35 and 2.36 we obtain

$$F = \frac{\zeta d_{ag}^2}{K_1}(\phi_v - \phi_{vc})^{\xi} \tag{2.37}$$

Hence, (2.34) can be restated as

$$\begin{aligned} \frac{\tau_{cm}}{g(\rho_{sm} - \rho)d_m} &= \frac{\alpha_3 \tan\phi_m}{(\alpha_1 + \alpha_2 \tan\phi_m)} \\ &+ \frac{K \tan\phi_m / (\alpha_1 + \alpha_2 \tan\phi_m)}{K_1} \frac{d_{ag}^2}{g(\rho_{sm} - \rho)d_m^3} \zeta(\phi_v - \phi_{vc})^{\xi} \end{aligned} \tag{2.38}$$

Equation 2.38 can be simplified by recognizing that the first term on the right hand side is coarse grain dominated, while the second term is dominated by the fine constituent. Therefore, in the first term the subscript, *cg*, implies coarse grain dominance. As for the second term the ratio, $K \tan\phi_m / (\alpha_1 + \alpha_2 \tan\phi_m)K_1$, will be considered to be a bed dependent characteristic coefficient, K'. Then, (2.38) can be restated as

$$\tau_{cm} = \left[\frac{\alpha_{3cg} \tan \phi_{cg}}{(\alpha_{1cg} + \alpha_{2cg} \tan \phi_{cg})} + \frac{K'\zeta(\phi_v - \phi_{vc})^{\xi}}{g(\rho_{sm} - \rho)d_m} \right] g(\rho_{sm} - \rho)d_m \qquad (2.39)$$

where the authors have also invoked the assumption, $d_{ag} \approx d_m$. In (2.39), $K'=0$ implies the absence of fine material, and increasing K' signifies increasing modulation of the critical stress for erosion of coarse material by fines.

Equation 2.39 is significant because it points to the interactive role of the mixture components in controlling erosion, and through the parameter K' suggests a potential approach for both improving the modeling of erosion of sediment mixtures and explaining the observed behavior. Consequently, the authors suggest additional experimentation on the erosion of mixtures in the vicinity of space-filling volume fraction.

2.14 Sharif (2002)

The objective of this work was to develop a model for the critical shear stress for the erosion of cohesive soils. The author's model included a relation for critical shear stress of pure cohesive soils, a relation for critical shear stress of mixed cohesive/non-cohesive soils with low clay content, and a relation for critical shear stress of mixed cohesive/non-cohesive soils with high clay content.

The relation for critical shear stress of mixed cohesive/non-cohesive soils with low clay content was based on a force balance on a single non-cohesive particle similar to Equation 2.27 and resulted in the following expression for τ_{cn}, the critical shear stress for a non-cohesive particle in a cohesive bed

$$\tau_{cn} = g(\rho_{sn} - \rho)d_n\theta + \frac{18\alpha_{sn}\xi_n\theta}{\alpha_{vc}\alpha_{vn}\pi d_n d_c^2 \rho^2 \rho_{sc}}\left(\frac{f_c\rho_d\rho_{sn}}{(\rho_{sn} - f_n\rho_d)}\right)^3 \tag{2. 40}$$

where ρ_{sn} is the granular density of the non-cohesive sediment grain, ρ_{sc} is the granular density of the fine cohesive particles, d_{nc} is the diameter of the non-cohesive particle, f_c is the weight fraction of fine cohesive particles, f_n is the weight fraction of non-cohesive particles, ρ_d is the bulk density of the bed, ξ_n is the magnitude of the force associated with the bonds between a fine cohesive particle and a non-cohesive particle, θ is the Shields parameter, d_c is the average diameter of fine cohesive particles, α_{vc} and α_{vn} are volumetric shape factors for fine cohesive particles and non-cohesive particles respectively, and α_{sn} is as area shape factor for non-cohesive particles.

The relation for the critical shear stress for erosion of pure cohesive soils was based on a force balance for the separation of the aggregates at the surface of the bed from the bed itself. This force balance ultimately resulted in the following expression for τ_{ca}, the critical shear stress for a pure cohesive bed, as a function of aggregate density

$$\tau_{ca} = \frac{k_1 g\theta_a}{(\rho_{ag} - \rho)^{k_2 - 1}} + \frac{18\rho_{ag}\theta_a\xi_a}{\pi\alpha_{vc}d_c^2\rho_{sc}} \tag{2.41}$$

where ρ_{ag} is the granular density of the aggregates, ξ_a is the magnitude of the average force associated with the bonds between two fine cohesive particles, θ_a is the Shields parameter for cohesive aggregates estimated from the Shields diagram, and k_1 and k_2 are coefficients from the following relation for floc diameter, d_a, as a function of floc density

$$d_a = \frac{k_1}{(\rho_a - \rho)^{k_2}} \tag{2.42}$$

The relation for critical shear stress for erosion of mixed cohesive/non-cohesive soils with high clay content was based on the presumption that the critical shear is governed by the critical shear stress of the non-cohesive particles and the critical shear stress of the aggregates, and the degree by which these two different critical shear stresses influence the bed shear stress overall. The author made the assumption that the degree of impact of each critical stress type depended on the average area at the plane of failure covered by each type of material (cohesive or non-cohesive). Using this assumption, the author arrive at the following expression for τ_{ch}, the overall critical shear stress of the mixed cohesive/non-cohesive beds with high clay content

$$\tau_{ch} = \tau_{cn} W_n + \tau_{ca} W_a \tag{2.43}$$

where W_n and W_a are weighting factors representing the contribution of the critical shear stress of non-cohesive particles and cohesive aggregates, respectively, to the overall critical shear stress of the bed. W_n and W_a are defined as follows

$$W_n = A_{nb}^{b_n} \tag{2.44}$$

$$W_a = A_{ab}^{b_a} \tag{2.45}$$

where A_{nb} is the specific area of the non-cohesive particles, A_{ab} is the specific area of the aggregates, and b_n and b_a are experimentally determined coefficients.

After applying the model for low clay concentrations and analyzing the results, the author made the following important conclusion: the critical shear stress for erosion of mixed cohesive/non-cohesive soils with low clay content is influenced solely by the forces acting on the non-cohesive particles and that this was the case up to the clay content associated with the maximum critical shear stress.

CHAPTER 3
CRITICAL STRESS FOR SAND BED WITH INTERSTITIAL CLAY PARTICLES

3.1 Introduction

An expression for the critical stress of sand in the presence of clay particles in pore water is developed in this chapter. To begin with, the incipient motion for cohesionless grains is defined and an expression for the critical stress of cohesionless sediment is developed.

3.2 Incipient Motion of Cohesionless Particles

Shields (1936) defined the critical condition as the point at which zero sediment transport occurs. In other words, the critical condition is the point of maximum stress at which no sediment transport occurs, therefore allowing for weak sediment movement but no mass transport of particles. Kramer's (1935) definition of weak movement seems to correspond to Shields' critical condition, where it is understood that with weak movement a few of the smallest sand particles are in motion in isolated spots. Vanoni (1946) advanced a criterion for incipient motion by counting the number of bursts per second; critical is defined with the burst frequency of 1/3 to 1 bursts per second. Sutherland (1967) found that near the threshold on a flat bed, motion was restricted to isolated spots with a small number of grains moving briefly a few centimeters. Bursts of motion occurred from positions all over the bed with frequencies that appeared to be constant from one location to another. Sutherland connected the intermittent movement with penetration of eddies into the viscous sublayer.

Given the above observations it is necessary to explain the formal use of "incipient motion" in relation to "incipient transport." From the work on incipient motion done to date, the first term is most frequently used to describe the instantaneous state at which a solid moves. This definition, while concise, may still lead to ambiguities between the work of one researcher and the work of another. For example, it does not follow that once surface solids have moved in a particular area of the bed, that they will continue to do so, since the condition of "armoring" may occur (Mantz, 1977). It also does not follow that when an individual grain or small grouping of surface solids is moving at one location, that others will be moving at a different location, due to the stochastic nature of the properties of both the flow and the bed. A time and spatially averaged critical stress which determines the fluid condition for incipient motion need not, therefore, be that which describes the initial continuous motion of solids, or incipient transport.

Defining incipient motion using average flow properties tends to over-simplify the entrainment process in light of the stochastic nature of turbulent flow. In that regard, Christensen (1972) and others have shown that, due to the randomness of the velocity fluctuations, the instantaneous bed shear stress, tb, may be related to a time-mean value of the shear stress, $\bar{\tau}_{cr}$, when the probability of erosion, i.e., the probability that the instantaneous shear stress exceeds $\bar{\tau}_{cr}$, is prescribed. Christensen (1972) proposed the following equation:

$$\frac{\tau_b}{\overline{\tau}_{cr}} = \left(\frac{\overline{u} + u'}{\overline{u}}\right)^2 = \left(1 + \frac{\sigma_u}{\overline{u}} \cdot n\right)^2 \qquad (3.2.1)$$

in which u' is the instantaneous value of the velocity fluctuation, $\overline{u}$ is the average value of the velocity, σ_u is the standard deviation of u', and $n = u'/\sigma_u$. Using Einstein and El Samni's (1949) observations of the fluctuating lift, Christensen (1965) demonstrated that the velocity fluctuations are normally distributed near the bed and that $\sigma_u/\overline{u}$ must be constant and equal to 0.16, i.e., a value that is in good agreement with direct observations (e.g., Reichardt, 1938). Consequently, n may be found from the table of the Gaussian probability integral when the probability of exceeding τ_b, and thereby risking erosion, is decided. Christensen and Bush (1971) showed that good agreement with observations of the critical shear stress, $\overline{\tau}_{cr}$, may be obtained if this probability is 0.001 corresponding to an n value of 3.09. Hence, since sediment erosion rate tends to increase rapidly with the average bed shear stress in slight-to-moderate excess of calculated critical values, the definition of a critical shear stress using time-averaged flow properties ($\overline{\tau}_{cr}$) remains useful for sediment transport modeling.

3.3 Critical Stress of Cohesionless Sediment with Clay Particles in the Pore Water

Consider a planar stationary bed of cohesionless particles subjected to unidirectional turbulent flow. It is assumed the flow and bed are statistically in a steady state. As soon as the fluid starts to flow, hydrodynamic forces are exerted on the particles, and with an increase of the flow velocity a condition is eventually reached where the particles at the surface of the bed are unable to resist the forces and, as a result, the first grain get dislodged and moves. This condition of incipient motion is defined by

$$\tan\varphi = \frac{F_t}{F_n} \tag{3.3.1}$$

where F_t and F_n are the instantaneous forces parallel and normal to the angle of repose, j. F_t and F_n are resultants of the hydrodynamic drag F_D, the lift force F_L, and the submerged weight W_b. Substituting in these forces, Equation 3.3.1 becomes

$$\tan\varphi = \frac{W_b \sin\theta_b + |F_D|}{W_b \cos\theta_b - F_L} \tag{3.3.2}$$

where the angle θ_b is the inclination of the bed from the horizontal at which incipient sediment motion takes place. Consequently,

$$|F_D| = \frac{W_b(\tan\Phi\cos\theta_b - \sin\theta_b)}{1 + \frac{F_L}{F_D}\tan\Phi} \tag{3.3.3}$$

where the particle packing angle (or bed pocket geometry angle), Φ, is substituted for the angle of repose, φ, following Wiberg and Smith (1987). Figure 3.1 illustrates the force balance. The bed pocket geometry angle is a measure of the difficulty of moving a sediment grain up and out of the pocket in which it is resting. The instantaneous drag force, the instantaneous lift force, and the buoyant weight are all expressed as follows:

$$F_L = \lambda\alpha_1 d^2 \tag{3.3.4}$$

$$F_D = \tau_b\alpha_1 d^2 \tag{3.3.5}$$

$$W_b = \alpha_2(\gamma_s - \gamma)d^3 \tag{3.3.6}$$

where α_1 is a shape factor representing the cross-sectional area of the grain, α_2 is a shape factor representing the volume of the grain, λ is the value of the instantaneous lift force per unit area, τ_b is the value of the instantaneous shear stress, γ_s is the unit weight of the

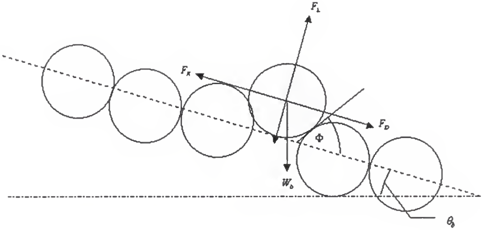

Figure 3.1 Force balance on a particle at the surface of a bed.

sediment, γ is the unit weight of water, and d is the grain size. Substituting into Equation 3.3.3 gives

$$|\tau_{cr}| = \frac{\alpha_2}{\alpha_1}\frac{(\gamma_s - \gamma)d(\tan\Phi\cos\theta_b - \sin\theta_b)}{1 + \frac{\lambda}{\tau_b}\tan\Phi} \tag{3.3.7}$$

This is the instantaneous bed shear stress at which failure is about to occur for surface particles on a bed with a sloping angle of θ_b. Following Christensen (1972) we will define τ_{cr} as

$$|\tau_{cr}| = C_D\rho\frac{u^2}{2} = C_D\rho\frac{1}{2}(\bar{u} + u')^2 = C_D\rho\frac{\bar{u}^2}{2}\left(1 + \frac{\sigma_u}{\bar{u}}\cdot\frac{u'}{\sigma_u}\right)^2 \tag{3.3.8}$$

where $\bar{u}$ is the time-averaged velocity, u' is the instantaneous fluctuation of velocity, and σ_u is the standard deviation of the instantaneous velocity fluctuations. Consequently,

$$\bar{\tau}_{cr} = C_D \rho \frac{\bar{u}^2}{2} \overline{\left(1 + \frac{\sigma_u}{\bar{u}} \cdot \frac{u'}{\sigma_u}\right)^2} = C_D \rho \frac{\bar{u}^2}{2}\left[1 + \left(\frac{\sigma_u}{\bar{u}}\right)^2\right] \tag{3.3.9}$$

$$\frac{|\tau_{cr}|}{\bar{\tau}_{cr}} = \frac{C_D \rho \frac{\bar{u}^2}{2}\left(1 + \frac{\sigma_u}{\bar{u}} \cdot \frac{u'}{\sigma_u}\right)^2}{C_D \rho \frac{\bar{u}^2}{2}\left[1 + \left(\frac{\sigma_u}{\bar{u}}\right)^2\right]} = \frac{\left(1 + \frac{\sigma_u}{\bar{u}} \cdot \frac{u'}{\sigma_u}\right)^2}{1 + \left(\frac{\sigma_u}{\bar{u}}\right)^2} = \frac{(1 + S_u n)^2}{1 + S_u^2} \tag{3.3.10}$$

where $S_u = \sigma_u / \bar{u}$ and $n = u'/\sigma_u$. Therefore,

$$|\tau_{cr}| = \bar{\tau}_{cr}\, \frac{(1 + S_u n)^2}{1 + S_u^2} \tag{3.3.11}$$

Equivalently,

$$|\lambda| = C_L \rho \frac{u^2}{2} = C_L \rho \frac{1}{2}(\bar{u} + u')^2 = C_L \rho \frac{\bar{u}^2}{2}\left(1 + \frac{\sigma_u}{\bar{u}} \cdot \frac{u'}{\sigma_u}\right) \tag{3.3.12}$$

$$\bar{\lambda} = C_L \rho \frac{\bar{u}^2}{2} \overline{\left(1 + \frac{\sigma_u}{\bar{u}} \cdot \frac{u'}{\sigma_u}\right)^2} = C_L \rho \frac{\bar{u}^2}{2}\left[1 + \left(\frac{\sigma_u}{\bar{u}}\right)^2\right] = C_L \rho \frac{\bar{u}^2}{2}\left(1 + S_u^2\right) \tag{3.3.13}$$

$$\frac{\bar{\lambda}}{\bar{\tau}_{cr}} = \frac{C_L \rho \frac{\bar{u}^2}{2}\left(1 + S_u^2\right)}{\bar{\tau}_{cr}} = \frac{C_L \rho\, u_*^2 \left(\frac{\bar{u}}{u_*}\right)^2 \left(1 + S_u^2\right)}{\bar{\tau}_{cr}} = \frac{C_L \rho \left(\frac{\bar{\tau}_b}{\rho}\right)\left(\frac{\bar{u}}{u_*}\right)^2 \left(1 + S_u^2\right)}{\bar{\tau}_{cr}} \tag{3.3.14}$$

and therefore,

$$\frac{\bar{\lambda}}{\bar{\tau}_{cr}} = \frac{C_L}{2}\left(\frac{\bar{u}}{u_*}\right)^2 \left(1 + S_u^2\right) \tag{3.3.15}$$

Substitution back into Equation 3.3.7, results in

$$\bar{\tau}_{cr}\, \frac{(1 + S_u n)^2}{1 + S_u^2} = \frac{\alpha_2}{\alpha_1} \frac{(\gamma_s - \gamma) d \left(\tan\Phi \cos\theta_b - \sin\theta_b\right)}{1 + \frac{C_L}{2}\left(\frac{\bar{u}}{u_*}\right)^2 \left(1 + S_u^2\right)\tan\Phi} \tag{3.3.16}$$

which simplifies to

$$\overline{\tau}_{cr} = \frac{\alpha_2}{\alpha_1}\frac{(\gamma_s-\gamma)d(\tan\Phi\cos\theta_b - \sin\theta_b)(1+S_u^2)}{\left[1+\frac{C_L}{2}\left(\frac{\overline{u}}{u_*}\right)^2(1+S_u^2)\tan\Phi\right](1+S_u n)^2} \tag{3.3.17}$$

At this point, an expression for the turbulent velocity profile, $\overline{u}/u_*$. For a turbulent flow the vertical profile of velocity for the near-bed flow is a function of the roughness Reynolds Number, $R_* = u_* k_s/\nu$, where k_s is the length scale for the bed roughness. When the flow is in the hydraulically rough range, $R_* > 100$, the flow is found to increase logarithmically away from the bed for $z > 3k_s$:

$$u(z) = \frac{u_*}{\kappa}\ln\left(\frac{z}{z_o}\right) \tag{3.3.18}$$

where the von Karman's constant is $\kappa = 0.407$, and $z_o = k_s/30$. In fully rough flow, the viscous sublayer, δ_ν, is compressed compared to hydraulically smooth or transitional flow, and the individual grains are found to extend up through the sublayer and into the turbulent flow, resulting in flow separation around the individual grains and a consequent independence of critical shear (Shields parameter) from Reynolds number. When the flow is in the hydraulically smooth range, $R_* > 3$, the grains at the surface of the bed are considered to be totally submerged in the viscous sublayer, which has an average height of $\delta_\nu = 11.6\nu/u_*$. Within the viscous sublayer, the velocity profile is linear, and for $R_* > 3$, $u(z) = u_*^2 z/\nu$ in this region. Above the viscous sublayer, the velocity profile is logarithmic and obeys Equation 3.3.18 with $z_o = \nu/(9u_*)$ for hydraulically smooth flow.

Wiberg and Smith (1987) use the equation of Reichardt (1951) for the velocity profile for transitional flow which, they argue, provides a nice transition between the viscous sub-layer and the logarithmic flow above and is also in excellent agreement with measurements, and use Equation 3.3.18 for hydraulically rough flow. One of the ideas advanced in their work is that in a heterogeneous mixture of cohesionless grains, the grains that are most likely to move are those that sit relatively high on the bed (e.g., those with their bottoms near the zero velocity level). They argue that these particles are minimally affected by the wakes of upstream particles when the flow is in the fully rough region of flow, and that it was therefore acceptable to extend the logarithmic velocity profile down to $z = z_o$. In the hydraulically smooth region of flow, they agree that the aforementioned expression for flow inside the viscous sublayer was only valid for $z > k_s$, but argue that since $k_s << \delta_v$, it was acceptable to approximate the near-bed flow by extending the linear velocity profile to the bed. They also argue that the transition between the viscous sublayer and the logarithmic flow above is not abrupt because the turbulent eddies depress and expand the viscous sublayer as they pass, and therefore the velocity at $z = d$ in reality lies between the linear and logarithmic values. Consequently, they sought an expression for velocity that yields a linear profile for $z << \delta_v$, a logarithmic profile for $z >> \delta_v$, and provides a smooth transition in the region in between. For this reason they use the expression of Reichardt (1951)

$$u(z)=u_*\left[\frac{1}{\kappa}\ln\left(1+\kappa z^+\right)-c\left(1-e^{-z^+-11.6}-\frac{z^+}{11.6}e^{-0.33z^+}\right)\right] \qquad (3.3.19)$$

where $z^+ = u_* z/\nu = R_* z/k_s$ and $z_o^+ = u_* z_o/\nu = R_* z_o/k_s$, to determine the velocity in the transitional region of flow ($3 < R_* < 100$). In the transitional region, the bed roughness parameter, z_o, is a function of roughness Reynolds number as given by Nikuradse (1933). Figure 3.2 shows the vertical velocity profile calculated from Equation 3.3.19 for $R_* = 1$.

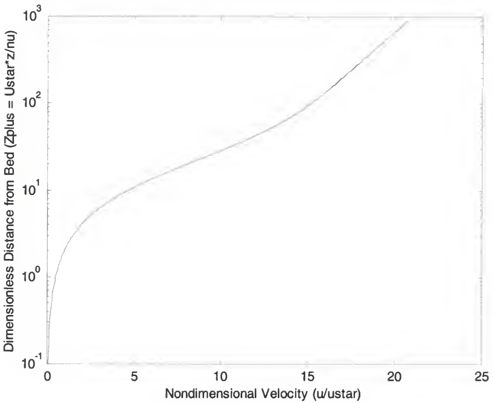

Figure 3.2 Velocity as a function of non-dimensional height above the bed. Equation of Reichardt (1951).

It should be noted that with Equation 3.3.19, all of the terms in Equation 3.3.17 can be either measured or calculated with the exception of the particle packing angle, Φ. It should also be mentioned that to use these two Equations (3.3.18 and 3.3.19) for non-dimensional velocity with the expression for critical shear stress, Equation 3.3.17, it is necessary to use Equation 3.3.19 in the transitional region of flow and to use Equation 3.3.18 in the hydraulically rough region of flow. It is also necessary to select the appropriate elevation above the bed at which to determine the non-dimensional velocity (this elevation is discussed subsequently).

Christensen (1972) notes that the classical expression based on Prandtl's well-known mixing length hypothesis gives very good results at moderate to great distances from the bed, but that it fails near the bed where z approaching zero results in a time-mean velocity approaching the highly unrealistic value of minus infinity. Consequently, he used

$$\frac{u}{u_*} = \frac{1}{\kappa} \ln\left(\frac{29.6z}{k_s} + 1 \right) \tag{3.3.20}$$

This velocity profile is identical to the classical expression except for the +1 term which makes the time-mean velocity equal to 0 at the bed, and is based on the work of Rossby (1932). This profile is plotted in Figure 3.3. Since it is only valid for the hydraulically rough range, it can be modified it so that it may be used in both the transitional region of flow and the fully rough region:

$$\frac{u}{u_*} = \frac{1}{\kappa} \left(q \frac{d}{k_s} e^{\kappa B} + 1 \right) \tag{3.3.21}$$

where q is the elevation above the bed expressed as a fraction of the grain size, d, and B is the Nikuradse velocity coefficient. It should be noted that as with the Reichardt (1951) formula, in this expression all of the terms in Equation 3.3.17 can be either measured or calculated with the exception of the particle packing angle, Φ. As before, it is necessary to select the appropriate elevation above the bed at which to determine the non-dimensional velocity.

Guoren (1981) developed an expression that accurately describes the velocity, at a given point above the bed, throughout all three regions of flow. He considered the occurrence of the three regions to be due to the degree of separation of the flow passing over the roughness elements. He argued that in the case of homogeneous roughness, the roughness element can be considered approximately as a sphere and that, consequently, the degree of separation, α_s, may be expressed as follows:

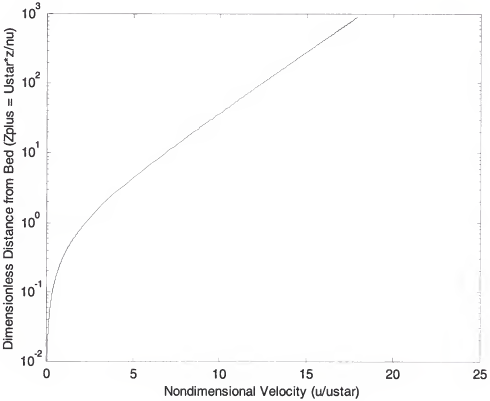

Figure 3.3 Turbulent time mean velocity distribution in proximity of rough bed, rough range. Profile of Christensen (1972).

$$\alpha_s = \left(1 - \cos\theta_{sep}\right)/2 \tag{3.3.22}$$

where θ_{sep} is the separation angle. Based on this concept he developed the following generalized velocity profile:

$$\frac{u}{u_*} = 2.5\ln\left(1 + \frac{u_* z}{5\nu}\right) + 7.05\left(\frac{\frac{u_* z}{5\nu}}{1 + \frac{u_* z}{5\nu}}\right)^2 + 2.5\left(\frac{\frac{u_* z}{5\nu}}{1 + \frac{u_* z}{5\nu}}\right) + B_* \tag{3.3.23}$$

where

$$B_* = \frac{u_a}{u_*} - 2.5\left(1 + \frac{\alpha_s u_* d}{5\nu}\right) - 7.05\left(\frac{\frac{\alpha_s u_* d}{5\nu}}{1 + \frac{\alpha_s u_* d}{5\nu}}\right)^2 + 2.5\left(\frac{\frac{\alpha_s u_* d}{5\nu}}{1 + \frac{\alpha_s u_* d}{5\nu}}\right) \tag{3.3.24}$$

$$\frac{u_a}{u_*} = -2.5\left(1 + \frac{\beta_s \alpha_s u_* d}{5\nu}\right) - 7.05\left(\frac{\frac{\beta_s \alpha_s u_* d}{5\nu}}{1 + \frac{\beta_s \alpha_s u_* d}{5\nu}}\right)^2 + 2.5\left(\frac{\frac{\beta_s \alpha_s u_* d}{5\nu}}{1 + \frac{\beta_s \alpha_s u_* d}{5\nu}}\right) \tag{3.3.25}$$

$$\beta_s = 1 - (1 - \beta_o)(\alpha_s + \theta_s/\pi)/2 \tag{3.3.26}$$

and

$$\theta_s/\pi = (\ln \mathrm{Re} - \ln \mathrm{Re}_1)/(\ln \mathrm{Re}_2 - \ln \mathrm{Re}_1) \tag{3.3.27}$$

in which $\mathrm{Re}_1 = 1.25$, $\mathrm{Re}_2 = 100$, and $\beta_o = 0.107$. A comparison of this profile with the other three and the data of Nikuradse (1933) is shown in Figure 3.4 from which it may be seen that a good agreement is obtained.

Coleman (1981) developed an expression that accurately describes the velocity above the bed of a sediment laden fluid. He accounted for the effect of suspended sediment through a modified expression for kinematic viscosity and a wake region augmentation function. His expression for viscosity is

$$\nu = \frac{\mu\left(1 + 2.5\varphi + 6.25\varphi_w^2 + 15.62\varphi_w^3\right)}{\rho + (\rho_s - \rho)^{\varphi_w}} \tag{3.3.28}$$

where μ is the dynamic viscosity of the fluid, φ_w is the sediment concentration at the point in question expressed as volume of sediment per unit volume of sediment-fluid mixture, ρ_s is the sediment density, and ρ is the fluid density. His velocity profile for bounded shear flows is

$$\frac{u}{u_*} = \left[\frac{1}{\kappa}\ln\left(\frac{u_* z}{\nu}\right) + A\right] - \frac{\Delta u}{u_*} + \frac{\Pi}{\kappa}\varpi\left(\frac{z}{\delta}\right) \tag{3.3.29}$$

where A is an integration constant, $\Delta u/u_*$ is the channel roughness velocity reduction function (Hinze, 1951), and $(\Pi/\kappa)\varpi(z/\delta)$ is the wake region velocity augmentation function containing the wake strength coefficient Π, and the boundary layer thickness δ. The symbol ω is merely a functional symbol. The augmentation function is defined as

$$\varpi\left(\frac{z}{\delta}\right) = 2\sin^2\left(\frac{\pi}{2}\frac{z}{\delta}\right) \tag{3.3.30}$$

and

$$\Pi = \frac{\kappa}{2}\left[\frac{u_m - u}{u_*}\right]_{\frac{z}{\delta}=1} \tag{3.3.31}$$

where u_m is the maximum velocity. A comparison of this profile with the other three, as they vary over the transitional and hydraulically rough ranges of flow, and with the data of Nikuradse (1933) is shown in Figure 3.4. All four profiles seem to compare well with each other and with the data.

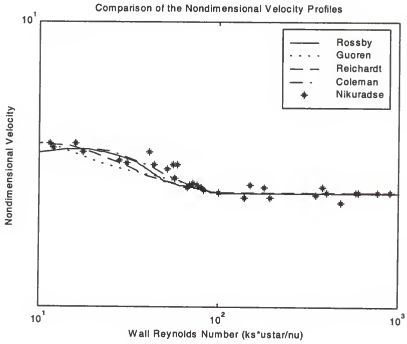

Figure 3.4 Comparison of four velocity profiles with the data of Nikuradse (1933).

The above four profiles were then substituted into the expression for critical bottom shear, Equation 3.3.17, and were found to compare well with the data of Shields (1936) as can be seen in Figure 3.5.

Values for several of the parameters in Equation 3.3.17 need to be defined before it may be used:

α_1: This parameter is the shape factor representing the bed area associated with one grain divided by the grain size squared. If the grains are spherical and arranged in a pattern that may be described between a square and a hexagon, it can be shown that a1 = 0.933.

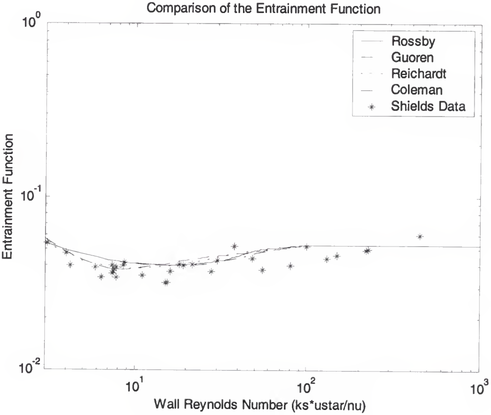

Figure 3.5 Comparison of profiles for critical bottom shear with the data of Shields (1936).

α_2: This parameter represents the grain volume divided by the grain-size cubed. By definition, this parameter is equal to p/6 or 0.524.

S_u and n: Using Einstein and El Samni's (1949) observations of the fluctuating lift, Christensen (1965) showed that the velocity fluctuations are normally distributed near the bed and S_u is constant and equal to 0.164, a value that is in good agreement with observations. Consequently, n may be found from the table of the Gaussian probability when the probability of exceeding τ_{cr} is selected. As noted earlier, Christensen and Bush (1971) showed that good agreement with observations was obtained if this probability is 0.001 corresponding to $n = 3.09$.

C_L: Einstein and El Samni (1949) and Christensen (1965) found a value of $C_L = 0.178$ produced the closest agreement with measurements, when the velocity used was measured at a distance of 0.35 d_{50} above the theoretical bed.

Φ: Wiberg and Smith (1987) argue that the particle packing angle changes for a bed composed of mixed sizes because it is easier for a large grain to roll over a bed of smaller particles than for a small grain to roll over a bed of larger particles. This is indicated by an increase in the value of Φ as the ratio of grain diameter to bed roughness length, d/k_s, decreases and is illustrated in Figure 3.6. Φ was defined using an expression derived from the work of Miller and Byrne (1966):

$$\Phi = \cos^{-1}\left[\frac{d/k_s + z_*}{d/k_s + 1}\right] \tag{3.3.32}$$

where z* is the average level of the bottom of the almost moving grain. The best agreement with Miller and Byrne (1966) was obtained with $z_* = -0.02$ for natural sand having a sphericity of 0.7 and roundness of 0.5.

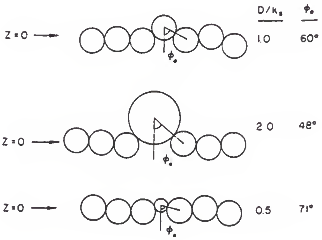

Figure 3.6 Relationship between the particle packing angle and the ratio of particle size to bed roughness scale, D/ks, where D is the grain diameter. In this representation the bottoms of the almost-moving grains are at the zero level of the bed, indicated by arrows at z = 0 (Wiberg and Smith, 1987).

Dade and Nowell (1991) suggested a threshold value of the solids fraction of a clay suspension above which a networked structure is formed at which point the sediment mixture behaves primarily as if it were a mud. They suggested threshold values of solids fraction ψ between 0.01 and 0.05 (1 and 5 percent) where ψ is defined as

$$\psi = \frac{\omega_{\mathrm{clay}} \rho_{clay}}{\omega_{\mathrm{clay}} \rho_{clay} + \omega_{sand} \rho_{sand}} \tag{3.3.33}$$

The results of Torfs (1995) concerning the mode of erosion agreed with this concept and indicated a transition from sandy to muddy-type erosion between 3% and 15%. The results of Nalluri and Alvarez (1992) indicated a transition between 2% and 17%. Mitchener and Torfs (1996) mention a transition zone in the mode of erosion from sand-type behavior to mud-type behavior between 7% and 13% from their results with montmorillonite mixtures. The results of Huygens and Verhoeven (1996) for kaolinite mixtures show a transition between 2% and 9%. Panagiotopoulos et al. (1997) noted two different regimes of critical conditions for erosion; one at mud content less than 30%, and one at mud content greater than 30%. The results of Sharif (2002) show a transition zone between 5% and 15% for kaolinite and sand mixtures. Examples of this trend are given in Figures 3.7 and 3.8.

The non-linear dependence of the critical shear stress on the fine-grained weight fraction is indicative of the interactive role of the sand grain matrix and the interstitial clay particles in controlling critical shear stress, and further suggests a potential route for improving this relationship. Incipient motion of an individual sand grain with interstitial clay particles can be examined by considering the forces acting on the grain resting at the bed surface subjected to turbulent flow.

As clay is added to sand the clay particles start to fill in the pore spaces of the sand matrix altering the pivoting characteristics and consequently the value of the internal friction angle. At low clay content, clay apparently acts to lubricate the sand grain at its contact points reducing the internal friction angle and resulting in the decrease in $\bar{\tau}_{cr}$ as shown in Figures 3.7 and 3.8. Hence, this lubricating effect of clay can be shown through the adoption, in Equation 3.3.17, of an effective particle packing angle, Φ_{eff}:

$$\bar{\tau}_{cr}=\frac{\alpha_2}{\alpha_1}\frac{(\gamma_s-\gamma)d\left(\tan\Phi_{\mathrm{eff}}\cos\theta_b-\sin\theta_b\right)\left(1+S_u^2\right)}{\left[1+\frac{C_L}{2}\left(\frac{\bar{u}}{u_*}\right)^2\left(1+S_u^2\right)\tan\Phi_{\mathrm{eff}}\right]\left(1+S_u n\right)^2} \tag{3.3.34}$$

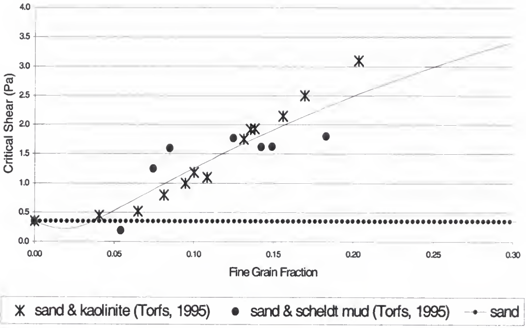

Figure 3.7 Critical shear stress for erosion of kaolinit/sand and scheldt mud/sand mixtures versus fine grain weight fraction: data (Torfs, 1995).

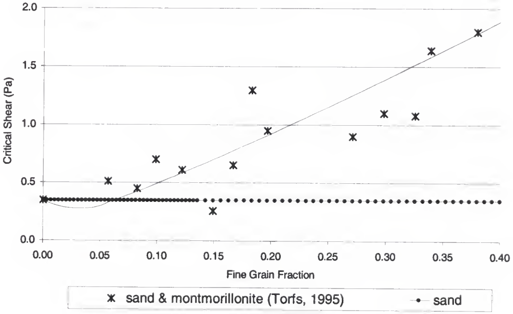

Figure 3.8 Critical shear stress for erosion of Montmorillonite/sand mixture versus fine grain weight fraction: data (Torfs, 1995)

CHAPTER 4
EXPERIMENTAL SETUP AND PROCEDURES

4.1 Introduction

To test the validity of the analysis carried out in Chapter 3, which derives the critical shear stress of sand in the presence of clay, laboratory experiments were conducted. The experimental setup, procedures and tests are presented in this chapter.

4.2 Flume

Tests were carried out in a small flume at the Coastal Engineering Laboratory of the University of Florida. McAnally (2000) has provided a brief summary of the underlying design-and-operation concept of such open channel flumes. Typically, a pump is used to deliver water from a tail basin to a head basin. The water then flows through the flume back into the tail basin completing the circuit. The velocity, and consequently the bottom shear stress, are controlled by regulating the pumps' discharge.

Figure 4.1, which shows the schematic of the flume, was constructed of 3-cm-thick Plexiglas to dimensions of 4.3 m length, 15 cm width, and 19 cm depth. It was elevated to a height of 92 cm above the floor and supported by a wooden table the base of which was adjustable and used to level the flume.

The head basin was constructed of 3-cm-thick Plexiglas to dimensions of 89 cm length, 183 cm width, and 29 cm depth. It was fed by a Worthington model D814 centrifugal pump with a Baldor, single-phase, 1 hp, L5510F motor. The basin was fed via a 7.6 cm OD PVC pipe into which several holes were drilled so as to evenly distribute the incoming water and minimize any currents in the head basin. The current velocity in the input pipe was measured using a Signet model MK525 metalex "paddle-wheel" type current meter.

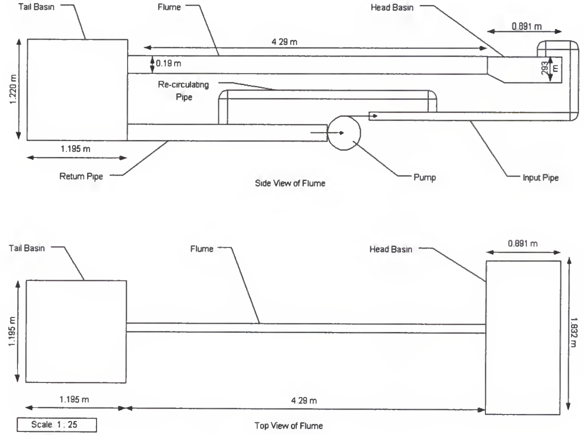

Figure 4.1 Schematic drawing of flume.

A vertical sluice gate was installed at the end of the flume to regulate the water surface height. It was constructed of 6.6 mm Plexiglas slightly wider than the width of the flume, and was placed at the end of the flume immediately before the tail basin. The sluice gate could be raised or lowered, which would in turn increase or decrease, respectively, the flow area underneath the gate. Consequently, for a given discharge the sluice gate could be used to control the surface height of the water in the flume.

The tail basin was constructed of 3-cm-thick Plexiglas to dimensions of 120 cm long, 120 cm wide, and 122 cm deep. This basin was supported by a frame constructed of 5.1 cm aluminum, the base of which was adjustable and was used to level the basin. Water flowed into the top of the basin and out of the bottom side of the basin through a 15.2 cm OD PVC outflow pipe. This pipe connected to both a 7.6 cm OD PVC re-circulating pipe and the pump. A bypass pipe was added to control the pump's discharge.

Current profiles were measured using a Kent miniflo model 265 propeller-type current meter. This current meter was attached to a vernier scale, so that the depth of the sensor could be accurately measured. The vernier scale was attached to a sliding aluminum mount, so that the current meter could be moved along the length of the flume, and be maintained in a position perpendicular to the flow so only the horizontal component of velocity was measured. The current meter and the vernier scale may be seen in Figure 4.2.

Seven 0.3 cm holes were drilled into the side of the flume at positions 115 cm, 165 cm, and 425 cm from the upstream end of the flume, so that water samples at different depths could be extracted during experimental runs to obtain sediment concentrations profiles, and a manometer was used to determine the slope of the water surface across three different points along the length of the flume. The manometer and two of the three sets of side-holes may be seen in Figure 4.3.

A false bottom was constructed of 3-cm-thick Plexiglas and secured to the bottom of the flume so that a sediment bed could be placed into the flume. The false bottom, seen in Figures 4.3 and 4.4, was made into three segments. The front segment was 198.5 cm long, 2.5 cm high, the width of the inside of the flume, and secured at the upstream end of the flume with silicon gel so that it would neither move nor leak but could be removed later if needed. The end segment was 20 cm long, 2.5 cm high, the width of the inside of the flume, and similarly secured at a distance of 400 cm from the upstream end the flume. The middle segment was 226 cm long, 2.5 cm high, the width of the inside of the flume, and designed to be removed and replaced with a sediment bed. It could lay flush with and in between the front and back segments. In this way, when emplaced it resulted in a flat bottom 2.5 cm above the flume bottom. As seen in Figure 4.4, the middle segment began at a distance of 199 cm from the upstream end of the flume and ended at a distance of 425 cm.

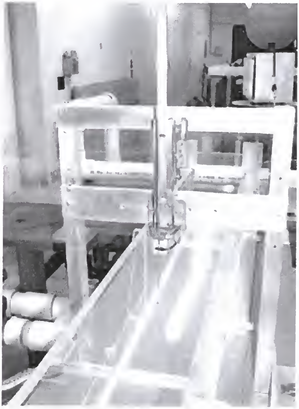

Figure 4.2 Kent propeller type current meter and its mount.

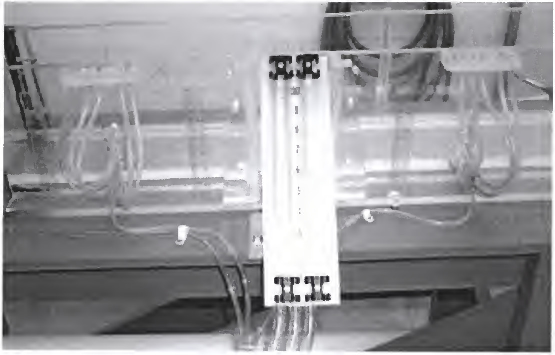

Figure 4.3 Manometer and sampling locations.

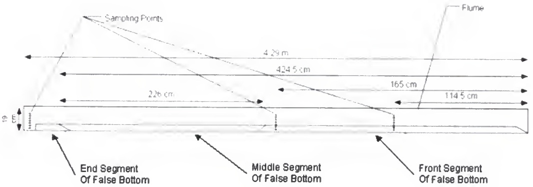
Sampling Points
Flume
4.29 m
424.5 cm
165 cm
114.5 cm
226 cm
19 cm
End Segment Of False Bottom
Middle Segment Of False Bottom
Front Segment Of False Bottom

Figure 4.4 Schematic drawing of flume detailing sampling points and false bottom.

4.3 Simulator of Erosion Rate Function

The Simulator of Erosion Rate Function (SERF) was similar in principle to those designed by earlier investigators (Moore and Masch, 1962; Arulanandan et al., 1975; Croad, 1981; Chapuis and Gatien, 1986). Lee and Mehta (1994) have provided a brief summary of the underlying design-and-operation concept. Typically, these devices consist of a rotating outer cylinder, which is filled with the chosen eroding fluid. A remolded or intact sample in the shape of a smaller cylinder is placed into the outer cylinder. While rotating, the outer cylinder imparts rotation to the fluid, which translates into a shear stress being uniformly imparted to the sample. The torque applied to the stationary sample is measured and converted to the corresponding shear stress. Erosion of the sample follows, and a relation is obtained between erosion rate and shear stress. In SERF a load cell allowed the eroded mass to be measured without removing the sample assembly from the outer cylinder.

Figure 4.5 shows the schematic of the SERF, and Figure 4.6 is a photographic view. The clay sample is molded into a cylinder with a diameter of 7.6 cm and a height of 9.6 cm. The cylinder is impaled on a shaft which secures an upper and a lower disk of equal diameters to the two ends of the sample. The upper end of the shaft affixes to an Omega (Stamford, CT) model TQ201-100Z torque cell, which is in turn connected to an Omega model LC601-5 load cell. When the acrylic outer cylinder is rotated, the chosen eroding fluid imparts a torque to the sample, and in turn the shaft and torque cell. The cell is connected to an Omega model DP25-S LED (light-emitting diode) display, and shows the applied torque in g-cm. The load cell is attached to the entire shaft/torque cell/sample assembly, and can be used to measure mass eroded after a given run. This unit can move vertically out of the outer cylinder for sample and water replacements.

The outer cylinder is capable of rotating at a maximum of 2,350 rpm, and a minimum of 150 rpm. The torque cell has a 1,800 g-cm capability, and the load cell can accommodate a maximum of 2.3 kg.

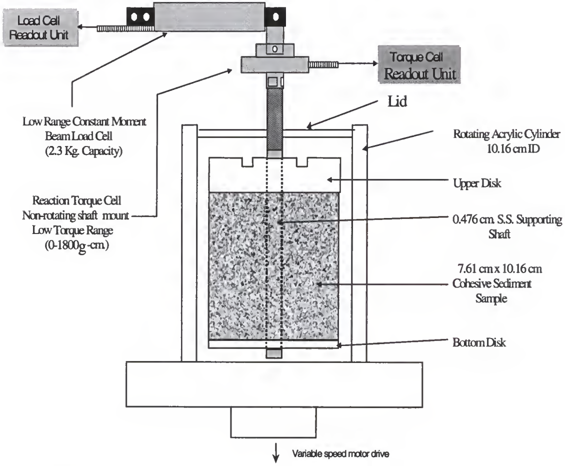
Load Cell Readout Unit
Torque Cell Readout Unit
Lid
Low Range Constant Moment Beam Load Cell (2.3 Kg. Capacity)
Rotating Acrylic Cylinder 10.16 cm ID
Upper Disk
Reaction Torque Cell Non-rotating shaft mount Low Torque Range (0-1800g-cm)
0.476 cm. S.S. Supporting Shaft
7.61 cm x 10.16 cm Cohesive Sediment Sample
Bottom Disk
Variable speed motor drive

Figure 4.5 Schematic of SERF.

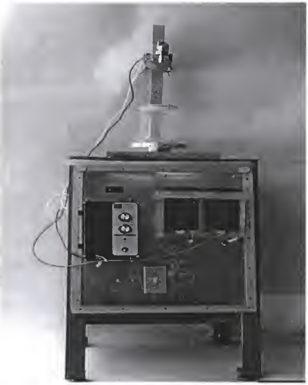

Figure 4.6 Front-view of SERF showing the rotating cylinder assembly, speed control panel (lower left) and digital readouts (lower right) for the torque cell and the load cell.

4.4 Schulze Ring Shear Tester

The Schulze Ring Shear Tester shown in Figure 4.7 is similar in principle to the common Jenike shear tester. It consists primarily of a lower rotating annular tray that holds the sample, and an annular disk that is placed on top the sample and just barely inside the bottom tray as can be seen in Figure 4.8.

The lower rotating tray is used to apply a shear stress to the sample, while the upper annular disk is used to apply a normal force. The lower tray is connected to an electric motor, while the upper tray is connected to two horizontal load cells in order to measure the torque being applied to the sample, and is also connected to a single vertical load cell used to measure the normal force. These components may be seen in Figure 4.9.

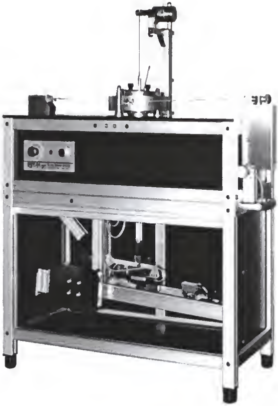

Figure 4.7 Schulze Ring Shear Tester.

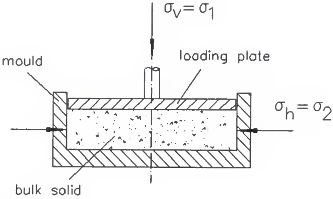

Figure 4.8 Cross-sectional view of sample inside upper annular disk and lower annular tray.

Figure 4.10 shows a schematic of the upper disk, and Figure 4.11 contains a schematic of the fins that were attached to the bottom of the upper disk to prevent sample material from sliding.

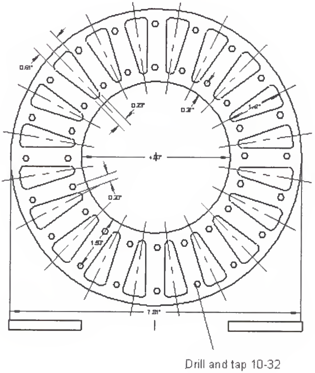

Figure 4.10 Schematic of upper annular disk.

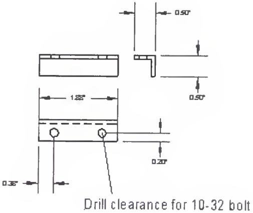

Figure 4.11 Fin schematic.

The lower tray was machined out of solid aluminum while the upper disk was constructed out of 0.16 cm thick perforated aluminum supported by 1.3 cm thick Plexiglas designed according to Figure 4.10. The perforated aluminum on the upper disk allowed water to seep through when a normal force was applied to the sample. This controlled the pore water pressure and kept the load on the sediment matrix. Additionally, the fins were screwed onto the perforated aluminum of the upper disk.

The Schulze tester allowed for automated load application. The vertical load, N, as shown in Figure 4.9, acting on the bulk solid sample could be adjusted by the operator. The tester also had a digitally controlled motor drive for shear cell rotation. Thus, cell rotation w (Figure 4.9) was computer-controlled. The shear force, $F_1 = F_2$ (Figure 4.9), was automatically measured and the output was viewed using a Linseis plotter. Testing at very low pressures was accomplished with a counterweight system to reduce the weight of the lid and other parts connected to the lid. Thus, tests at stresses < 500 Pa were possible.

4.5 Materials

The soil materials used for these experiments were clay minerals, commercially prepared clays, and sand particles. All three were obtained commercially, and were well graded. All three materials were analyzed for particle size distribution, and the clay were additionally analyzed for pertinent physicochemical properties such as the Cation Exchange Capacity (CEC).

Three types of commercially available clays were selected which together cover a wide range of cohesive soil properties; a kaolinite, a bentonite, and an attapulgite. Kaolinite (pulverized kaolin), a light beige-colored powder, was obtained from the EPK Division of Feldspar Corporation in Edgar, Florida. Its Cation Exchange Capacity (CEC) as given by the supplier, was 5.2 - 6.5 milliequivalents per 100 grams. Its granular density was 2,603 kg/m^3. Bentonite was obtained from the American Colloid Company in Arlington Heights, Illinois. It was a sodium montmorillonite (commercial name Volclay) of a light gray color. Its CEC was 105 milliequivalents per 100 grams, and its granular density was 2,760 kg/m^3. Attapulgite, of a greenish-white color, was obtained from Floridin Company in Quincy, Florida. Also known as palygorskite, its CEC was 28 milliequivalents per 100 grams, and its granular density was 2,300 kg/m^3.

The median particle sizes of attapulgite, bentonite, and kaolinite were 0.86 μm, 1.01 μm, and 1.10 μm, respectively. These three clays were used to create two different mixtures. Mixture #1 was composed of 50% kaolinite, 45% attapulgite, and 5% bentonite. Mixture #2 was composed of 50% kaolinite, 35% attapulgite, and 15% bentonite.

Three commercially prepared ceramic clays were obtained from Bennett Pottery Supply (Orlando, Florida) #10, #20, and #75. Clay #10 had a d_{50} value of 0.45 μm, #20 had a d_{50} of 0.36 μm and #75 had a d_{50} of 0.46 μm. The cumulative size distribution plots may be seen in Figures 4.12 through 4.14. These three clays were also analyzed using a computer-controlled x-ray diffractometer. Each of the clays was scanned from 2° to 60° of 2θ using copper kα radiation. The results of this analysis can be seen in Table 4.1.

Five angular quartz sands from the Feldspar Corporation in Edgar, Florida were used to provide a range of d_{50} values. The sand, which had the largest d_{50} value of 1.40 mm, was Feldspar F 8-20. The cumulative size distribution plot for this sand may be seen in Figure 4.15 and a picture of the grains in Figure 4.20. The second, with a d_{50}

value of 0.94 mm, was Feldspar sand sieved in through a #20 screen (Figures 4.16). The third, with a d_{50} value of 0.83 mm, was the Feldspar 20-30 (Figures 4.17 and 4.21). The fourth, with a d_{50} value of 0.47 mm, was Feldspar sand sieved through a #30 screen (Figure 4.18). The smallest, with a d_{50} value of 0.41 mm, was Feldspar sand sieved through a #40 screen (Figures 4.19 and 4.22).

Table 4.1 Composition of commercially prepared clays in order of predominance

Material	Bennett Pottery #10	Bennett Pottery #20	Bennett Pottery #75
Kaolinite	Yes	Yes	Yes
Quartz	Yes	Yes	Yes
Mica	Yes	Yes	No
Vermiculite	Yes	Yes	No

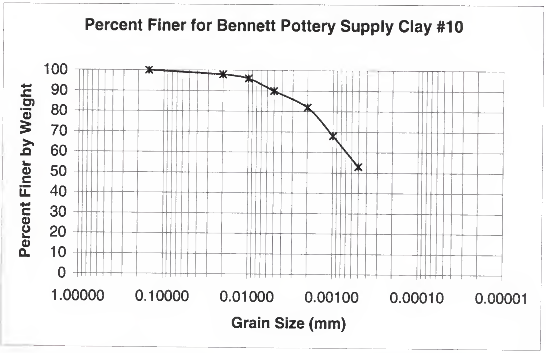

Figure 4.12 Cumulative size distribution plot of Bennett Pottery Supply Clay #10.

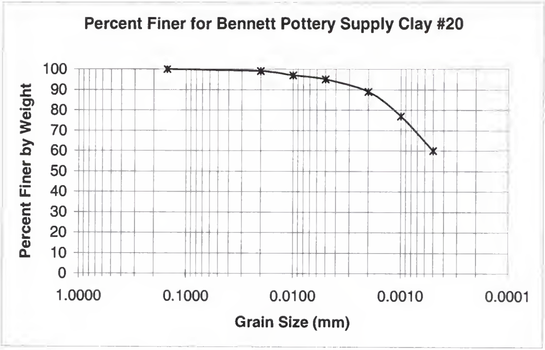

Figure 4. 13 Cumulative size distribution plot of Bennett Pottery Supply Clay #20.

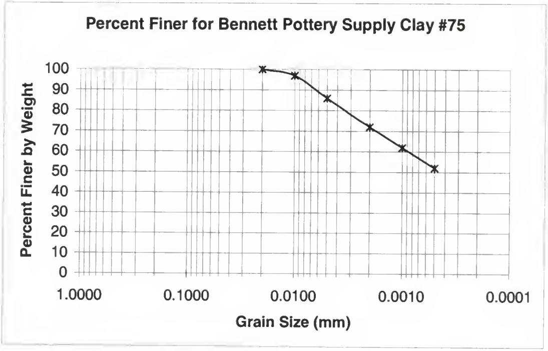

Figure 4.14 Cumulative size distribution plot of Bennett Pottery Supply Clay #75.

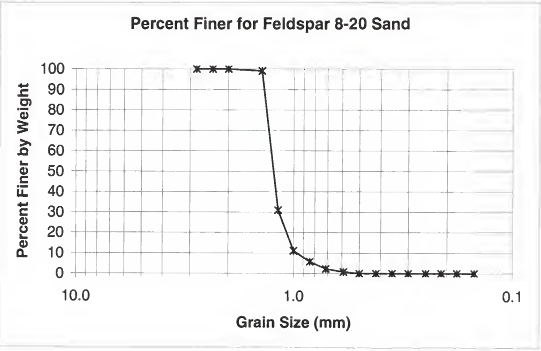

Figure 4.15 Cumulative size distribution plot of Feldspar F 8-20 sand.

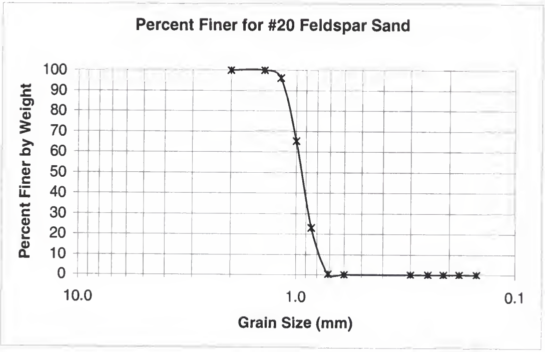

Figure 4.16 Cumulative size distribution plot of Feldspar sand sieved through a #20 screen.

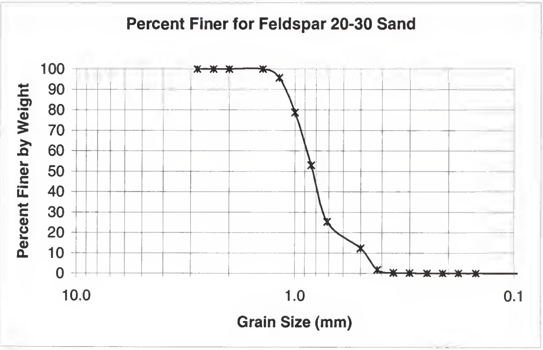

Figure 4.17 Cumulative size distribution plot of Feldspar 20-30 sand.

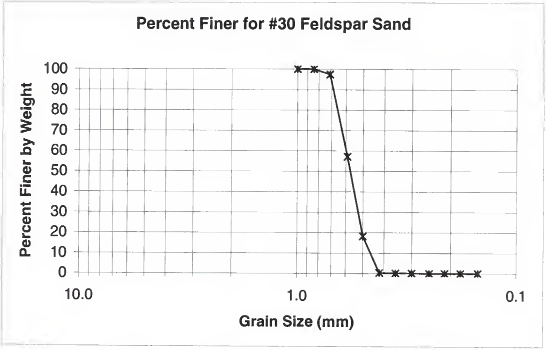

Figure 4.18 Cumulative size distribution plot of Feldspar sand sieved through a #30 screen.

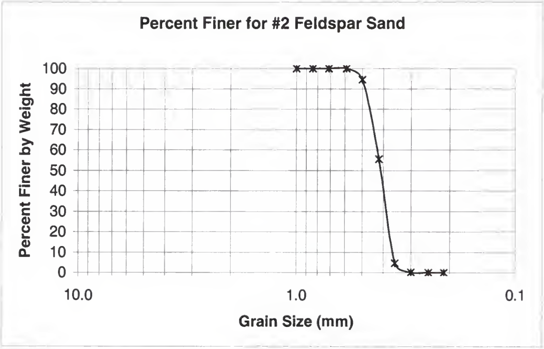

Figure 4.19 Cumulative size distribution plot of Feldspar sand sieved through a #40 screen.

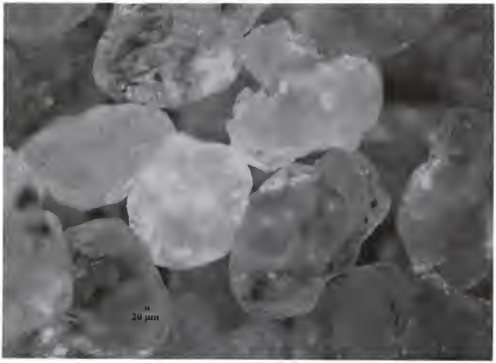

Figure 4.20 Picture of sand grains of Feldspar sand sieved through a #40 screen.

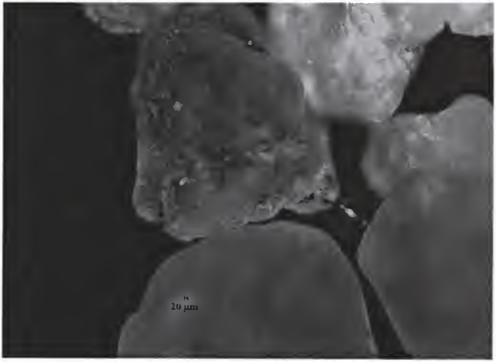

Figure 4.21 Picture of sand grains of Feldspar 20-30 sand.

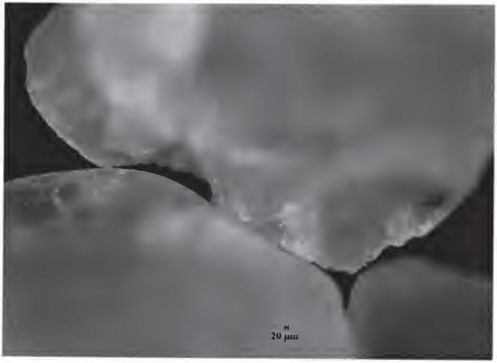

Figure 4.22 Picture of sand grains of Feldspar F 8-20 sand.

4.6 Flume Calibration and Experimental Procedure

The flume was calibrated to obtain the relationship between the sluice gate height and discharge, so that the discharge could be calculated knowing the water surface height immediately before the gate and the gate height, and to obtain the Manning's coefficient of the Plexiglas, so that the wall friction could later be subtracted out to obtain the bottom shear values for a given flow condition.

The discharge Q was related to the gate height and the water surface elevation immediately upstream of the gate through

$$Q = y_g b C_d \sqrt{2g\Delta H} \tag{4.6.1}$$

where y_g is the gate height in meters, b is the flume width in meters (= 0.15 m), C_d is the discharge coefficient (= 0.45), g is acceleration due to gravity, and $\Delta H = y_1 - y_g$ where y_1 is surface elevation immediately upstream of the gate. Figures 4.23 and 4.24 show the results for two gate heights.

Manning's n value was calculated by using the standard step method to calculate the back-water profile in the flume for a series of runs each with a different discharge. For each run, the surface elevation in the flume was measured 91 cm upstream of the bed, in 15.2 cm increments along the length of the bed starting at the front of the bed and ending at the back, and 61 cm from the back of the bed. In the used for each run, Manning's n was varied until the calculated and measured surface elevations matched. Figures 4.25 and 4.26 provide an example of two different runs.

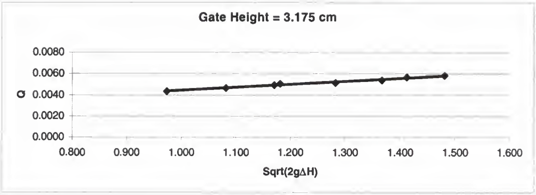

Figure 4.23 Relationship for discharge calculation for gate height of 3.18 cm.

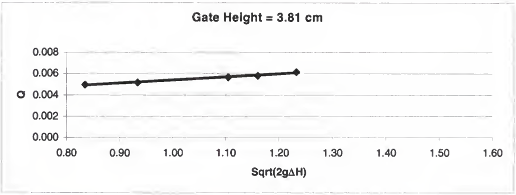

Figure 4.24 Relationship for discharge calculation for gate height of 3.81 cm.

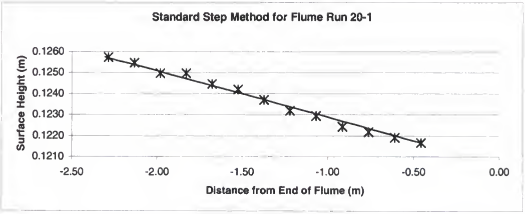

Figure 4.25 Comparison of calculated and measured surface elevations for Run 20-1.

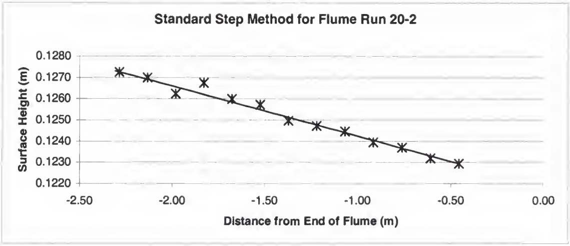

Figure 4.26 Comparison of calculated and measured surface elevations for Run 20-2.

Manning's n value for each run was then averaged to obtain a value of 0.014 for the bed which compares well with the reported value for Plexiglas of 0.010.

4.7 SERF Calibration and Experimental Procedure

The torque cell was calibrated using an aluminum ring affixed to the shaft of the cell. A two-point calibration was done using no load, and then with a 1 kg weight hanging from the ring, which had a radius of 1 cm. This resulted in a calibration between 0 and 1 kg-cm. The load cell was calibrated in the same two-point fashion, using a 1 kg weight hung from the cell.

The calibration to convert torque into shear stress required running the device with dummy samples. SERF was run with three aluminum cylinders of varying diameters but identical height. The varying of diameters provided a relationship between the applied torque and the sample radius, considered to be necessary in instances when the radius of a sample decreases measurably due to erosion. For a given cylinder, SERF was rotated from a standstill to a “reasonable” speed (up to 1,600 rpm) in time-steps, and torque readings were taken at each rpm value after steady-state was reached (typically within 5 seconds). Once at peak rpm, the device was slowed in time-steps and torque readings were taken again. This procedure was done three times for each cylinder, the shaft and cylinder being removed and re-installed each time in order to gauge the precision of the device after re-installment of samples. The bottom disk of the sample holder was also tested in this manner. By subtracting the bottom disk torque from the total torque, the torque applied to the sample area can be obtained. The water meniscus was located just below the upper disk (Fig. 4.5) for the fluid to act on the cylinder and the bottom disk. It was at times necessary to add or remove water to obtain the appropriate meniscus.

A trend-line was plotted for the variation of torque with rpm for the disk, and the corresponding relation (Eq. 4.7.1) was used to determine the torque provided by the sample area by subtracting the bottom disk torque (Fig. 4.5) from the overall torque. This adjusted torque value was converted into shear stress using Eqs. 4.7.1 and 4.7.3:

$$\mathrm{T} = 0.0086\mathrm{RPM} - 1 \tag{4.7.1}$$

$$F_T = \frac{\mathrm{T}}{r_c} \tag{4.7.2}$$

$$\tau = \frac{gF_{\tan}}{A_c} \tag{4.7.3}$$

where T is the torque reading in kg-m (g-cm for Eq. 4.7.1), r_c is the cylinder radius in m, F_{tan} is the applied tangential force in kg, τ is the shear stress in Pa, g is the acceleration due to gravity in m/s^2, and A_c is the cylinder surface area in m^2. The shear stress values were then plotted versus rpm to yield calibration curves for three cylinders (Figs. 4.27, 4.28, 4.29). The spread in data was attributed to slight but inevitable changes in the alignment of the cylinders with respect to the central axis, due to the removal and re-installment of the shaft/cylinder assembly between runs. This procedure of removal/re-installment was carried out in order to identify the degree of precision of the device. Overall, the small and large cylinders followed a power fit, and the medium cylinder followed a linear trend Figs. 4.27, 4.28, 4.29). Fitting a power function to the medium cylinder resulted in overestimation of shear stress at high rpm (>1,000).

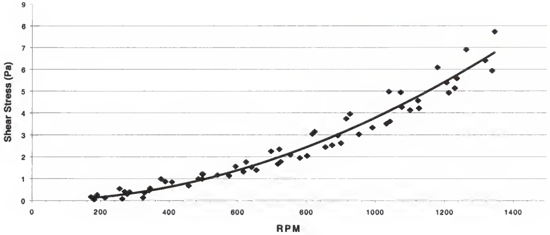

Figure 4.27 Calibration curve for large aluminum cylinder (dia.=7.6 cm).

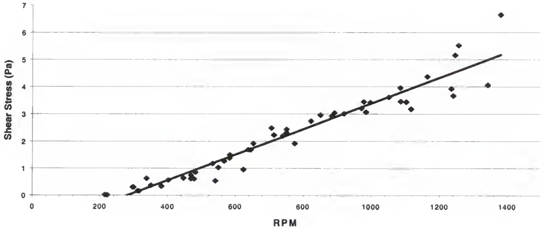

Figure 4.28 Calibration curve for medium aluminum cylinder (dia.=7.2 cm).

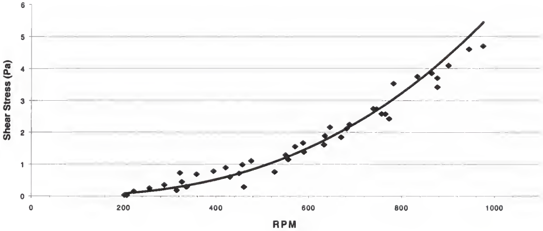

Figure 4.29 Calibration curve for small aluminum cylinder (dia.=6.8 cm).

For the large, medium, and small cylinder, respectively, the following relations were obtained:

$$\tau = 4.9\, x\, 10^{-6} \mathrm{RPM}^{1.96} \tag{4.7.4}$$

$$\tau = 4.7\, x\, 10^{-3} \mathrm{RPM} - 1.32 \tag{4.7.5}$$

$$\tau = 8.0\, x\, 10^{-8} \mathrm{RPM}^{2.63} \tag{4.7.6}$$

As an illustration of the differences among the above relations note that a 10% decrease in surface area from the small cylinder to the large cylinder led to a 67% increase in shear stress at an rpm of 1,000 for the small cylinder. This resulted from the decreased moment arm of the small cylinder leading to an increased tangential force and therefore increased shear stress.

The three ceramic clays from Bennett Pottery Supply (Orlando, FL), #10, #20, and #75 were used. Each clay was molded to two different bulk densities (both lower than initial) by adding tap water and working by hand. This procedure was repeated twice, resulting in four densities tested for each clay. A third set was prepared by molding two equal amounts of clay with water, one with tap water and another with 35 ppt salt (sodium chloride) water. Water was added in equal amounts to yield a similar density. Since the clays arrived with existing pore water, the actual salinity of the pore water was less than 35 ppt.

The first set of clays was shaped into cylinders of the same diameter as the medium cylinder, hence the medium cylinder calibration curve was used. The second set of samples was shaped into the diameter of the large cylinder, as was the third set. The volume and surface area of each sample were known, and sample mass was determined by weighing the sample with the bracket and lid (Figs. 4.5, 4.6), and then weighing only the bracket and lid. This provided the density of each respective sample.

Once a sample was emplaced within into the outer cylinder the load cell was zeroed. After 5 to 15 min of rotation at a given rpm, the device was stopped and allowed to rest for approximately one minute. The actual time-step (between 5 and 15 min) depended on sample erodibility. In most cases the maximum speed of the outer cylinder was 1,500 rpm. Above this speed, the possibility of mass erosion (i.e., large clasts being eroded) was present, which could have resulted in an imbalance and excessive torque, thereby damaging the torque cell. After reaching steady-state, the device was stopped and the load cell displayed the loss in material in grams.

Since the load cell measured buoyant mass, only the mass loss of solids was being displayed. This value, along with the time-step and the surface area resulted in the erosion rate:

$$\varepsilon = \frac{\Delta m_s}{A_{cs} \Delta t} \tag{4.7.7}$$

where Δm_s is the dry sediment mass loss, A_{cs} is the sample surface area in m^2, and Δt is the time interval in seconds.

A comment is in order concerning the operating speed range of SERF, the generation of Taylor vortices in the annular gap between the outer cylinder and the sample, and the development of turbulence in this gap. When a certain Reynolds number has been exceeded in the gap between two rotating concentric cylinders, vortices appear. The axes of these vortices are along the circumferences of the cylinders, and they rotate in alternately opposite directions (Schlichting, 1979). The Taylor number T_a is used to predict the formation of these irregularities

$$T_a = \frac{U_a w_g}{\nu}\sqrt{\frac{w_g}{R_i}} \tag{4.7.8}$$

where U_a is the annular peripheral velocity of the cylinder, w_g is the gap width, R_i is the inner cylinder's radius, and ν is the kinematic viscosity of the fluid. Taylor vortices are formed in the range $41.3 < T_a < 400$, within a laminar flow regime (Schlichting, 1968). Even at the lowest operating speed of SERF, which corresponds to a peripheral velocity of 0.8 m/s (at 150 rpm), using a gap width of 0.024 m, an inner cylinder radius of 0.038 m, and water as the fluid (($\nu=10^{-6}$ m^2/s), the Taylor number was 15,000, well over the range of Taylor vortex formation.

With the characteristic Reynolds number defined as

$$\mathrm{Re} = \frac{U_a w_g}{\nu} \tag{4.7.9}$$

using an annular peripheral velocity of 0.8 m/s and the same fluid and gap width, Re = 18,880 is obtained. The SERF was typically operated above this speed, and in these tests the lowest Re attained was 100,000 at a speed of 4.3 m/s (at 800 rpm). Operating above the Taylor vortex regime and above the laminar flow regime, one can expect a comparatively uniform distribution of shear stress over the sample surface area. A detailed operator's manual may be found in Ganju et al. (2000).

4.8 Schulze Ring Shear Tester Calibration and Experimental Procedure

The calibration of the Schulze Ring Shear Tester was accomplished at the start of each run to assure that the data being collected were accurate. The calibration was carried out using an 80g aluminum weight holder designed to connect to the load cells and to carry a series of weighted plates. A measure was first taken on the Linseis strip chart with no load. Next, the 80g weight holder was connected and another reading was taken using the strip chart. After this, a 1 kg weight was placed onto the weight holder and a reading was taken using the strip chart. Again, an additional 1 kg weight was loaded onto the weight holder and a reading taken completing the calibration procedure. These readings provided a linear scale between the load placed on the load cell and the displacement on the strip chart against which readings taken during tests could be scaled.

Next, the sample bulk solid was placed into the shear cell and preconsolidated manually. It was then sheared at a normal stress σ_{pre} which was adjusted by a specific normal force *N*. The shear force *S*, acting over area *A*, increased with time *t* as indicated in the left diagram of Figure 4.30. Besides the shear stress, the bulk density of the sample also increased as the sand matrix decreased in volume as sand grains moved to a tighter, stronger packing structure. After a certain time (on the order of 10 minutes) a constant bulk density and a constant shear stress (τ_{pre}) prevailed.

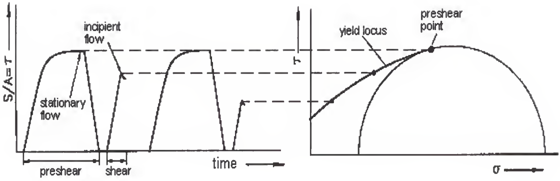

Figure 4.30 Plot of the shear stresses with time illustrating the data collection process, and the corresponding yield locus.

Both bulk density and shear stress are characteristic for the normal stress σ_{pre}, which means that each normal stress σ_{pre} results in a specific constant bulk density and shear stress. The deformation of the bulk solid at constant normal and shear stresses and constant bulk density represents a steady-state (or stationary) flow, and the process of attaining steady-state is called "preshear". With the preshear process the bulk solid is placed into a defined consolidation state (similar to the application of the consolidation stress in a uniaxial compression test). Preshear is arrested once steady state is reached by reversing the direction of rotation of the sample disk until $S = 0$ ($\tau = 0$). The values of normal stress σ_{pre} and the corresponding shear stress τ_{pre} form the point of steady state flow in the σ, τ-diagram (Figure 4.30, right diagram)

Afterwards, the sample is sheared again with a reduced normal stress $\sigma_{sh} < \sigma_{pre}$. Since the sample is now sheared under a smaller normal load than at preshear, it will start to flow (break) at a certain shear stress (similar to the breakage of the sample in a uniaxial test).

A bulk solid starts to flow when the Mohr stress circle representing the actual stress state touches the yield locus. The start of flow is connected to a decrease in the bulk density and a corresponding reduction of the shear stress (see Figure 4.30). The maximum in the plot of the shear stress versus time indicates the start of flow. The corresponding normal and the shear stresses describe a point on the yield locus in the σ, τ-diagram. If several samples of bulk solid are presheared under the identical normal stress σ_{pre} but sheared under different normal stresses $\sigma_{sh} < \sigma_{pre}$, the path of the yield locus in the σ, τ-diagram can be determined.

The parameters which describe the flow properties can be determined from the yield locus (Figure 4.31). The relevant consolidation stress σ_1 is equal to the major principal stress of the Mohr stress circle which is tangential to the yield locus and intersects at the point of steady state flow (σ_{pre} , τ_{pre}). This stress circle represents the stresses in the sample at the end of the consolidation process (stresses at steady state flow). The unconfined yield strength σ_c results from the stress circle which is tangential to the yield locus and which runs through the origin (minor principal stress $\sigma_2 = 0$). This stress circle represents the same stress state as the one which prevails in the second step of a uniaxial compression test. In contrast to a uniaxial compression test, the unconfined yield strength σ_c has to be determined on basis of the yield locus and does not follow directly from the measurement.

The tangent at the largest Mohr stress circle is called the effective yield locus. It encloses the σ-axis with the angle φ_e (effective angle of internal friction). Because the largest Mohr stress circle indicates a steady state flow, φ_e can be used as a measure of the internal friction at steady state flow.

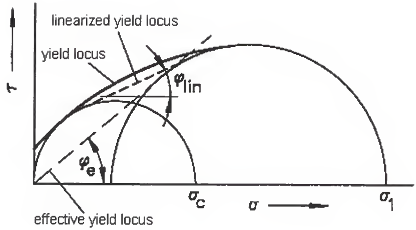

Figure 4.31 Yield locus.

The angle of internal friction φ_i is defined as the local slope angle of the yield locus. Because the yield locus is curved instead of being straight, φ_i varies along the yield locus. It is sufficient for most applications to state one value of φ_i. In this case, the internal friction angle is defined by the slope φ_{lin} of the linearized yield locus. The linearized yield locus results from the tangent common to both Mohr stress circles shown in Figure 4.31 (Schulze, 1994).

CHAPTER 5
EXPERIMENTAL RESULTS

5.1 SERF Experiments

Eighteen clay samples were tested in total, and for all but three samples (#2, #9 and #15) erosion was detected by the load cell. The experimental conditions under which these samples (less 2, #9 and #15) were tested are listed in Table 5.1.

Table 5.1 SERF experimental conditions

Sample #	Clay # (Bennet Pottery Supply)	Pore Water Composition	Density, ρ (kg/m^3)	Range of Applied Shear Stress (Pa)
1	10	fresh	1665	2.9 - 5.8
3	10	fresh	1710	2.8 - 5.9
4	10	fresh	1859	4.2 - 8.1
5	10	saline	1928	2.3 - 6.5
6	10	fresh	1928	2.2 - 7.5
7	20	fresh	1435	1.6 - 3.9
8	20	fresh	1537	4.1 - 5.4
10	20	fresh	1721	2.8 - 4.5
11	20	saline	1894	2.9 - 5.8
12	20	fresh	1905	4.1 - 6.5
13	75	fresh	1675	1.1 - 4.5
14	75	fresh	1698	2.0 - 4.5
16	75	fresh	1806	2.9 - 5.7
17	75	saline	1940	3.1 - 6.4
18	75	fresh	1963	3.2 - 6.8

A dimensionless erosion rate as a function of dimensionless shear stress plot was obtained as may be seen in Figure 5.1. For that purpose, linear trend-lines were fitted to each set of results with the following form:

$$\varepsilon = \varepsilon_n(\tau_b - \tau_s) \tag{5.1.1}$$

where ε is the erosion rate in kg/m^2-s, τ_s is the sample shear strength in Pa, ε_N is the erosion rate constant in kg/N-s and τ_b is the shear stress in Pa. A summary of these results may be seen in Table 5.2. These trend lines were then made dimensionless as follows:

$$\frac{\varepsilon}{\varepsilon_n} = \frac{\tau_b - \tau_s}{\tau_s} \tag{5.1.2}$$

Table 5.2 Density, erosion rate constant, and shear strength values for 15 clay samples

Sample #	Density, ρ (kg/m^3)	ε_N (kg/m^2-s)	τ_s (Pa)
1	1665	5.00×10^{-5}	3.14
3	1710	1.91×10^{-5}	3.38
4	1859	1.23×10^{-5}	4.49
5	1928	1.73×10^{-5}	0.60
6	1928	1.20×10^{-5}	1.67
7	1435	3.93×10^{-5}	1.93
8	1537	1.19×10^{-5}	2.81
9	1721	7.72×10^{-5}	3.02
10	1894	7.00×10^{-5}	1.58
11	1905	7.10×10^{-6}	2.00
12	1675	4.80×10^{-5}	1.39
13	1698	3.22×10^{-5}	1.73
14	1806	1.14×10^{-5}	1.76
16	1940	6.89×10^{-5}	3.27
17	1963	9.85×10^{-6}	1.88

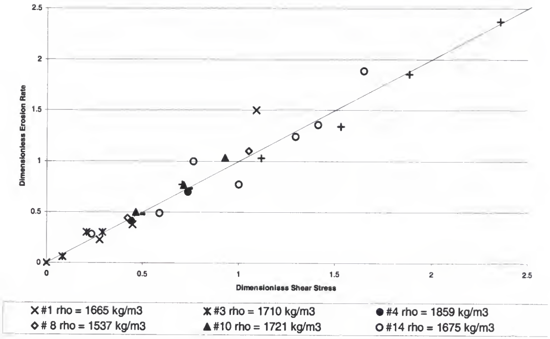

Figure 5.1 Dimensionless erosion rate as a function of dimensionless shear stress for the clay samples run in SERF.

It should be pointed out that the selected group of samples did not erode enough to significantly decrease the sample radius, and only one cylinder calibration curve was used for each sample. For example, sample #6, with a bulk density (wet) of 1928 kg/m^3, lost a total of 3 g during the entire test. This corresponds to a reduction in thickness of 0.007 cm, or 0.18% thickness lost (based on large cylinder volume).

5.2 Flume Experiments

After the flume was calibrated, it was run with the clays from Bennett Pottery Supply, the clays obtained from the EPK Division of Feldspar Corporation, and with the five angular quartz sands from the Feldspar Corporation. A total of 44 samples were tested, and the experimental conditions under which these samples were run are listed in Table 5.3.

Table 5.3 Summary of flume experimental conditions

Sample #	Sand Type	Clay Type	Fine Fraction	Pore Water	Bulk Density, (kg/m^3)	Applied Shear Stress (Pa)
1	N/A	Bennett Pottery #20	1.00	fresh	1232	0.13 - 0.79
2	N/A	Bennett Pottery #75	1.00	fresh	1259	0.16 - 0.52
3	N/A	Bennett Pottery #10	1.00	fresh	1240	0.09 - 0.84
4	N/A	Bennett Pottery #10	1.00	fresh	1288	0.14 - 0.88
5	#30	N/A	0.00	fresh	1850	0.10 - 0.59
6	#2	N/A	0.00	fresh	1850	0.10 - 0.63
7	#20	N/A	0.00	fresh	1850	0.20 - 0.93
8	F 8-20	N/A	0.00	fresh	1850	0.12 - 0.98
9	20-30	N/A	0.00	fresh	1850	0.12 - 0.75
10	F 8-20	Kaolinite	0.02	fresh	1832	0.12 - 1.40
11	F 8-20	Kaolinite	0.04	fresh	1886	0.11 - 0.99
12	F 8-20	Kaolinite	0.06	fresh	1895	0.12 - 0.99
13	F 8-20	Kaolinite	0.08	fresh	1911	0.12 - 0.59
14	F 8-20	Kaolinite	0.10	fresh	1974	0.12 - 0.80
15	20-30	Kaolinite	0.02	fresh	1770	0.12 - 0.56
16	20-30	Kaolinite	0.04	fresh	1851	0.12 - 0.49
17	20-30	Kaolinite	0.06	fresh	1912	0.12 - 0.28
18	20-30	Kaolinite	0.08	fresh	2013	0.12 - 0.41
19	20-30	Kaolinite	0.10	fresh	2022	0.12 - 0.42
20	20-30	Kaolinite	0.12	fresh	2086	0.12 - 0.78
21	20-30	Kaolinite	0.14	fresh	2128	0.12 - 1.33
22	20-30	Mixture #1	0.02	saline	1863	0.07 - 0.49
23	20-30	Mixture #1	0.04	saline	1951	0.12 - 0.70
24	20-30	Mixture #1	0.06	saline	2169	0.12 - 0.86
25	20-30	Mixture #1	0.08	saline	2416	0.12 - 1.81

Table 5.3 (continued)

Sample #	Sand Type	Clay Type	Fine Fraction	Pore Water	Bulk Density, (kg/m^3)	Applied Shear Stress (Pa)
26	20-30	Mixture #2	0.02	saline	1832	0.12 - 0.66
27	20-30	Mixture #2	0.04	saline	1903	0.12 - 0.65
28	20-30	Mixture #2	0.06	saline	2102	0.12 - 0.74
29	20-30	Mixture #2	0.08	saline	2394	0.12 - 1.07
30	20-30	Mixture #2	0.10	saline	2539	0.12 - 1.53
31	20-30	Kaolinite	0.02	saline	1853	0.12 - 0.63
32	20-30	Kaolinite	0.04	saline	2050	0.12 - 0.53
33	20-30	Kaolinite	0.06	saline	2140	0.12 - 0.48
34	20-30	Kaolinite	0.08	saline	2307	0.12 - 0.57
35	20-30	Kaolinite	0.10	saline	2417	0.12 - 0.68
36	20-30	Kaolinite	0.12	saline	2550	0.12 - 0.86
37	20-30	Kaolinite	0.14	saline	2574	0.12 - 0.96
38	#2	Kaolinite	0.02	fresh	1847	0.12 - 0.56
39	#2	Kaolinite	0.04	fresh	2057	0.12 - 0.20
40	#2	Kaolinite	0.06	fresh	2215	0.12 - 0.56
41	#2	Kaolinite	0.08	fresh	2301	0.12 - 0.50
42	#2	Kaolinite	0.10	fresh	2434	0.12 - 0.57
43	#2	Kaolinite	0.12	fresh	2554	0.12 - 0.72
44	#2	Kaolinite	0.14	fresh	2571	0.12 - 1.33

The flume was first run with the three different Bennett Pottery clay beds. The results from these runs may be seen in Figures 5.2 - 5.4. These results were used to check flume calibration as discussed in Section 5.4.

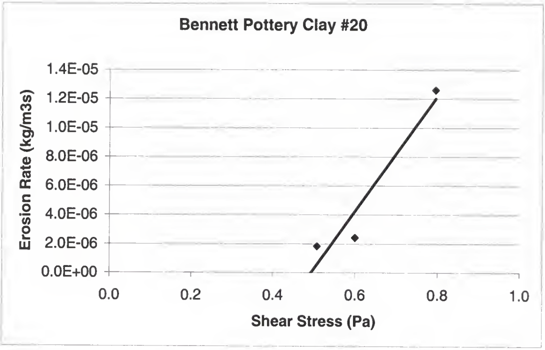

Figure 5.2 Erosion rate plot for Bennett Pottery Supply Clay #20.

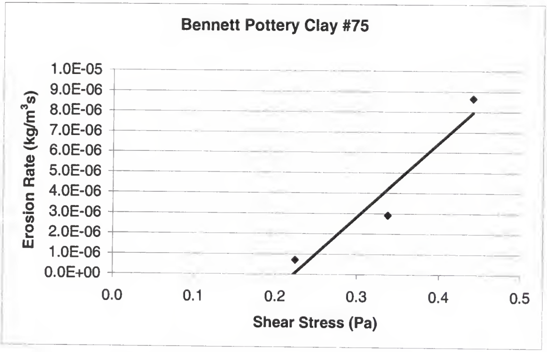

Figure 5.3 Erosion rate plot for Bennett Pottery Supply Clay #75.

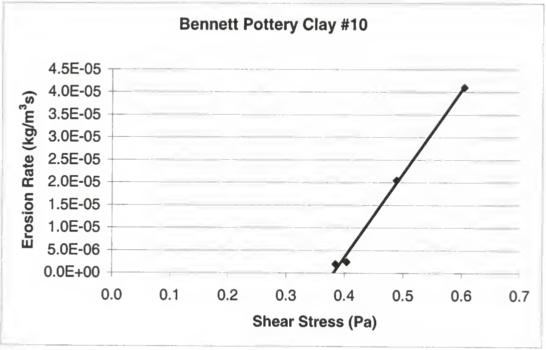

Figure 5.4 Erosion rate plot for Bennett Pottery Supply Clay #2

The flume was then run with the five different sand beds, each with a different median diameter (d_{50}), and the critical shear stress, as defined in Section 3.2, for each bed was determined. The fluid velocity, and consequently the bottom shear stress was increased incrementally until sand grain motion was observed to be restricted to isolated spots with a small number of grains moving briefly a few centimeters. After each increment of velocity change, the water surface height was recorded using the manometers to determine both the surface slope across the bed and the discharge through the sluice gate.

The critical shear stress, the Reynolds number, Re_*, and the critical Shields parameter, θ_{cr}, for each bed may be seen in Table 5.4. The critical Shields parameter for the cohesionless beds was plotted as a function of Re_*, and compared to values obtained by Mehta and Partheniades (1979), Panagiatopolous et. al. (1997), and Torfs (1995). Figure 5.5 shows the results from the flume to compare well with the results of these other authors.

Table 5.4 Critical shear stress, Reynolds number, and critical Shields parameter for sand beds

Sand Type	d_{50} (m)	Critical Shear Stress (Pa)	u_* (m/s)	Re*	θ_{cr}
# 2	0.00041	0.352	0.0187	7	0.0385
#30	0.00057	0.360	0.0190	10	0.0390
20-30	0.00083	0.498	0.0223	17	0.0371
#20	0.00094	0.609	0.0247	21	0.0400
F 8-20	0.0014	0.765	0.0277	35	0.0338

The flume was then used to test Samples 11 through 46 (Table 5.3). Results from these tests are seen in Figures 5.6 to 5.13. Figure 5.12 is a comparison plot of three different sediment beds, each with fresh kaolinite as the fine component and a different d_{50} for sand, to illustrate the effect of grain size on the behavior of the critical shear stress of the sand/kaolinite mixture. From this figure it can be seen that the $\psi_{\min}$ changes for each bed.

From Figure 5.12 it is seen that $\psi_{\min} = 0.045$ for $d_{50} = 0.41$ mm, $\psi_{\min} = 0.055$ for $d_{50} = 0.83$ mm, and $\psi_{\min} = 0.55$ for $d_{50} = 1.40$ mm, which indicates that the critical shear stress is not affected significantly by sand size.

Figure 5.13 is a comparison plot of four different sediment beds, each with the same d_{50} (= 0.83 mm) and a different clay, to illustrate the effect of clay on the critical shear stress for sand. It is seen that $\psi_{\min} = 0.06$ for the fresh kaolinite, $\psi_{\min} = 0.053$ for the saline kaolinite, $\psi_{\min} = 0.04$ for the clay mixture #1, and $\psi_{\min} = 0.03$ for the clay mixture #2, indicating the critical shear stress is affected by the cohesive component of sediment.

Finally, the minimum critical shear value, τ_{cs}, for each series of beds was used with Equation 3.3.34 to determine the critical Shields parameter, θ_{cr}, for each series and these values were then compared with those calculated for Figure 5.5. The values for the parameters in Equation 3.3.34 were the same as those given in Section 3.3 with the exception of $\Phi = 65^{\circ}$ and $\Phi_{eff} = 35^{\circ}$. This comparison may be seen in Figure 5.14.

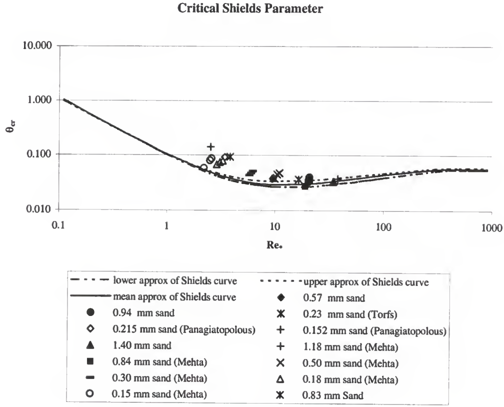

Figure 5.5 Comparison of critical Shields parameter of sand beds with the results of other researchers and with the Shields curve.

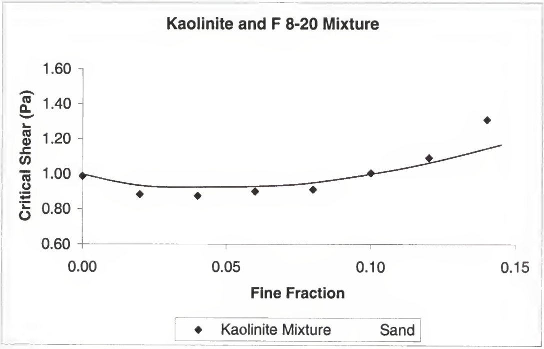

Figure 5.6 Plot of the behavior of the critical shear stress of the Feldspar F 8-20 and kaolinite with fresh pore water series of beds.

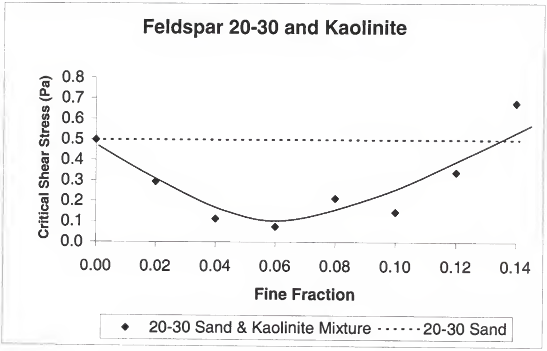

Figure 5.7 Plot of the behavior of the critical shear stress of the Feldspar F 20-30 and kaolinite with fresh pore water series of beds.

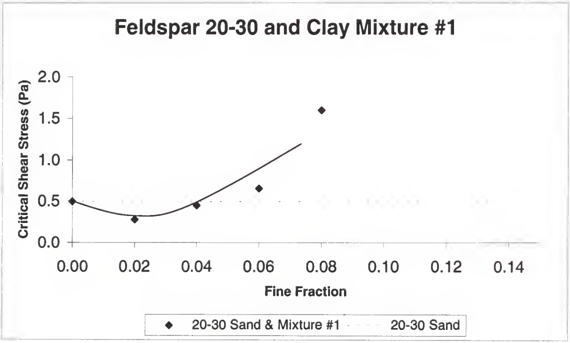

Figure 5.8 Plot of the behavior of the critical shear stress of the Feldspar F 20-30 and clay mixture #1 with 3 ppt. saline pore water series of beds.

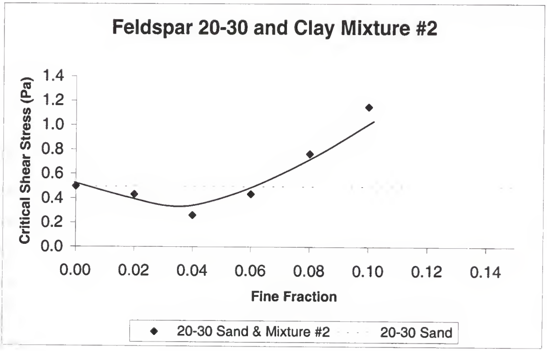

Figure 5.9 Plot of the behavior of the critical shear stress of the Feldspar F 20-30 and clay mixture #2 with 3 ppt. saline pore water series of beds.

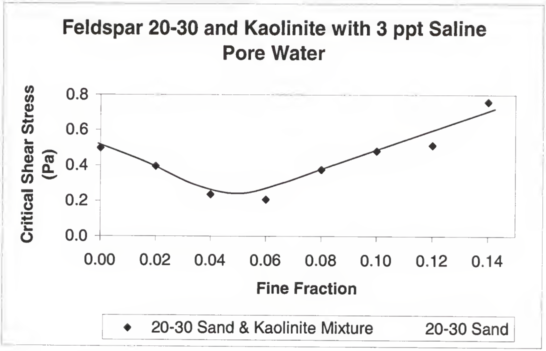

Figure 5.10 Plot of the behavior of the critical shear stress of the Feldspar F 20-30 and kaolinite with 3 ppt. saline pore water series of beds.

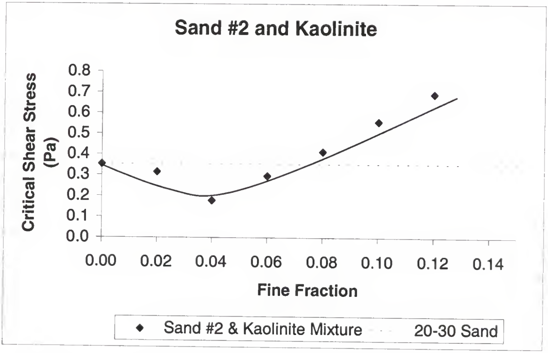

Figure 5.11 Plot of the behavior of the critical shear stress of the Sand #2 and kaolinite with fresh pore water series of beds.

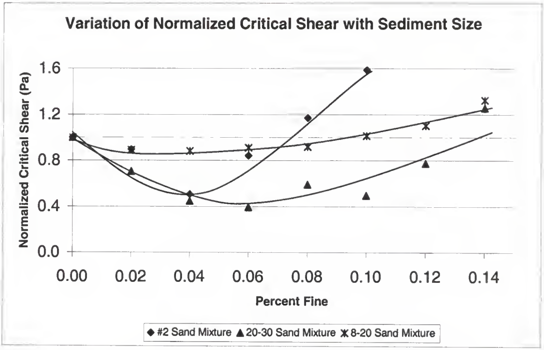

Figure 5.12 Variation of the normalized critical shear stress with fine weight fraction for three different sands.

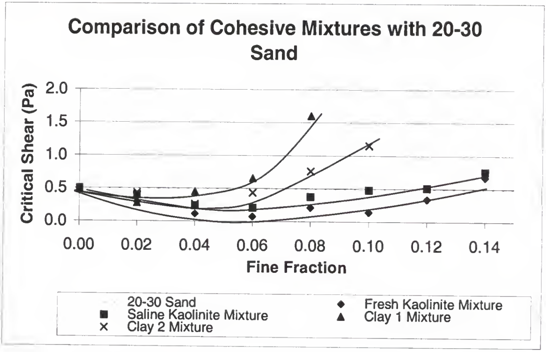

Figure 5.13 Variation of the critical shear stress with fine weight fraction for 20-30 sand and different clays.

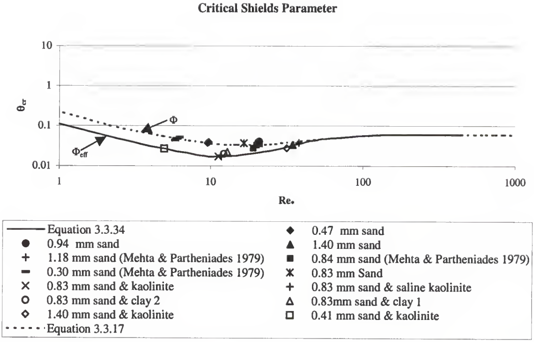

Figure 5.14 Comparison of the critical Shields parameter of sand beds with kaolinite calculated using Equation 3.3.34 compared with the results of Mehta and Partheniades (1979) and with the critical Shields parameter of sand beds without kaolinite calculated using Equation 3.3.17.

From Figure 5.14, it is seen that the introduction of clay particles in pore water to the sand grain matrix results in a significant decrease in the particle packing angle for the sand (from 65o to 35o), hinting at the mechanism causing the reduction in critical shear stress for sand. The particle packing angle, analogous to the angle of repose which is often referred to as the friction angle, by definition incorporates the effects of interparticle friction between the sand grains. Consequently, the reduction in this angle (from the introduction of interstitial clay particles) represents a lubrication between the sand grains.

5.3 Schulze Shear Tester Experiments

Sixty samples were tested in total, and for all but two samples whose shear stress values were less than the unconfined yield strength stress circle, reasonable values were detected by the shear cell. The experimental conditions under which these samples were tested are listed in Table 5.5.

Table 5.5 Schulze Shear Tester experimental conditions

Sample #	Sand Size (mm)	Clay Type	Fine Fraction	Pore Water	Preshear Load (g)	Applied Shear Stress (kPa)
1	0.41	Kaolinite	0.00	fresh	6000	0.00 - 6.23
2	0.41	Kaolinite	0.00	fresh	4000	0.00 - 4.50
3	0.41	Kaolinite	0.00	fresh	2000	0.00 - 2.49
4	0.41	Kaolinite	0.00	fresh	1000	0.00 - 1.81
5	0.41	Kaolinite	0.02	fresh	6000	0.00 - 7.03
6	0.41	Kaolinite	0.02	fresh	4000	0.00 - 4.90
7	0.41	Kaolinite	0.02	fresh	2000	0.00 - 2.37
8	0.41	Kaolinite	0.02	fresh	1000	0.00 - 1.93
9	0.41	Kaolinite	0.04	fresh	6000	0.00 - 7.35
10	0.41	Kaolinite	0.04	fresh	4000	0.00 - 5.28
11	0.41	Kaolinite	0.04	fresh	2000	0.00 - 2.44
12	0.41	Kaolinite	0.04	fresh	1000	0.00 - 1.88
13	0.41	Kaolinite	0.06	fresh	6000	0.00 - 5.51
14	0.41	Kaolinite	0.06	fresh	4000	0.00 - 4.51
15	0.41	Kaolinite	0.06	fresh	2000	0.00 - 2.18
16	0.41	Kaolinite	0.06	fresh	1500	0.00 - 1.67
17	0.41	Kaolinite	0.08	fresh	6000	0.00 - 6.75
18	0.41	Kaolinite	0.08	fresh	4000	0.00 - 4.29
19	0.41	Kaolinite	0.08	fresh	2000	0.00 - 3.18
20	0.41	Kaolinite	0.08	fresh	1500	0.00 - 1.57
21	0.41	Kaolinite	0.10	fresh	6000	0.00 - 5.31
22	0.41	Kaolinite	0.10	fresh	4000	0.00 - 3.95
23	0.41	Kaolinite	0.10	fresh	2000	0.00 - 2.03

Table 5.5 (continued)

Sample #	Sand Size (mm)	Clay Type	Fine Fraction	Pore Water	Preshear Load (g)	Applied Shear Stress (kPa)
24	0.41	Kaolinite	0.10	fresh	1500	0.00 - 1.56
25	0.41	Kaolinite	0.12	fresh	6000	0.00 - 5.12
26	0.41	Kaolinite	0.12	fresh	4000	0.00 - 3.56
27	0.41	Kaolinite	0.12	fresh	2000	0.00 - 1.89
28	0.41	Kaolinite	0.12	fresh	1500	0.00 - 1.49
29	0.41	Kaolinite	0.02	saline	6000	0.00 - 5.25
30	0.41	Kaolinite	0.02	saline	4000	0.00 - 3.74
31	0.41	Kaolinite	0.02	saline	2000	0.00 - 2.12
32	0.41	Kaolinite	0.02	saline	1500	0.00 - 1.69
33	0.41	Kaolinite	0.04	saline	6000	0.00 - 5.21
34	0.41	Kaolinite	0.04	saline	4000	0.00 - 3.80
35	0.41	Kaolinite	0.04	saline	2000	0.00 - 1.964
36	0.41	Kaolinite	0.04	saline	1500	0.00 - 1.58
37	0.41	Kaolinite	0.06	saline	6000	0.00 - 5.21
38	0.41	Kaolinite	0.06	saline	4000	0.00 - 3.68
39	0.41	Kaolinite	0.06	saline	2000	0.00 - 1.89
40	0.41	Kaolinite	0.06	saline	1500	0.00 - 1.48
41	0.41	Kaolinite	0.08	saline	6000	0.00 - 5.05
42	0.41	Kaolinite	0.08	saline	4000	0.00 - 3.59
43	0.41	Kaolinite	0.08	saline	2000	0.00 - 1.81
44	0.41	Kaolinite	0.08	saline	1500	0.00- 1.42
45	0.41	Kaolinite	0.10	saline	6000	0.00 - 4.86
46	0.41	Kaolinite	0.10	saline	4000	0.00 - 3.23
47	0.41	Kaolinite	0.10	saline	2000	0.00 - 1.77
48	0.41	Kaolinite	0.10	saline	1500	0.00 - 1.27
49	0.41	Kaolinite	0.12	saline	6000	0.00 - 4.64
50	0.41	Kaolinite	0.12	saline	4000	0.00 - 3.36
51	0.41	Kaolinite	0.12	saline	2000	0.00 - 1.72
52	0.41	Kaolinite	0.12	saline	1500	0.00 - 1.26
53	0.41	Kaolinite	0.01	fresh	6000	0.00 - 4.98
54	0.41	Kaolinite	0.01	fresh	4000	0.00 - 3.74
55	0.41	Kaolinite	0.01	fresh	2000	0.00 - 2.58

Table 5.5 (continued)

56	0.41	Kaolinite	0.01	fresh	1500	0.00 - 1.68
57	0.41	Kaolinite	0.01	saline	6000	0.00 - 5.13
58	0.41	Kaolinite	0.01	saline	4000	0.00 - 4.24
59	0.41	Kaolinite	0.01	saline	2000	0.00 - 2.12
60	0.41	Kaolinite	0.01	saline	1500	0.00 - 1.57

The Schulze shear tester was first run with the series of beds composed of Sand #2 and kaolinite with fresh pore water. The results from these runs are summarized in Table 5.6 and illustrated in Figure 5.15. The behavior of the friction factor for this series with change in the fine fraction may be seen in Figure 5.16. The shear tester was next run with the series of beds composed of Sand #2 and kaolinite with saline pore water. The results from these runs are first summarized in Table 5.7 and then illustrated in Figure 5.17. The behavior of the friction factor for this series with change in the fine fraction may be seen in Figure 5.18.

The friction factors were determined by extrapolating the critical shear stress back to a consolidation stress of 1000 Pa. The unconfined yield strength data for a given fine fraction was first plotted as a function of consolidation stress, calculated using the applied normal load and the area of the annular disk. This provided, for each fine fraction, a series of data points that could be used for a linear regression. The line was extrapolated backwards to determine the unconfined yield strength occurring at a consolidation stress of 1000 Pa, which was a consolidation stress much closer to that of a naturally occurring bed than what the ring shear tester could reproduce. The angle of internal friction for a given fine fraction occurring at 1000 Pa was determined using the same technique. Once these two values were known, the shear stress at incipient flow was calculated from

$$\tau_c = \frac{1}{2}\sigma_c \cos\varphi_i \tag{5.1}$$

where σ_c is the unconfined yield stress and φ_i is the angle of internal friction. From the shear stress the friction factor could be calculated from its definition:

$$f = \frac{\tau_c}{N} = \frac{\tau_c}{1000} \tag{5.2}$$

where N is the load. This process was repeated for each fine fraction, resulting in a series of data points for beds of Sand #2 with fresh kaolinite and Sand #2 with saline kaolinite.

Table 5.6 Schulze Shear Tester results for fresh kaolinite series

Fine Fraction	Consolidation Stress (g)	Unconfined Yield Strength, σ_c (kPa)	Angle of Internal Friction, φ_i	Shear Stress (kPa)
0.00	2497	1.791	38.35	0.702
0.00	4504	2.198	38.09	0.865
0.00	6234	2.193	37.94	0.865
0.01	1911	0.477	44.52	0.170
0.01	3527	0.581	43.97	0.209
0.01	5167	0.675	43.89	0.243
0.02	2132	0.551	44.59	0.196
0.02	3673	0.689	42.59	0.254
0.02	5376	0.826	41.53	0.309
0.04	2007	0.584	44.50	0.208
0.04	3423	0.713	42.60	0.262
0.04	5238	0.858	41.59	0.321
0.06	1682	0.586	45.11	0.207
0.06	2332	0.634	43.26	0.231
0.06	3582	0.776	42.51	0.286
0.06	5641	0.938	41.04	0.354
0.08	1569	0.894	39.04	0.347
0.08	4288	1.932	36.78	0.774
0.08	6755	3.053	33.40	1.274
0.10	1556	0.856	45.12	0.302
0.10	2032	0.962	40.73	0.364

Table 5.7 (continued)

0.10	3947	1.428	39.29	0.553
0.10	5309	1.399	38.87	0.545
0.12	1486	0.875	45.58	0.306
0.12	1895	0.982	45.28	0.345
0.12	3556	1.322	40.75	0.501
0.12	5117	1.376	39.50	0.531

Table 5.8 Shulze Shear Tester results for saline kaolinite

Fine Fraction	Consolidation Stress (g)	Unconfined Yield Strength, σ_c (kPa)	Angle of Internal Friction, φ_i	Shear Stress (kPa)
0.00	2497	1.791	38.35	0.702
0.00	4504	2.198	38.09	0.865
0.00	6234	2.193	37.94	0.865
0.01	2497	1.791	38.35	0.702
0.01	4504	2.198	38.09	0.865
0.01	6234	2.193	37.94	0.865
0.02	2123	0.651	44.39	0.233
0.02	3738	0.789	42.39	0.291
0.02	5254	0.926	41.03	0.349
0.04	1580	0.792	42.69	0.291
0.04	1964	0.877	44.27	0.314
0.04	3801	0.935	41.61	0.350
0.04	5214	0.968	41.26	0.364
0.06	1482	0.894	42.78	0.328
0.06	1893	1.039	46.10	0.360
0.06	3677	1.078	39.76	0.414
0.06	5209	1.203	39.73	0.463
0.08	1424	1.283	44.88	0.454
0.08	1806	1.300	40.76	0.492
0.08	3591	1.452	39.42	0.561
0.08	5055	1.525	40.20	0.582
0.10	1766	1.436	45.99	0.499
0.10	3323	2.424	40.06	0.928
0.10	4865	2.915	36.50	1.172
0.12	1264	1.638	38.63	0.640
0.12	1717	1.816	34.90	0.745
0.12	3362	2.291	38.20	0.900
0.12	4640	2.964	40.98	1.119

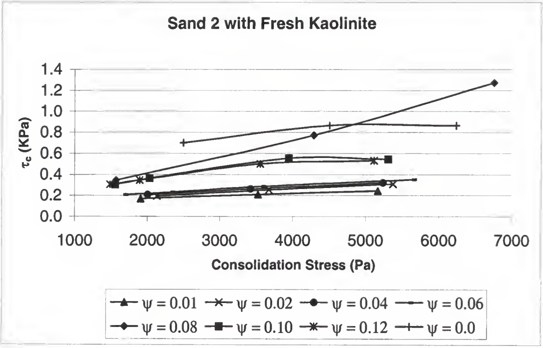

Figure 5.15 Comparison plot of the shear stress at incipient flow, τ_c, for the Sand #2 with fresh kaolinite series of beds.

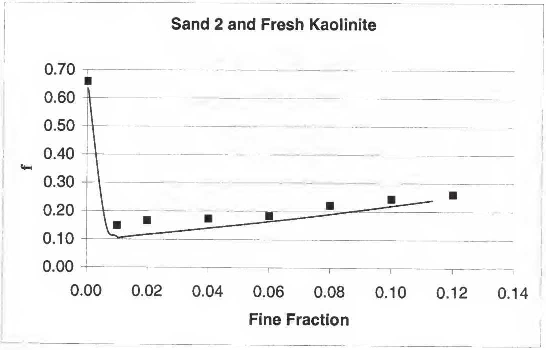

Figure 5.16 Plot of the friction factor at a consolidation stress of 1000 Pa as a function of ψ for the Sand #2 with saline kaolinite series of beds.

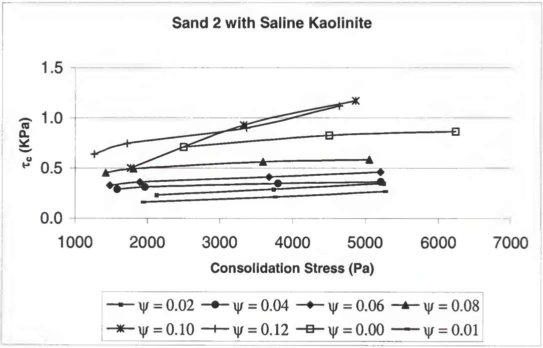

Figure 5.17 Comparison plot of the shear stress at incipient flow, τ_c, for the Sand #2 with saline kaolinite series of beds.

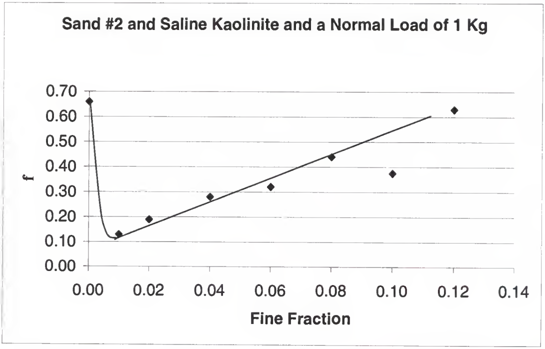

Figure 5.18 Plot of the friction factor at a consolidation stress of 1000 Pa as a function of ψ for the Sand #2 with saline kaolinite series of beds.

5.4 Comparison of SERF and Flume Data

The shear strengths clay samples used in both the SERF and the flume were plotted versus the dry density, and a fit of the following form (Mehta and Parchure, 2000) was applied to each clay type (Bennett Pottery #10, Bennett Pottery #20, Bennett Pottery #75):

$$\tau_s = C_1(\rho_d - \rho_l)^{C_2} \tag{5.3}$$

where C_1 and C_2 are empirical coefficients, ρ_d is the dry density in kg/m^3, and ρ_l is 64 kg/m^3 (selected to represent the dry density of fluid mud with no shear strength). For the #10 and #20 clays, $C_1 = 3.20 \times 10^{-3}$, and $C_2 = 1$, and for #75, $C_1 = 1.30 \times 10^{-3}$, and $C_2 = 1$ were obtained (Figures 5.19 through 5.21). Figure 5.22 is a comparison plot of the results for all three clay types. It was necessary to create beds of much lower density for the flume than those used in the SERF. Yet the flume results agree with those from the SERF. Consequently, it was concluded that the flume was accurately measuring the shear stress on the beds placed in it.

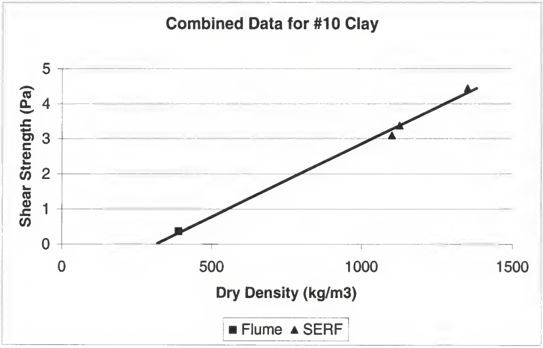

Figure 5.19 Comparison of values for shear strength for Clay #10.

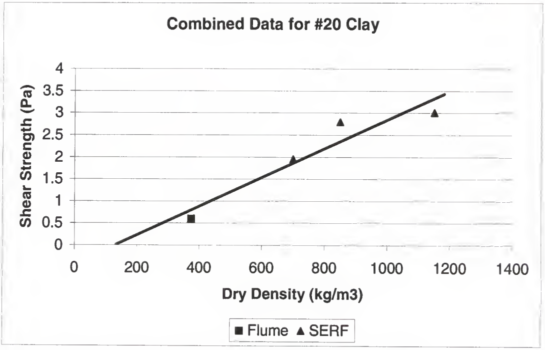

Figure 5.20 Comparison of values for shear strength for Clay #20.

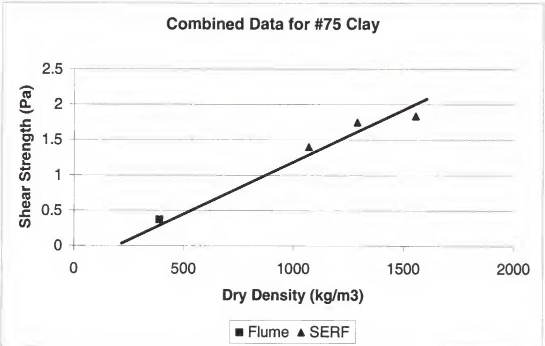

Figure 5.21 Comparison of values for shear strength for Clay #75.

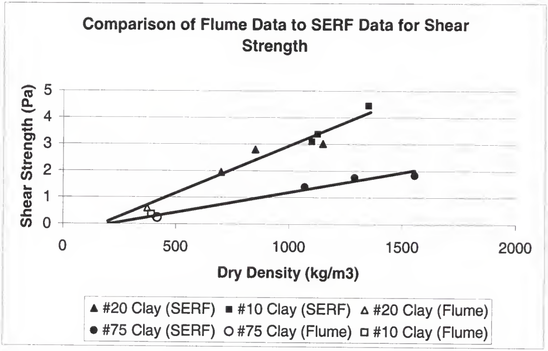

Figure 5.22 Summary plot of the comparison of the shear strength values.

CHAPTER 1
ANALYSIS OF RESULTS

6.1 Introduction

In Equation 3.3.34 for the critical shear stress $\overline{\tau}_{cr}$, or simply τ_{cr}, of sand influenced by the presence of clay, τ_{cr} has been shown to vary with the weight fraction ψ so that in the low range of ψ, τ_{cr} tends to decrease from τ_{co} for pure sand to τ_{cs} at some $\psi = \psi_{\min}$. τ_{cr} then increases with a further increase in ψ, passing through the point where it once again equals τ_{co} at ψ_r. This is trend illustrated in Figure 6.1. Table 6.1 summarizes the results from several experiments.

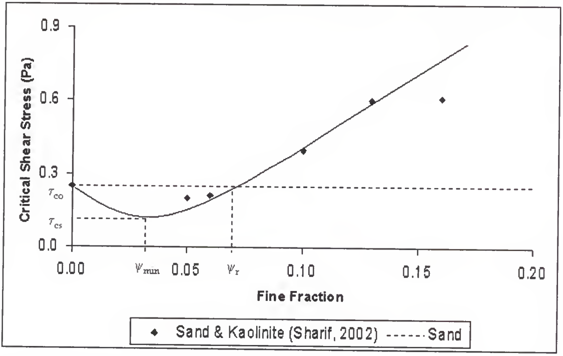

Figure 6.1 Schematic drawing of the effect of clay fraction on the critical shear stress for sand (Data of Sharif, 2002).

Table 6.1 Summarized data for τ_{co}, $\psi_{\min}$, τ_{cs}, and ψ_r

Investigator(s)	d_{50} (mm)	τ_{co} (Pa)	Clay type	$\psi_{\min}$	τ_{cs} (Pa)	ψ_r
Torfs (1995)	0.23	0.35	Scheldt Mud[a]	0.018	0.31	0.04
Torfs (1995)	0.23	0.35	Kaolinite	0.018	0.31	0.04
Torfs (1995)	0.23	0.35	Montmorillonite	0.028	0.33	0.07
Huygens and Verhofen (1996)	0.17	0.18	Kaolinite	0.036	0.15	0.05
Panagiotopoulos et. al. (1997)	0.15	0.32	Combwich mud[b]	0.022	0.30	0.11
Panagiotopoulos et. al. (1997)	0.22	0.35	Combwich mud	0.015	0.32	0.23
Sharif (2002)	0.20	0.22	Kaolinite (1.27 cm bed depth)	0.040	0.18	0.08
Sharif (2002)	0.20	0.22	Kaolinite (2.29 cm bed depth)	0.040	0.17	0.12
Present	1.40	0.99	Kaolinite	0.045	0.87	0.11
Present	0.83	0.70	Kaolinite	0.060	0.35	0.13
Present	0.83	0.70	Kaolinite (saline)	0.050	0.42	0.11
Present	0.83	0.70	Clay Mixture #2[c]	0.030	0.47	0.06
Present	0.83	0. 70	Clay Mixture #1[d]	0.020	0.50	0.04
Present	0.41	0.35	Kaolinite	0.036	0.20	0.07

[a] 55% illite, 30% smectite, 15% kaolinite

[b] 56% illite, 26% expansive clays (undefined), 11% kaolinite, and 7% chlorite

[c] 50% kaolinite, 35% attapulgite, and 15% bentonite

[d] 50% kaolinite, 45% attapulgite, and 5% bentonite

This work examines a physics-based explanation of the behavior of τ_{cr} under the premise that the interstitial clay particles alter grain-grain friction (and interlocking) between sand particles, and that the nature of lubrication is a function of ψ. This explanation is accomplished through the use of two different hypotheses. In the following sections, these hypotheses are presented first, and then the two are compared to determine their relative merits.

6.2 Quasi-Hydrodynamic Model for Sand Lubrication

In an effort to explain the interaction between the sand grains and the fine fraction, a mechanism of clay flow that possesses some of the features of hydrodynamic lubrication is considered. The basic feature of this quasi-hydrodynamic flow is an *in situ* layered flow of a clay film between two sand grains, portrayed schematically in Figure 6.2.

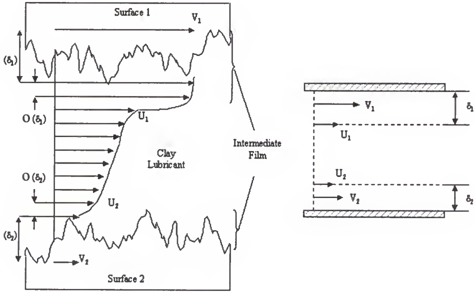

Figure 6.2 Schematics of the layered flow of a clay film between the surfaces of two sand grains where δ_1 and δ_2 are the roughness of the two surfaces (Heshmat and Brewe, 1995).

The behavior of two surfaces that begin to slide with respect to each other is strongly modified with the introduction of a lubricant between them. For example, if for two such surfaces we plot the coefficient of friction f against the ratio $\mu U/P$, where μ is the lubricant viscosity, U is the relative velocity of the one surface moving against the other, and P is the specific load, we find three different lubrication regimes (Szeri, 1998). This is illustrated in Figure 6.3.

At large values of $\mu U/P$ f is low and is proportional to $\mu U/P$. This is the regime of thick-film lubrication. It occurs when the film thickness exceeds roughly 2.5 μm and is approximately described by Petroff's law (Shigley and Mischke, 1989). Within this regime, f is dependent on μ. With decreasing $\mu U/P$, f passes through a minimum, as indicated schematically in Figure 6.3, and the behavior enters the regime of thin-film lubrication. In this regime, the film becomes thinner and some of the opposing asperities (roughnesses) touch. f now depends on the surface roughness, the properties of the solids, and the properties of the lubricant . With a decrease in $\mu U/P$, f passes into the boundary lubrication regime, in which the film is so thin that its properties are no longer the same as those of the bulk. If U or μ is reduced or P increased, the film becomes thinner than the height of some of the asperities. If these asperities are covered by a suitable molecular layer of lubricant, they will not weld together (Szeri, 1998).

The model of clay lubrication in Figure 6.2 permits an evaluation of the performance of clay lubrication in quantitative terms. In an incipient sliding contact between two sand grains with clay lubrication showing an infinitesimal section of it in the sliding direction, the film can be divided into regions of intermediate films and clay lubricant film. Intermediate films are of the order of surface roughness elements, the asperities, of the sand grains. In the present study it was observed visually that the surfaces of the sand particles in the beds tested were covered with thin adhered layers of clay almost immediately upon mixing the two sediment types together.

As may be seen in the schematic model of Figure 6.2, due to clay-induced lubrication an intermediate film acting as a boundary layer is created between the interacting sand grain surfaces and the clay lubricant film. A transition between the velocities of the two sand grains (V_1 and V_2, where the subscript "1" represents the top sand grain and subscript "2" represents the bottom sand grain) and the velocities of the edge of the lubricant film (U_1 and U_2) occurs across this intermediate film. This intermediate layer has the flexibility of behaving either as a solid or as a semi-solid in which creep occurs, which makes the transition of flow velocities from V_1 to U_1 and V_2 to U_2 possible, as shown in Figure 6.2. Figure 6.4 illustrates this quasi-hydrodynamic flow.

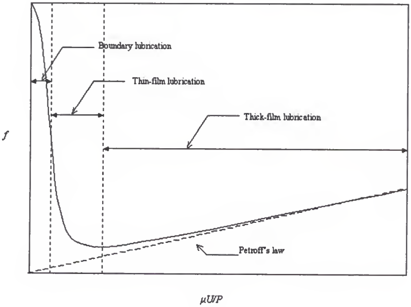

Figure 6.3 Lubrication regimes.

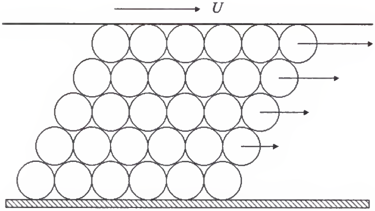

Figure 6.4 Quasi-hydrodynamic model of sand lubrication film.

Hydrodynamic lubrication is frequently explained through the application of Couette flow to a slider bearing. Figure 6.5 is an illustration of a simplified slider bearing. The same technique may be used here if two sand grains are represented in the analogous fashion. As illustrated in Figure 6.6, the upper sand grain can be shown to be the slider block, and the lower to be the reference surface (or pad).

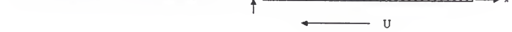

Figure 6.5 Slider bearing moving to right at speed *U* above stationary pad (a), and transformed to stationary block and pad moving to the left at speed *U* (b).

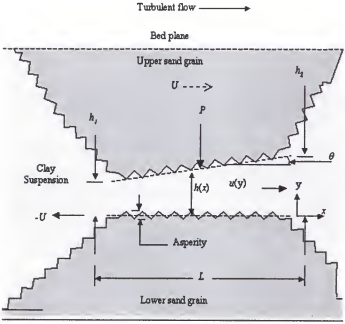

Figure 6.6 Flow of interstitial clay suspension viewed as slider bearing.

With reference to Figure 6.6, we will consider the problem in the *x*-*y* plane, treating the grains as if they were of unit thickness in the third dimension. Consider that the upper sand grain is set in motion at a velocity *U* by a turbulence-induced instantaneous shear stress at the exposed bed plane.

We may conveniently consider the short duration over which this shear acts to be long enough for the forces to be in equilibrium. Einstein and El Samni (1949) found that the pressure fluctuations (used to calculate the average lift on an individual sand grain as discussed in Section 2.2) had a predominant period of approximately 1/50th of a second. These researchers also reported the lift pressure as a function of duration, which can be used to determine a reference instantaneous lift pressure. A lift pressure (10.05 kg/m^2) occurring only 3% of the time is chosen so as to obtain a maximum value for the instantaneous lift pressure. Through Equations 3.3.8 and 3.3.12, it is seen that both the shear stress and the lift per unit area are proportional to the same flow properties and should, as a result, be of the same order of magnitude. Consequently, this maximum instantaneous lift pressure may be used to determine a maximum value for the instantaneous load on a single 0.83 mm sand grain (found to be 0.022 g) that is also representative of the maximum value for the instantaneous shear stress on an individual grain of the same diameter. The above load value was determined as follows:

Instantaneous Lift Pressure = (0.0100584 m water)(1000 kg/m^3) = 10.05 kg/m^2

Instantaneous Load = (10.05 kg/m^2)(π)(0.00083 m)^2 = 0.0217g

Now, due to the non-parallel orientation of the upper and the lower grain surfaces separated by a viscous clay suspension of small thickness, i.e., $h(x)/L \ll 1$ where h is O(10^1 μm) and L is O(10^3 μm), the resulting pressure gradient over distance L will cause the suspension to flow. If we choose the upper grain to be stationary, the lower one to translate at a velocity $-U$, and apply Couette flow, then for small values of angle θ a velocity profile in the suspension may be derived.

Starting with the continuity equation (considering only the x-y plane)

$$\frac{\partial u}{\partial x}+\frac{\partial v}{\partial y}=0 \qquad (6.2.1)$$

and using the following dimensionless variables,

$$\begin{aligned} u_* &= \frac{u}{U} & x_* &= \frac{x}{L} \\ v_* &= \frac{v}{V} & y_* &= \frac{y}{h} \end{aligned} \qquad (6.2.2)$$

where V is the maximum velocity in the y-direction, the continuity equation can be expressed in the following form

$$U\frac{\partial u_*}{\partial x_*}+\left(\frac{L}{h}\right)V\frac{\partial v_*}{\partial y_*}=0 \qquad (6.2.3)$$

It is assumed θ is very small, or h/L is very small ($h<<L$). Consequently, for the two terms of Equation 6.2.3 to be of the same order, $v << u$ since $L/h >> 1$. The momentum equations are:

$$x:\quad \rho u\frac{\partial u}{\partial x}+\frac{\partial p}{\partial x}=\mu\left(\frac{\partial^2 u}{\partial x^2}+\frac{\partial^2 u}{\partial y^2}\right) \qquad (6.2.4)$$

$$y:\quad \frac{\partial p}{\partial y}=0 \qquad (6.2.5)$$

The x-direction momentum equation can be made non-dimensional as follows

$$u_*\frac{\partial u_*}{\partial x_*}+\left(\frac{p_0}{L}\right)\frac{\partial p_*}{\partial x_*}=\left(\frac{\mu}{\rho UL}\right)\frac{\partial^2 u_*}{\partial x_*^2}+\left(\frac{\mu}{\rho UL}\right)\left(\frac{L}{h}\right)^2\frac{\partial^2 u_*}{\partial y_*^2} \qquad (6.2.6)$$

where $p_* = p/p_o$ and p_o is the ambient pressure in the clay suspension. Substituting the definition for the Reynolds number ($\mathrm{Re}=\rho UL/\mu$) into Eq. 6.2.6 gives the following expression

$$u_*\frac{\partial u_*}{\partial x_*}+\left(\frac{p_0}{L}\right)\frac{\partial p_*}{\partial x_*}=\left(\frac{1}{\mathrm{Re}}\right)\frac{\partial^2 u_*}{\partial x_*^2}+\left(\frac{1}{\mathrm{Re}}\right)\left(\frac{L}{h}\right)^2\frac{\partial^2 u_*}{\partial y_*^2} \qquad (6.2.7)$$

Since $L/h >> 1$, and since this is laminar flow ($\mathrm{Re} < 10^4$), it can be seen that the first and third terms of Equation 6.2.7 will be much smaller than the rest. The first term will be $O(1)$ and the third term $O(1/\mathrm{Re})$, whereas the second term $O(p_o/L)$ and the fourth term is $O(L^2/h^2)$. Consequently, the first and third terms can be neglected. This leads to a thin layer flow approximation in which gradients across the flow in the narrow direction are much greater than gradients along the flow:

$$\frac{\partial p}{\partial x} = \mu \frac{\partial^2 u}{\partial y^2} \tag{6.2.8}$$

which is very similar to Couette flow. The only difference is that now $\partial p/\partial x$ depends on x [since u is f(x,y)].

The boundary conditions for the fluid velocities are:

$$\begin{aligned} u &= -U \quad @ \quad y = 0 \\ u &= 0 \quad @ \quad y = h \end{aligned} \tag{6.2.9}$$

and when applied to Equation 6.2.8 result in

$$u = -U\left(1 - \frac{y}{h}\right) - \frac{h^2}{2\mu}\frac{dp}{dx}\frac{y}{h}\left(1 - \frac{y}{h}\right) \tag{6.2.10}$$

From Equation 6.2.10 the (short-duration steady) discharge Q is given by:

$$Q = \int_0^h u\,dy \tag{6.2.11}$$

or

$$Q = \frac{-Uh}{2} - \frac{h^3}{12\mu}\frac{dp}{dx} \tag{6.2.12}$$

giving for dp/dx

$$\frac{dp}{dx} = \frac{-12\mu}{2}\left(\frac{Uh}{2} + Q\right) \tag{6.2.13}$$

The boundary conditions for the pressure are

$$p = p_o \quad @ \quad x = 0, L$$

where p_o is the pressure in the clay suspension at both $x = 0$ and $x = L$. Applying these boundary conditions for the pressure, an expression relating U and Q through geometry is obtained

$$Q = -\frac{U}{2}\frac{\int_0^L \frac{dx}{h^2}}{\int_0^L \frac{dx}{h^3}} \tag{6.2.14}$$

Using geometry to express h as a function of x gives

$$h = h_1 + (h_2 - h_1)\frac{x}{L} \qquad \tan\theta = \frac{h_1 - h_2}{L} \tag{6.2.15}$$

Substituting Equation 6.2.15 into 6.2.14 gives

$$Q = -\frac{Uh_o}{2} \tag{6.2.16}$$

where

$$h_o = \frac{2h_1h_2}{h_1 + h_2} \tag{6.2.17}$$

so that

$$\frac{dp}{dx} = -\frac{6\mu U}{h^3}(h - h_o) \tag{6.2.18}$$

Substituting Equation 6.2.18 into 6.2.10, we obtain

$$u = -U\left(1 - \frac{y}{h}\right) + \frac{h^2}{2\mu}\frac{6\mu U}{h^3}\frac{y}{h}(h - h_o)\left(1 - \frac{y}{h}\right) \tag{6.2.19}$$

which may be simplified to

$$u = -U\left(1 - \frac{y}{h}\right) + \frac{3Uy}{h^2}(h - h_o)(h - y) \tag{6.2.20}$$

or

$$u = -U\left(1 - \frac{y}{h}\right) + \frac{3Uy}{h^2}(h^2 - h_oh - hy + h_oy) \tag{6.2.21}$$

or

$$u = -U + \frac{Uy}{h} + \frac{3Uy}{h} - \frac{3Uyh_o}{h^2} - \frac{3Uy^2}{h^2} + \frac{3Uh_o y^2}{h^3} \qquad (6.2.22)$$

Substituting Equation 6.2.16 into 6.2.22 gives

$$u = -U + \frac{4Uy}{h} + \frac{6Qy}{h^2} - \frac{3Uy^2}{h^2} - \frac{6Qy^2}{h^3} \qquad (6.2.23)$$

which can be seen to be

$$u(y) = -U + \left(\frac{4U}{h} + \frac{6Q}{h^2}\right)y - \left(\frac{3U}{h^2} + \frac{6Q}{h^3}\right)y^2 \qquad (6.2.24)$$

In obtaining Equation 6.2.24 it is assumed that the grain asperities are of negligible height, i.e., grains have smooth surfaces, so that they do not significantly effect the flow. The shear force F on the lower grain is obtained from

$$F = \int_0^L \mu \left.\frac{du}{dz}\right|_{z=0} dx = \frac{\mu}{(k-1)h_L}\left[4\ln k - 6\frac{k-1}{k+1}\right]UL = K_1 UL \qquad (6.2.25)$$

where μ is the viscosity of the suspension, $k = h_2/h_1$ and

$$K_1 = \frac{\mu}{(k-1)h_L}\left[4\ln k - 6\frac{k-1}{k+1}\right]$$

Hence the coefficient of friction f is obtained as

$$f = \frac{F}{P} = K_1\left(\frac{\mu U}{P}\right) \qquad (6.2.26)$$

which is Petroff's law for thick-film lubrication (Figure 6.3).

As $\mu U/P$, a measure of horizontal viscous force relative to normal load, decreases f will decrease until h approaches $O(10^{-1}\text{-}10^{0})$ µm, the size of clay particles. Hence f will increase with a further decrease in $\mu U/P$ in the zone of thin-film lubrication. Finally, there will be a further and rapid rise in f (boundary lubrication) as the film becomes so thin that its properties are no longer those of the bulk and abrasion/interlocking due to clay particles and asperities, $O(10^{-1})$ μm, takes over. In accordance with this quasi-hydrodynamic behavior Equation 6.2.26 is extended to yield

$$f = K_1\left(\frac{\mu U}{P}\right) + K_2 e^{-K_3\left(\frac{\mu U}{P}\right)} \qquad (6.2.27)$$

in which K_2 and K_3 characterize thin-film and boundary layer lubrication. Eq. 6.2.26 is recovered when $K_2 = 0$.

From a reanalysis of the data of Heshmat and Brewe (1996) using *dry* Molybdenum sulfide powder as a lubricant for journal bearings, mean values were obtained for $K_1 = 0.0431$, $K_2 = 1.00$ and $K_3 = 0.31 - 2.2$, as shown in Figure 6.7.

As previously discussed in Sections 4.2, 4.5, and 5.5, 46 different sediment beds were subjected to increasing water flow until incipient motion of sand grains occurred. As a specific example, in runs 17-23 and 32-39 (listed in Table 5.3), 840 μm quartz sand mixed with 1 μm kaolin was tested. In runs 17-23, the pore water was fresh and in runs 32-39 it was pre-equilibrated with 3 ppt solution of NaCl in water. A salinity of 3 ppt was specifically chosen for the kaolinite flocculation properties discussed subsequently. A comparison plot of the results of both of these series of runs may be seen in Figure 6.8. All of the results, which are shown in Figures 5.9 to 5.16 and 6.8, seemingly mimic the behavior of Equation 6.2.27 which is illustrated in Figure 6.3.

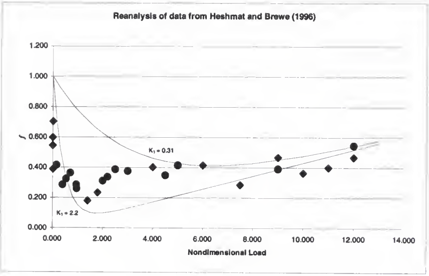

Figure 6.7 Plot of Equation 6.2.27 applied to the data of Heshmat and Brewe (1996).

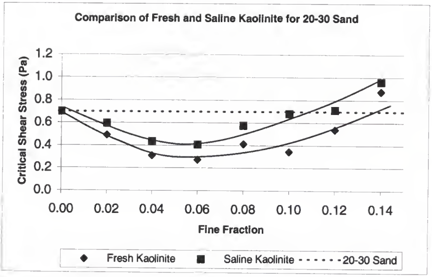

Figure 6.8 Comparison plot of both series of kaolinite and 20-30 sand tests.

Referring to Equation 6.2.27, from Engelund and Zhaohui (1984) the viscosity of hyper-concentrated flows of kaolinite is given by

$$\mu = 0.001 + 0.206C^{1.68} \tag{6.2.28}$$

where C is the volume concentration of the suspension expressed as a dimensionless fraction, and μ is in Ns/m^2. The pore water kaolinite suspension concentrations in the present study ranged from 0.00 to 0.37. These ranges were obtained by using the following expression

$$C = \frac{\rho_d}{\rho_{sc}} = \frac{\dfrac{m_c}{V_c + V_w}}{\dfrac{m_c}{V_c}} = \frac{V_c}{V_t} \tag{6.2.29}$$

where ρ_d is the dry density, ρ_{sc} is the granular density of the clay, m_c is the mass of the clay, V_c is the volume of the clay, and V_w is the volume of the water. The concentration, C, is related to ψ, where ψ is defined as follows

$$\psi = \frac{m_c}{m_s + m_c + m_w} = \frac{\rho_{sc}(1 - n_c)V_c}{\rho_s V_s + \rho_{sc}(1 - n_c)V_c + \rho V_w} \tag{6.2.30}$$

where m_s is the mass of the sand, V_s is the volume of sand, ρ_s is the granular density of the sand, V_w is the volume of the pore water, and n_c is the porosity. Solving Equation 6.2.30 for V_c results in the following expression

$$V_c = \frac{\psi(\rho_s V_s + \rho V_w)}{\rho_{sc}(1 - n_c)(1 - \psi)} \tag{6.2.31}$$

Substituting Equation 6.2.31 into 6.2.29 results in

$$C = \frac{\psi(\rho_s V_s / V_t + \rho V_w / V_t)}{\rho_{sc}(1 - n_c)(1 - \psi)} \tag{6.2.32}$$

However, if it is assumed within the range of fine fraction used for this study, that the contribution of the volume of clay to the total volume, V_t, is negligible, the volume ratios can be refined as follows:

$$\begin{aligned}\frac{V_s}{V_t} &= \frac{V_s}{V_s + V_c + V_w} = \frac{V_s}{V_s + V_w} = 1 - n_s \\ \frac{V_w}{V_t} &= \frac{V_w}{V_s + V_c + V_w} = \frac{V_w}{V_s + V_w} = n_s\end{aligned} \qquad (6.2.33)$$

where n_s is the porosity of the sand grain matrix. This assumption is shown to be valid in subsequent sample calculations. If these ratios are substituted back into Equation 6.2.32, the following expression results relating C to ψ:

$$C = \frac{[\rho_s(1-n_s) + \rho n_s]\psi}{\rho_{sc}(1-n_c)(1-\psi)} \qquad (6.2.34)$$

which is valid for the range of fine fraction used in this study. Assuming $\rho_s = \rho_{sc} = 2.65\text{x}10^{-6}$ kg/mm^3, $\rho = 1.00\text{x}10^{-6}$ kg/mm^3, $n_c = 0.48$ (this value is discussed subsequently), $n_s = 0.50$ (taken from Hough, 1957, for clean, uniform surface sand), and $\psi = 0.16$ (the upper range of fine fraction used in this study), Equation 6.2.34 gives $C = 0.37$ as the upper range of concentration for this work. The viscosity consequently varied as follows:

$$\begin{aligned}\mu &= 0.001 + 0.206(0.0)^{1.68} = 0.001 \\ \mu &= 0.001 + 0.206(0.37)^{1.68} = 0.040\end{aligned} \quad \text{Ns/m}^2$$

The flow-induced drag coefficient is

$$C_D = \frac{\tau_{cr}}{\rho u_{cr}^2} \qquad (6.2.35)$$

where ρ is water density and u_{cr} is the critical velocity. If we consider u_{cr} to be invariant, then since f can be considered to be related to C_D, the variation of f can in turn be considered to qualitatively reflect the variation of τ_{cr}. By substituting Equation 6.2.34 into Equation 6.2.29, viscosity μ is seen to vary with ψ as follows

$$\mu = 0.001 + 0.206\left\{\frac{\left[\rho_s(1-n_s)+\rho n_s\right]\psi}{\rho_{sc}(1-n_c)(1-\psi)}\right\}^{1.68}$$

Thus the behavior of μ, and consequently $\mu U/P$, can be considered to reflect the behavior of ψ. Therefore, the variation of f with $\mu U/P$ is seen to be qualitatively analogous to the variation of τ_{cr} with ψ.

6.3 Effect of Pore Water Salinity

From Figure 6.8 we note that $\tau_{co} = 0.70$ Pa. Further, for saline water $\tau_{cs} = 0.42$ Pa at $\psi_{\min} \approx 0.05$, and for fresh water $\tau_{cs} = 0.35$ Pa also at $\psi_{\min} \approx 0.06$. From the corresponding $\tau_{cs}/\tau_{co} = 0.6$ and 0.5, we may infer that kaolin in fresh water provides ~17% greater lubrication than in saline water, and that $\psi \approx 0.06$ marks the transition between thin-film and thick-film lubrication. Both of these trends, the location of $\psi_{\min}$ and the reduction in τ_{cs} with fresh pore water, are explained by the quasi-hydrodynamic model of clay lubrication.

The lubricating effect of kaolinite in pore water is determined by the orientation of the individual plate-like particles. Kaolinite is characterized by particles of relatively large size and a low cation exchange capacity in comparison to other clay minerals. For example, the length and thickness of typical kaolinite particles are 1 μm and 0.1 μm, respectively, compared with equivalent dimensions of 0.1 and 0.01 μm, respectively, for montmorillonite.

Clay particles have a negative charge on the surface and a positive charge on the edges. Hence, certain clays can be flocculated by edge to face mechanisms (Figure 6.9) under a state of non-salt flocculation. The addition of salt in the suspending medium increases the concentration of negatively charged ions which gather at the edges of the particles and thus make the edges less effective in flocculation. Consequently, a greater degree of parallelism results with salt-flocculation (Figure 6.10). The structure of clay with edge-to-face contacts of particles is more open and has lower shear resistance than that of a more compact structure with face-to-face contact of particles (Lambe and Whitman, 1969).

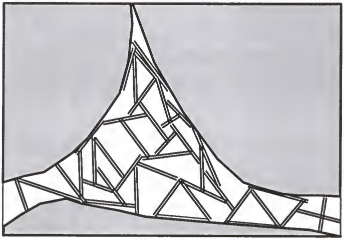

Figure 6.9 Freshwater flocculation in pore water with edge-to-face contacts.

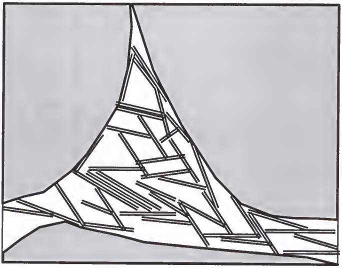

Figure 6.10 Saltwater flocculation with particle orientation approaching parallelism.

Both of these types of flocculation are observed in the case of kaolinite in water at different salt concentrations. Kaolinite in fresh water flocculates by the edge-to-face mechanism, as illustrated in Figure 6.9, resulting in a very weak particle matrix. The presence of concentrations of salt in the suspending fluid (greater than approximately 1 ppt), like the concentration (3 ppt) used in this study, results in salt-flocculation of the type illustrated in Figure 6.10. In this case a matrix of lower density and shear strength than the low-salt case results, but still having greater density and shear strength than with fresh water flocculation (Lambe and Whitman, 1969).

The addition of salt at 3 ppt concentration resulted in a matrix that was both denser and stronger, and as a result had a viscosity higher than the case with fresh water pore water. From Wasp et al. (1977), the effective viscosity of Bingham plastic fluid is given as

$$\mu_e = \frac{\tau_o D_p}{6U_t} \tag{6.3.1}$$

where τ_o is the yield stress, D_p is the pipe diameter, and U_t is the transition velocity. This expression may be used to determine the ratio of the effective viscosity of saline kaolinite to the effective viscosity of fresh kaolinite

$$\frac{\mu_{es}}{\mu_{ef}} = \frac{\tau_{os}}{\tau_{of}} \tag{6.3.2}$$

where the subscript "*s*" represents saline kaolinite, and the subscript "*f*" represents fresh kaolinite. From the work of Einstein (1941), this ratio is found to be 40:1. Equation 6.3.32 can then be combined with Equation 6.2.28 to determine the viscosity of saline kaolinite as follows

$$\mu_{es} = \frac{\tau_{os}}{\tau_{of}}\left(0.001 + 0.206C^{1.68}\right) = (40)\left[0.001 + 0.206(0.37)^{1.68}\right] = 1.6 \text{ Ns/m}^2 \quad (6.3.3)$$

(The quasi-hydrodynamic model then would predict this bed to have a higher friction factor, since in the thick-film region of lubrication Equation 6.2.27 is essentially governed by Petroff's law where the friction factor is directly proportional to the viscosity. With an increase in viscosity, as in the comparison of the fresh water kaolinite to saline kaolinite illustrated in Figure 6.8, Equation 6.2.27 would result in an increase in friction factor.

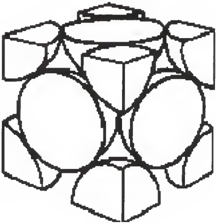

Figure 6.11 Face-centered cubic unit cell.

If we assume that sand grains are hexagonally close-packed in the bed, we can determine both the number of layers of clay particles and the total thickness of the layers within the pore water of the resulting face-centered unit cube (Figure 6.11) that will provide lubrication between sand grains at ψ_{min}. As may be seen in Figure 6.11, in this structure the grains touch along the diagonals for each face (and not along the edges of the cube). The length of the diagonal is $r_g + 2r_g + r_g$, or $4r_g$, where r_g is the sand grain radius. Hence the edge length is $r_g\sqrt{8}$. Since the net number of sand grains in the face-centered cubic unit cell is 4, the total volume occupied by the pore fluid is the total volume of the cell $\left(r_g\sqrt{8}\right)^3$ minus the volume occupied by the four sand grains $4(4/3)(\pi r_g^3)$, or $\left[\left(r_g\sqrt{8}\right)^3 - 4(4/3)(\pi r_g^3)\right]$.

A face-centered cubic structure with a sand grain having a diameter of 0.83 mm, a clay particle size of 1μm, and a fine grain fraction of 0.066, will have a clay layer approximately 20 μm thick and will consequently have approximately 20 layers of clay particles. This calculation is given below:

$$\mathrm{V_{total}} = \left(0.415\sqrt{8}\right)^3 = 1.62\mathrm{mm}^3$$

$$\mathrm{V_{sand}} = 4\left(\frac{4}{3}\right)\pi(0.415)^3 = 1.20\mathrm{mm}^3$$

$$\mathrm{V_{clay}} = 4\left(\frac{4}{3}\right)\pi\left[(0.415 + 0.02)^3 - (0.415)^3\right] = 0.182\mathrm{mm}^3$$

$$\mathrm{V_{pore}} = \mathrm{V_{total}} - \mathrm{V_{sand}} - \mathrm{V_{clay}} = 0.24\mathrm{mm}^3$$

$$\psi = \frac{2.65\mathrm{x}10^{-6}(1 - 0.48)\mathrm{V_{clay}}}{2.65\mathrm{x}10^{-6}\,\mathrm{V_{sand}} + 2.65\mathrm{x}10^{-6}(1 - 0.48)\mathrm{V_{clay}} + 1.00\mathrm{x}10^{-6}(0.48)\mathrm{V_{clay}} + 1.00\mathrm{x}10^{-6}\,\mathrm{V_{pore}}} = 0.066$$

assuming $\rho_{\mathrm{clay}} = \rho_{\mathrm{sand}} = 2.65\mathrm{x}10^{-6}$ kg/mm^3, $\rho_{\mathrm{w}} = 1.00\mathrm{x}10^{-6}$ kg/mm^3, the porosity of the clay = 0.48:

$$n_c = \frac{\rho_{\mathrm{b}}\mathrm{V_{tot}} - m_{\mathrm{c}}}{\rho\left(\mathrm{V_{tot}} - m_{\mathrm{c}}/\rho_{\mathrm{sc}}\right)} = \frac{\left(1850\,\mathrm{kg/m^3}\right)\left(0.005984\,\mathrm{m^3}\right) - 10.001\,\mathrm{kg}}{\left[\left(1000\,\mathrm{kg/m^3}\right)\left(0.005984\,\mathrm{m^3} - (10.001\,\mathrm{kg})/\left(2650\,\mathrm{kg/m^3}\right)\right)\right]} = 0.48$$

(where $\mathrm{V_{tot}} = \mathrm{V_c} + \mathrm{V_w}$), and the clay bonded to the sand grains in layers. This last assumption is based on the observations of Torfs (1995), Pangiatopolous et. al. (1997), and visual observation made during the laboratory portion of the present study. Torfs and

Panagiatopolous both commented on the homogeneity of the sand and clay mixtures used in their work. In this study it was observed, especially in the sand beds with very low fine fractions (0.2 and 0.4), that the beds looked to be made up of "dirty" or discolored sand. In other words, the clay could be seen with the naked eye to bond to the sand grains giving the beds the appearance that they were made up of a different colored sand.

It is interesting to note that the thickness of the clay layer (20 μm) at the minimum point of critical shear stress (τ_{cs}) is close to the size of the asperities (~ 20 μm) for a "rough" quartz surface (prepared using a No. 220 grit diamond wheel) as reported by Lambe and Whitman (1969) and as seen in Figure 4.21. This is precisely the point at which the transition from thin-film to boundary layer lubrication occurs.

A face-centered cubic structure with a sand grain having a diameter of 0.83 mm, a clay particle size of 1μm, and a fine grain fraction of 0.13, will have a clay layer approximately 40 μm thick and will consequently have approximately 94% of the interstitial pore space filled with clay. This calculation is given below:

$$V_{total} = \left(0.415\sqrt{8}\right)^3 = 1.62\text{mm}^3$$

$$V_{sand} = 4\left(\frac{4}{3}\right)\pi(0.415)^3 = 1.20\text{mm}^3$$

$$V_{clay} = 4\left(\frac{4}{3}\right)\pi\left[(0.415+0.04)^3 - (0.415)^3\right] = 0.38\text{mm}^3$$

$$\psi = \frac{2.65\text{x}10^{-6}(1-0.48)V_{clay}}{2.65\text{x}10^{-6}V_{sand} + 2.65\text{x}10^{-6}(1-0.48)V_{clay} + 1.00\text{x}10^{-6}(0.48)V_{clay} + 1.00\text{x}10^{-6}V_{pore}} = 0.13$$

$$\frac{V_{clay}}{V_{pore}} = 0.94$$

In this case, it is interesting to note that "space-filling" is occurring at a fine grain fraction of 0.13. This is an important point, since it implies that ψ_r (~ 0.13 for fresh kaolinite as shown in Figure 6.8), which is the point that the shear stress once again equals τ_{co} and the sediment starts to be dominated by the clay component (as can be seen in Figure 6.8), appears to be the space-filling fine fraction.

6.4 Shear Resistance Model for Clay Lubrication

Relative sliding between particles, which is the main mechanism causing deformation within the soil mass including at the sand bed surface, is determined largely by shear resistance at contacts between particles. Considering the force balance of Chapter 3 (Equation 3.3.2), this model seeks to explain the behavior of τ_{cr} through the change in shear resistance that accompanies a change in ψ.

For inter-particle shear resistance, which is frictional in nature, there are two basic laws (Amonton's laws): (1) shear resistance between two bodies is proportional to the normal force between the bodies, and (2) shear resistance between two bodies is independent of the dimensions of the two bodies. According to Lambe and Whitman (1969):

(1) On a submicroscopic scale most surfaces are actually rough, and consequently two solids will be in contact only where the asperities touch one another; i.e., actual contact is a very small fraction of the apparent contact area as may be seen in Figure 6.12.

(2) Because contact occurs at discrete sites, the normal stresses across these contacts are high, and even under light loading reach the yield strength of the material at these sites. Therefore, the actual area of grain-grain contact A_g is

$$A_g = \frac{N}{q_u} \tag{6.4.1}$$

where N, which is equivalent to P of the quasi-hydrodynamic model, is the normal load and q_u is the normal stress required to cause yield, i.e., plastic flow. Since q_u is fixed in magnitude, an increase in the total normal load between the two surfaces implies a proportional increase in the area of actual contact. This increase in area is a result of plastic flow of the asperities.

(3) The high contact stresses cause the two surfaces to adhere at the points of actual contact; i.e., the two bodies are joined by chemical bonds. Shear resistance is provided by the adhesive strength of these points. The maximum possible shear force $T_{\max}$ is

$$T_{\max} = sA_g \tag{6.4.2}$$

where s is the shear strength of the adhered junctions. Combining Equations 6.4.1 and 6.4.2 leads to

$$T_{\max} = N\frac{s}{q_u} \tag{6.4.3}$$

Since s and q_u are material properties, T_{max} is proportional to N.

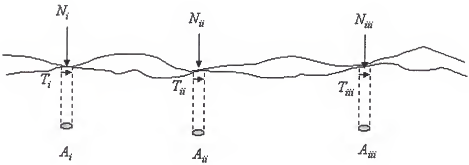

Figure 6.12 Microscopic view of frictional resistance.

While Equation 6.4.3 is appropriate for sand beds, it needs to be modified to include the effect of clay in pore water. Clay surfaces have irregularities not in the form of asperities, but in the form of step-like mesas and plateaus, and this fact combined with the size of the particles results in a different shear resistance behavior than that of sand grains. On clay surfaces, the steps are on the order of 10 - 100 Å compared to an asperity size of about 1000 - 10,000 Å for sand grains. Even when clay surfaces come into close proximity over almost their entire area, they may not come into direct contact. Foreign molecules on the surfaces, including sorbed water, are not squeezed out from between the surfaces unless the normal stress exceeds approximately 5.50 x 10^8 Pa. Rather, these foreign molecules participate in the transmission of the normal stress. Hence with clays, the normal stress is carried over much greater areas and is transmitted throughout the clay matrix rather than over a few asperities, as in the case with sand grains resulting in plastic deformation. This is the case even with fresh water flocculation (Figure 6.9), which results in an edge-to-face orientation that is more nearly similar to the asperity contacts discussed for granular particles, except that in the case of clays each contact probably contains only one asperity. However, because of the small size of the clay particles, the normal load is spread across several-fold more asperities than with the case of sand grains. Consequently, the load on each asperity is orders of magnitude smaller than with the case of sand grains. This is best illustrated with an example.

A sand grain contact is illustrated in Figure 6.13(a). The grains are assumed to be spheres and the diameter of the contact area between the two grains is given by (Lambe and Whitman, 1969)

$$d_{ca} = \left[\frac{12\left(1 - \nu^2\right)}{E} N \frac{R_1 R_2}{R_1 + R_2} \right]^{\frac{1}{3}} \tag{6.4.4}$$

which is simply an equation for the diameter of the contact area between two elastic spheres as derived by Lambe and Whitman (1969).

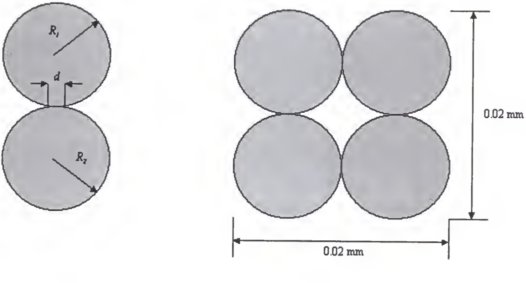

(a) (b)

Figure 6.13 Sand grain arrangement for calculation of shear resistance example.

In the above equation, the Poisson's ratio $\nu = 0.31$ for quartz, Young's modulus $E = 7.58 \times 10^{10}$ Pa for quartz, and R_1 and R_2 are the grain radii (which may be assumed equal). This equation is combined with Equation 6.4.1 to determine the average contact stress ($q_{avg} = N/A$) between two quartz spheres:

$$q_{avg} = \frac{N}{A} = \frac{4N^{\frac{1}{3}}}{\pi C_1^2 R^{\frac{2}{3}}} \tag{6.4.5}$$

where $C_1 = 0.0004\ (1/\mathrm{Pa})^{1/3}$. If we assume the grains are oriented in a cubic array such as in Figure 6.13(b), we need only consider a horizontal plane through the unit cell itself. From Figure 6.13 we note that there will be four contacts in a unit cell, and consequently the average contact stress will be one fourth of the average contact stress for a single contact

$$q_{avg} = \frac{N}{A_{tot}} = \frac{N^{\frac{1}{3}}}{\pi C_1^2 R^{\frac{2}{3}}} \tag{6.4.6}$$

where A_{tot} is the total contact area for the unit cell equal to four times the area of a single contact. Given that plastic yield for quartz occurs at a normal stress of 1.03×10^{10} Pa (Lambe and Whitman, 1969), Equation 6.4.6 can be used to determine the normal load and from it the confining stress needed to cause plastic yield:

$$N = \left(q_{avg} \pi C_1^2 R^{\frac{2}{3}} \right)^3 = \left[\left(1.03\mathrm{x}10^{10}\ \mathrm{Pa}\right) \pi C_1^2 \left(1.0\mathrm{x}10^{-5}\ \mathrm{m}\right)^{\frac{2}{3}} \right]^3 = 721\mathrm{g} \tag{6.4.7}$$

$$q = \frac{N}{A_{\mathrm{cell}}} = \frac{721\mathrm{g}}{\left(2.0\mathrm{x}10^{-5}\ \mathrm{m}\right)^2} = 1.8\mathrm{x}10^{12}\,\mathrm{Pa} \tag{6.4.8}$$

where q is the over-all confining stress applied over the area of the unit cell, A_{cell}.

If we now consider that each sphere is not perfectly smooth but contacts its neighbors on one asperity with a tip radius of 1000 Å, Equation 6.4.6 can again be used to determine the normal load and the confining stress that must be applied to cause plastic yield:

$$N = \left(q_{avg} \pi C_1^2 R^{\frac{2}{3}} \right)^3 = \left[\left(1.03\text{x}10^{10}\,\text{Pa}\right) \pi C_1^2 \left(1.0\text{x}10^{-7}\,\text{m}\right)^{\frac{2}{3}} \right]^3 = 33.2\,\text{g} \qquad (6.4.9)$$

$$q = \frac{N}{A_{\text{cell}}} = \frac{33.2\,\text{g}}{\left(2.0\text{x}10^{-5}\,\text{m}\right)^2} = 8.3\text{x}10^{10}\,\text{Pa} \qquad (6.4.10)$$

If we consider the dimensions of kaolinite, 1μm long x 0.1 μm wide x 0.01 μm thick, and assume the porosity (n_c) to be 0.48, we can determine the number of particles per unit volume

$$\text{V}_{\text{solid}} = (1 - n_c)\text{V}_t = 0.52\,\text{m}^3 \qquad (6.4.11)$$

$$\#\,\text{particles} = \frac{\text{V}_{\text{solid}}}{\text{V}_{\text{particle}}} = \frac{0.52\,\text{m}^3}{1.0\text{x}10^{-21}\,\text{m}^3} = 5.2\text{x}10^{20} \qquad (6.4.12)$$

The number of particles contacting a unit area may be assumed equal to (Lambe and Whitman, 1969)

$$\frac{\text{Number Particles}}{\text{Unit Area}} = \left(\frac{\text{Number Particles}}{\text{Unit Volume}} \right)^{\frac{2}{3}} \qquad (6.4.13)$$

$$\frac{\text{Number Particles}}{\text{Unit Area}} = \left(\frac{5.2\,\text{x}\,10^{20}}{1\text{m}^3} \right)^{\frac{2}{3}} = 6.47\,\text{x}\,10^{13} \qquad (6.4.14)$$

If we consider that each particle makes two stress-carrying contacts on a horizontal plane, we find that the number of contacts per unit area is twice the number of particles per unit area, or 1.29 x 10^{14}.

If we further consider each particle-particle contact with the edge to have a radius of 0.01 μm and that plastic flow starts at 6.9×10^9 Pa (Lambe and Whitman, 1969), these values can be used with Equation 6.4.6, to determine the confining stress that must be applied to cause plastic yield

$$N = \left[\left(6.9\text{x}10^{9}\,\text{Pa}\right) \pi C_1^2 \left(1.29\,\text{x}\,10^{14}\right) \left(1.0\text{x}10^{-8}\,\text{m}\right)^{\frac{2}{3}} \right]^3 = 1.25\,\text{x}\,10^{20}\,\text{g} \qquad (6.4.15)$$

$$q = \frac{N}{A_{\text{cell}}} = \frac{1.25\,\text{x}\,10^{20}\,\text{g}}{\left(2.0\text{x}10^{-5}\,\text{m}\right)^2} = 3.12\,\text{x}\,10^{26}\,\text{Pa} \qquad (6.4.16)$$

From this example it is seen that the normal load at a discrete contact, *N*, required to cause plastic yield increases significantly from the case where the overall confining stress is carried by a sand grain matrix in which the grains are modeled as spheres with 1000 Å asperities ($N = 33.2$ g as shown in Equation 6.4.9) to the case where the stress is carried by a kaolinite suspension with a porosity of 0.48 ($N = 1.25 \times 10^{20}$ g as shown in Equation 6.4.15).

Since the friction factor ($f = T_{\max}/N$) is inversely proportional to the normal load, this helps to explain the behavior illustrated in Figure 6.14. When $\psi = 0.0$, the confining stress, due to a normal load is carried completely by the sand matrix. The normal load at each discrete contact, as a result, is low (~ 33 g) and the friction factor is high ($f = 0.68$).

When $\psi \geq \psi_{\min}$, the confining stress is carried completely by the clay matrix. The normal load at each discrete contact is much higher ($\sim 1.25 \times 10^{20}$ g) and the friction factor, consequently, much lower ($f \sim 0.3$).

At low values of $\psi (< \psi_{\min})$, when assuming a face-centered cubic structure for the sand matrix it was shown in Section 6.3 that the clay layer is not thick enough to cover the asperities of the sand. As mentioned previously, a sand grain having a diameter of 0.83 mm, a clay particle size of 1μm, and a fine grain fraction of 0.066, will have a clay layer approximately 20 μm thick which is approximately the height of the asperities on rough quartz. Consequently, when $\psi < \psi_{\min}$ the over-all confining stress is carried by both the sand matrix and the clay suspension in between the sand grains.

As ψ increases from zero, more clay particles are added to the sand matrix and the clay increasingly shares the load carried by the sand particles, resulting in a decrease in the value of N for the sand grains. Considering Equations 6.4.1 and 6.4.2, it can be seen that this decrease in the normal load carried by the sand matrix will result in a decrease in the contact area between the sand grains, A_g, and a corresponding decrease in the maximum possible shear force, T_{max}, for the sand, which will in turn result in a decrease in the friction factor for the sand grains ($f = 0.15$).

With fresh water flocculation for kaolinite there is an increased number of edge-to-face contacts than with salt water flocculation, which results in a lower friction factor for the sediment beds with fresh water kaolinite. From Equation 6.4.15 it can be seen that the normal load is directly proportional to the number of contacts. Consequently, as shown in Figure 6.14, for a given value of ψ the friction factor for the fresh kaolinite will be less than the friction factor for the saline kaolinite. Also, this should lead to a greater difference between the two beds as ψ increases, because the clay suspension will have more of an influence on the behavior of the friction factor as it will carry more of the over-all confining stress.

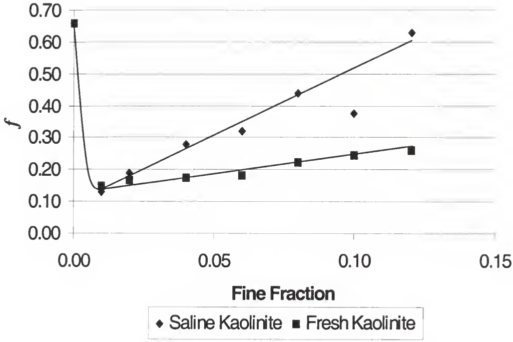

Figure 6.14 Plot comparing the results from the Schulze cell for the saline kaolinite and fresh kaolinite series of sand beds.

6.5 Comparison of Model Concepts

The two models are compared in Table 6.2, their strengths and weaknesses listed, to determine their relative merits.

Table 6.2 Comparison of model concepts

Model	Strengths	Weaknesses
Quasi-Hydrodynamic Model	• Effective in quantitatively predicting the behavior over the entire range of lubricating thickness. • Effective in explaining the behavior of the mixture once the sand grains are separated enough to have a clay layer between them.	• Focus is on the thin film and thick film regions of lubrication. • Does not provide a detailed explanation for the observed behavior in the boundary layer region of lubrication.

Table 6.2 (Continued)

Model	Strengths	Weaknesses
Shear Resistance Model	• Effective in explaining the behavior of the mixture when the sand grains are in contact or slightly separated.	• Focus is on the boundary layer region of lubrication. • Does not provide a detailed explanation for the observed behavior in the thin film and thick film regions of lubrication.

From Figure 6.8 it is seen that the quasi-hydrodynamic model predicts a value for $\psi_{\min}$ for kaolinite that is between 0.04 and 0.06. This value matches the $\psi_{\min}$ values obtained from the data for kaolinite beds of other researchers; the data from Torfs (1995) results in $\psi_{\min} = 0.02$, the data from Huygens and Verhofen (1996) results in $\psi_{\min} = 0.04$, and the data from Sharif (2002) results in $\psi_{\min} = 0.04$.

It is also noted that assuming a face-centered cubic structure for the sand grain matrix, $\psi_{\min}$ is the fine weight fraction at which the thickness of the clay layer is close to the size of the asperities of the sand grains (~ 20 μm) at which the transition from thin-film to boundary layer lubrication occurs.

From Figure 6.14 it is seen that the shear resistance model predicts $\psi_{\min} = 0.01$ for kaolinite. This value does not match well with the $\psi_{\min}$ values obtained from the data for kaolinite beds of other researchers 0.02-0.04. In addition, this value for $\psi_{\min}$ results in a clay thickness much less than the size of the asperities of the sand grains (~ 20 μm), as a sand grain having a diameter of 0.83 mm, a clay particle size of 1 μm, and a fine grain fraction of 0.01, will have a clay layer approximately 3 μm thick assuming the sand grains are organized in a face-centered cubic structure. It is also noted that the minimum friction factor (~ 0.15) occurs when the thickness of the clay layer is approximately 3 μm, from which it may be concluded that the strongest lubricating effect occurs when the over-all confining stress is carried by both the sand matrix and a thin clay suspension in between the sand grains.

Finally, it should be noted that ψ_{min} was not found to represent the space-filling weight fraction, contrary to the suggestion by Torfs et al. (2000). Assuming that sand grains are organized in a face-centered cubic structure, the sand grain diameter is 0.83 mm, and the clay particle size is 1 μm, it is not until the fine grain fraction reaches a value greater than 0.13 that the pore volume not occupied by clay becomes negligible (< 1% of the total volume). In other words, it is not until a fine fraction greater than 0.13 is reached that the clay suspension fills the entire volume of pore space within the sand unit cell. This is an important point, since it implies that ψ_r (~ 0.13 for fresh kaolinite as shown in Figure 6.8), which is the point that the shear stress once again equals τ_{co} and the sediment starts to be dominated by the cohesive component (as can be seen in Figure 6.8), appears to be the space-filling fine weight fraction.

CHAPTER 7
SUMMARY AND CONCLUSIONS

7.1 Summary

It was the goal of this study to develop an explanation for the effect of clay particles on the critical shear stress tcr for sand. To meet this goal the following tasks were carried out:

1. An expression, based on a force-balance for a sand grain at the surface of a bed, was developed for the critical shear stress of sand beds in the presence of interstitial clay particles, τ_{cr}, in the range of fine fraction, ψ, from 0.0 to 0.15.

2. A narrow, unidirectional flow flume with a false bottom designed for emplacing sediments beds, was used to determine the relationship of the critical shear stress of the sand beds as a function of clay weight fraction.

3. The expression for the critical shear stress of sand beds in the presence of interstitial clay particles was applied to the results from the flume tests to determine the effect of the fine grain fraction on the effective particle packing angle, Φ_{eff}.

4. A quasi-hydrodynamic model of clay lubrication, a mechanism of interstitial clay flow which possesses some features of hydrodynamic lubrication, was developed to explain the interaction between sand grains and the fine fraction.

5. A Schulze ring shear tester was modified for use with clays and then used to explain the behavior of τ_{cr} of sand at low values of ψ.

6. A shear resistance model, which relates to the nature of shear resistance between particles, was developed to explain the dependence of τ_{cr} on the fine grain fraction.

7.2 Conclusions

The following are the main conclusions of this study:

1. From the application of the expression for the critical shear stress τ_{cr}, of sand influenced by the presence of clay, τ_{cr} was shown to vary with the weight fraction ψ so that in the low range of ψ, τ_{cr}, tended to decrease from τ_{co} for pure sand to τ_{cs} at some $\psi = \psi_{\min}$. τ_{cr} then increased with a further increase in ψ, passing through the point where it once again equals τ_{co} at ψ_r.

2. It was determined that $\psi_{\min}$ is associated with the presence of clay particles. From tests on four different sediment beds, each with the same d_{50} (= 0.83 mm) and a different clay, $\psi_{\min}$ was found to vary from 0.020 to 0.060.

3. It was determined that $\psi_{\min}$ is less significantly affected by the sand size. From tests on four sediment beds, each with the same clay (kaolinite) and a different d_{50}, $\psi_{\min}$ was found to only vary from 0.045 to 0.060.

4. The quasi-hydrodynamic model for clay lubrication was found to explain the observed behavior of τ_{cr} with ψ. This model predicted a value for $\psi_{\min}$ for kaolinite (0.04) that matched the $\psi_{\min}$ values obtained from the data for kaolinite beds of other researchers; the data from Torfs (1995) resulted in $\psi_{\min} = 0.02$, the data from Huygens and Verhofen (1996) resulted in $\psi_{\min} = 0.04$, and the data from Sharif (2002) resulted in $\psi_{\min} = 0.04$. This result was explained through $\psi_{\min}$ being the fine weight fraction at which the thickness of the clay layer is close to the size of the asperities of the sand grains (~ 20 μm) at which the transition from thin-film to boundary layer lubrication occurs.

5. The shear resistance model for clay lubrication was found to offer an explanation for the observed behavior of τ_{cr} with ψ in the boundary layer region of lubrication. This model predicted a value for $\psi_{\min}$ (0.01) that did not match well with the $\psi_{\min}$ values obtained from the data for kaolinite beds of other researchers (0.02-0.04). This model failed because it predicted a value for $\psi_{\min}$ that resulted in a clay layer approximately 3 μm thick which is much smaller than the size of the asperities of the sand grains (~ 20 μm), and consequently in the boundary region of lubrication.

6. It was determined that ψ_r is the space-filling weight fraction and the point at which the behavior of τ_{cr} of the sand grain matrix starts to be dominated by the clay suspension. From tests on two sediment beds, each with the same clay (kaolinite) and the same d_{50} (= 0.83 mm), ψ_r was found to be the point at which the pore volume not occupied by clay becomes negligible (< 1% of the total volume).

7. Salinity was found to effect sand lubrication in the boundary region through changes in flocculation and in the thick-film region through changes in viscosity. Viscosity was found to increase from 0.040 Ns/m^2 to 1.60 Ns/m^2 as a result of addition of salt to pore water, and from 0.001 Ns/m^2 to 0.040 Ns/m^2 as a result of increase in the fine fraction.

8. It was determined that the shear resistance in the boundary region of lubrication was dramatically decreased with the presence of interstitial clay particles due to an increased number of load-carrying contacts. The normal load at a discrete contact, N, required to cause plastic yield was found to increase significantly from the case where the overall confining stress was carried by a sand grain matrix in which the grains were modeled as spheres with 1000 Å asperities (N = 33.2 g) to the case where the stress is carried by a kaolinite suspension with a porosity of 0.48 ($N = 1.25 \times 10^{20}$ g).

7.3 Recommendations for Future Work

The following recommendations are made for further work:

1. Consolidation of sediment beds composed of differing sand sizes and clay types needs to be conducted to determine the effect of consolidation on $\psi_{\min}$. Consolidation has been reported in several previous studies (e.g., Mehta and Partheniades, 1982) to dramatically effect the behavior of clay beds, and consequently has the potential to effect the behavior of $\psi_{\min}$ through changes in the clay fraction of sediment mixtures. All of the beds in this study were consolidated for a period of 72 hours before testing. In future work, beds of similar composition (sand grain size, clay type, and fine fraction) should be consolidated for varying time periods to determine if consolidation has an effect on the behavior of $\psi_{\min}$.

2. The two models for clay lubrication presented in this study give differing values for $\psi_{\min}$, and this discrepancy warrants further study. The quasi-hydrodynamic model for clay lubrication predicted a value for $\psi_{\min}$ for kaolinite of 0.04, and the shear resistance model for clay lubrication predicted a value for $\psi_{\min}$ for kaolinite of 0.01. A potential cause for this discrepancy is that while the dimensional analysis that leads to the Stribeck curve is reasonable for the "thick-film" lubrication regime where the grains are not in contact, it is quite possible that, in the lower region of the curve (the boundary layer lubrication regime) where the grain asperities become significant, other variables such as grain asperity size might become contributing factors. For example, if a modulus of elasticity, E, is used to represent the grain material strength (with units of stress) with the length scale of the grain asperities, d, then a potential additional dimensionless parameter incorporating the normal load per unit width, P, would be

$$\frac{E}{(P/d)}$$

which is a ratio of material strength to applied stress. In this ratio, an increase in the normal load per unit width would be equivalent to a decrease in the length of the asperities (both would increase the stress) or a decrease in the grain material strength for the same load. It would consequently be expected that lower values of this parameter would result in a more rapid transition to the "thick-film" regime of lubrication where the grain asperities play no role. If this were the case, a family of curves would be expected that should all converge to the thick-film curve for larger values of dimensionless viscosity (Figure 7.1), analogous to smooth turbulent flow where the resistance is governed only by viscosity and the roughness plays no role.

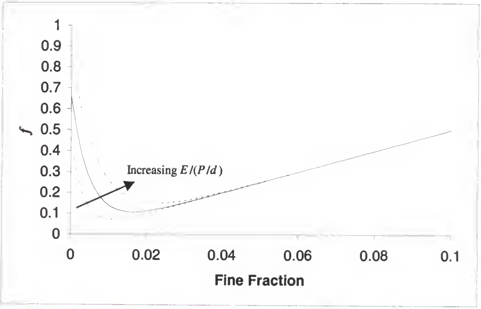

Figure 7. 1 Stribeck Curve with new dimensionless parameter.

Consequently, the application of various normal loads per unit width over beds with differing grain asperities needs to be conducted to determine the effect of normal load per unit width on ψ_{min}.

LIST OF REFERENCES

Ackers, P. (1993). Sediment transport in open channels: Ackers and White update. *Proc., Institution of Civil Engineers: Water, Maritime and Energy*, 101, 247-249.

Arulanandan, K., Sargunam, A., Loganathan, P., and Krone, R. B. (1973). Application of chemical and electrical parameters to prediction of erodibility. *Soil erosion: causes and mechanisms, prevention and control. Special Report 135*, D. H. Gray, ed., Highway Research Board, Washington, DC, 42-51.

Benedict, B. A., and Christensen, B. A. (1972). Hydrodynamic lift on a stream bed. *Symposium to Honor H. A. Einstein*, H. W. Shen, ed., Colorado State University, Fort Collins, 5, 1-17.

Chapuis, R.P., and Gatien, T. (1986). An improved rotating cylinder technique for quantitative measurement of the scour resistance of clays. *Canadian Geotechnical Journal*, 23(1), 83-87.

Christensen, B. A. (1965). Discussion of, "Erosion and deposition of cohesive soils by E. Partheniades". *Journal of the Hydraulics Division*, ASCE, 91(5), 301-308.

Christensen, B. A. (1972). Incipient motion on cohesionless channel banks. *Symposium to Honor Professor H. A. Einstein*, H. W. Shen, ed., Colorado State University, Fort Collins, 1-22.

Christensen, B. A. (1975). On the stochastic nature of scour initiation. *Proc., 15th Congress of IAHR*, 2, 65-72.

Coleman, N. L. (1981). Velocity profiles with suspended sediment. *Journal of Hydraulic Research*, 19(3), 211-229.

Croad, R.N. (1981). Physics of erosion of cohesive soils. Ph.D. Thesis, University of Auckland, New Zealand.

Dade, W. B., and Nowell, A. R. M. (1991). Moving muds in the marine environment. *Proc., Coastal Sediments '91*, Specialty conference, ASCE, New York, 54-71.

Dade, W. B., Nowell, A. R. M., and Jumars, P. A. (1992). Predicting erosion resistance of muds. *Marine Geology*, 105, 285-297.

Dyer, K. R. (1986). *Coastal and Estuarine Sediment Dynamics.* Wiley Interscience, Chichester, United Kingdom.

Dyer, K. R. (1989). Sediment processes in estuaries: future research requirements. *Journal of Geophysical Research*, 94(C10), 14327-14339.

Einstein, H. A. (1941). The viscosity of highly concentrated underflows and its influence on mixing. *Transactions, Twenty Second Annual Meeting of the American Geophysical Union, Hydrology Section*, 597-603.

Einstein, H. A. (1943). Flow on a movable bed. *Proc., Second Hydraulics Conference*, Iowa City, Bulletin 27, 332-346.

Einstein, H. A., and El Samni, E. A. (1949). Hydrodynamic forces on a rough wall. *Reviews of Modern Physics*, 21(3), 520-524.

Engelund, F., and Zhaohui, W. (1984). Instability of hyperconcentrated flow. *Journal of Hydraulic Engineering*, 101(3), 219-233.

Ganju, N, K., Barry, K.M., and Mehta, A. J. (2000). Performance report on the simulator of erosion rate function. *Technical Report TR-011*, Coastal and Oceanographic Engineering Program, Department of Civil and Coastal Engineering, University of Florida, Gainesville.

Guoren, D. (1981). The structure of turbulent flow in channels and pipes. *Scientia Sinica*, 24(5), 727-737.

Hayter, E.J. and Mehta, A.J. (1986). Modeling cohesive sediment transport in estuarial waters. *Appied Mathematical Modelling*, 10, 294-303.

Heshmat, H. (1991). The rheology and hydrodynamics of dry powder lubrication. *Tribology Transactions*, 34(3), 433-439.

Heshmat, H., and Brewe, D. E. (1996). Performance of a powder lubricated journal bearing with WS_2 powder: experimental study. *Transactions of ASME*, 118, 484-491.

Hinze, J. O. (1951). *Turbulence*. McGraw-Hill, New York.

Huygens, M., and Tito, L. (1994). Sediment transport of mixtures of cohesive and non-cohesive materials in sewer conduits. *Hydrosoft 5th International Conference on Hydraulic Engineering Software*, Porto Carras, Greece, 212-227.

Huygens, M., and Verhofen, R. (1996). Some fundamental particularities on partly cohesive sediment transport in a circular test flume. *Advances in Fluid Mechanics*, 9, 11-20.

Jinchai, P. (1998). A laboratory study of mud slurry discharge through pipes. Ph.D. Dissertation, University of Florida, Gainesville, Florida.

Keulegan, G. H. (1938). Laws of turbulent flow in open channels. *Research Paper 1151*, National Bureau of Standards, 21(6), 707-741.

Kramer, H. (1935). Sand mixtures and sand movement in fluvial models. *Transactions of ASCE*, 100, 798-873.

Lambe, T. W., and Whitman, R. V. (1969). *Soil Mechanics*. John Wiley & Sons, New York.

MacAnally, W.H. (2001). Aggregation and deposition of estuarial fine sediment. Ph.D. Dissertation, Department of Civil and Coastal Engineering, University of Florida, Gainesville, Florida.

Mantz, P. A. (1977). Incipient transport of fine grains and flakes by fluids: extended Shields diagram. *Journal of the Hydraulics Division*, ASCE, 103(6), 601-615.

Mehta, A.J. (1981). A review of erosion functions for cohesive sediment beds. *Proc., First Indian Conference on Ocean Engineering*, Indian Institute of Technology, Madras, India, 1, 122-130.

Mehta, A. J., and Lee, S. C. (1994). Problems in linking the threshold condition for the transport of cohesionless and cohesive sediment grain. *Journal of Coastal Research*, 10(1), 170-177.

Mehta, A. J., and Parchure, T. M. (1985). Erosion of soft cohesive sediment deposits. *Journal of Hydraulic Engineering*, 111(10), 1308-1326.

Mehta, A. J., and Parchure, T. M. (2000). Surface erosion of fine-grained sediment revisited. *Muddy Coast Dynamics and Resource Management*, B. W. Flemming, M. T. Delafontaine and G. Liebezeit, eds., Elsevier, Amsterdam, The Netherlands, 55-74.

Mehta, A. J., and Partheniades, E. (1979). Kaolinite resuspension properties. *Journal of the Hydraulics Division*, ASCE, 105(4), 409-416.

Migniot, C. (1968). E'tude des propiertes physiques de differents sediments tres fins et de leur comportment sous des actions hydrodynamiques. *La Houille Blanche*, 7, 591-620 (in French).

Miller, R.L., and Byrne, R.J. (1966). The angle of repose for a single grain on a fixed rough bed. *Sedimentology*, 6, 303-314.

Mitchener, H., and Torfs, H. (1996). Erosion of mud/sand mixtures. *Coastal Engineering*, 29, 1-25.

Moore, W.L., and Masch, F.D., Jr. (1962). Experiments on the scour resistance of cohesive sediments. *Journal of Geophysical Research*, 67(4), 1437-1449.

Munson, B.R., Young, F.Y., and Okiishi, T.H (1990). *Fundamentals of Fluid Mechanics*, 3rd edition, John Wiley & Sons, New York, NY.

Nalluri, C. and Alvarez, E.M. (1992). The influence of cohesion on sediment behavior. *Water Science and Technology*, 25(8), 151-164.

Nikuradse, J. (1933). Stromungsgesetze in rauhen rohren. *VDI Forschungsheft No. 361* (in German).

Ohtsubo, K., and Muraoka, K. (1986). Re-suspension of cohesive sediments by currents. *Third International Symposium River Sedimentation*, University of Mississippi, Oxford, 1680-1689.

Panagiotopoulos, I. Voulgaris, G., and Collins, M. B. (1997). The influence of clay on the threshold of movement of fine sandy beds. *Coastal Engineering*, 32, 19-43.

Parchure, T. M., and Mehta, A. J. (1985). Erosion of soft cohesive sediment deposits. *Journal of Hydraulic Engineering*, 111(10), 1308-1326.

Partheniades, E. (1965). Erosion and deposition of cohesive soils. *Journal of the Hydraulics Division*, ASCE, 91(1), 105-139.

Partheniades, E. (1977). Unified view of wash load and bed material load. *Journal of the Hydraulics Division*, ASCE, 103(9), 1037-1057.

Raudkivi, A. J. (1990). *Loose Boundary Hydraulics.* 3rd edition, Pergamon Press, Oxford.

Reichardt, H. (1938). Messungen turbulenter schwankungen. *Naturwissenschaften*, Berlin, Germany, 26, 404-421 (in German).

Reichardt, H. (1951). Vollstandige darstellung der turbulenten geschwindigkeitsverteilung in glattern leitungen. *Z. Angew. Math Mech.*, 31(7), 208-219 (in German).

Rijn, L. van (1984). Sediment transport (in 3 parts). *Journal of Hydraulic Engineering*: *Part I*, 110(10), 1431-1456; *Part II*, 110(11), 1613-1641; *Part III*, 110(12), 1733-1754.

Rossby, C. G. (1932). Conditions on kinematic similarity. *Massachusetts Institute of Technology Meteorology Papers*, 1(4), 9-14.

Schlichting, H. (1979). *Boundary-Layer Theory.* 7th edition, McGraw-Hill, New York.

Schulze, D. (1994). Entwicklung und anwendung eines neuartigen ringscherätes (Development and application of a novel ring shear tester), *Aufbereitungstechnik*, 35(10), 524-535, (in German and English).

Sharif, A. R. (2002). Critical shear stress and erosion of cohesive soils. Ph.D. thesis, SUNY Buffalo, NY.

Shields, A. (1936). Anwendung der ahnlichkeitsmechanik und der turbulenzforschung auf die geschiebebewegung. *Mitt. der Preuss. Versuchsanstalt für Wasserbau und Schiffbau*, Berlin, 26 (in German).

Shigley, J.E., and Mischke, C.R. (1989). *Mechanical Engineering Design*, 5th edition, McGraw-Hill, New York, NY.

Sutherland, A.J. (1967). Proposed mechanism for sediment entrainment by turbulent flows. *Journal of Geophysical Research*, 72, 6183-6194.

Szeri, A. Z. (1998). *Fluid Film Lubrication: Theory and Design.* Cambridge University Press, New York.

Taki, K. (2000). Critical shear stress for cohesive sediment transport. *Coastal and Estuarine Fine Sediment Transport Processes*, W. H. McAnally and A. J. Mehta, eds., Elsevier, Amsterdam, 53-61.

Torfs, H. (1995). Erosion of mud/sand mixtures. Ph.D. Thesis, Catholic University of Leuven, Leuven, Belgium.

Torfs, H., Jiang, J., and Mehta, A. (2000). An assessment of erodibility of fine/coarse sediment mixtures. *Coastal and Estuarine Fine Sediment Transport Processes*, W. H. McAnally and A. J. Mehta, eds., Elsevier, Amsterdam, 109-123.

Vanoni, V. A. (1946). Transportation of suspended sediment by water. *Transactions of ASCE*, 111, 67-133.

Vanoni, V., and Brooks, N. (1957). Laboratory studies of the roughness and suspended load of alluvial channels. *Report E-68*, California Institute of Technology, Pasadena, California.

Wasp, E. J., Kenny, J.P., and Gandhi, R.L. (1977). *Solid Liquid Flow Slurry Pipeline Transportation. Trans Tech Publications*, Clausthal, Germany.

Wiberg, P. L., and Smith, J. D. (1987). Calculations of the critical shear stress for motion of uniform and heterogeneous sediments. *Water Resources Research*, 23(8), 1471-1480.

Yalin, M. S. (1972). *Mechanics of Sediment Transport*. Pergamon, New York.

BIOGRAPHICAL SKETCH

Kevin Barry was born on June 2, 1966, in Augusta, Georgia. He graduated from the United States Military Academy and received his Bachelor of Science degree in chemical engineering in 1989. After graduation, he worked as a cavalry officer in the United States Army during which time he participated in both Operation Desert Shield and Operation Desert Storm, and was awarded a Bronze Star for his achievements in these operations. Upon retiring from the Army in 1991, he attended the Georgia Institute of Technology where he designed the hand-held torch for the 1996 Summer Olympic Games in Atlanta, Georgia. He graduated from Georgia Tech in 1995 and received his Master of Science in mechanical engineering. After graduation, he entered the University of Florida to study in the Civil and Coastal Engineering Department. After these years of study, he earned the Doctor of Philosophy degree, and looks forward to contributing his newly acquired knowledge to serve his country.

I certify that I have read this study and that in my opinion it conforms to acceptable standards of scholarly presentation and is fully adequate, in scope and quality, as a dissertation for the degree of Doctor of Philosophy.

AJMehta

Ashish J. Mehta, Chair
Professor of Coastal and Civil Engineering

I certify that I have read this study and that in my opinion it conforms to acceptable standards of scholarly presentation and is fully adequate, in scope and quality, as a dissertation for the degree of Doctor of Philosophy.

Robert G. Dean

Robert G. Dean
Graduate Research Professor of Coastal and Civil Engineering

I certify that I have read this study and that in my opinion it conforms to acceptable standards of scholarly presentation and is fully adequate, in scope and quality, as a dissertation for the degree of Doctor of Philosophy.

Hanes

Daniel M. Hanes
Professor of Coastal and Civil Engineering

I certify that I have read this study and that in my opinion it conforms to acceptable standards of scholarly presentation and is fully adequate, in scope and quality, as a dissertation for the degree of Doctor of Philosophy.

Clay L. Montague

Clay L. Montague
Associate Professor of Environmental Engineering Sciences

I certify that I have read this study and that in my opinion it conforms to acceptable standards of scholarly presentation and is fully adequate, in scope and quality, as a dissertation for the degree of Doctor of Philosophy.

Robert J. Thieke
Assistant Professor of Coastal and Civil Engineering

This dissertation was submitted to the Graduate Faculty of the College of Engineering and to the Graduate School and was accepted as partial fulfillment of the requirements for the degree of Doctor of Philosophy.

May, 2003

Pramod Khargonekar

Pramod P. Khargonekar
Dean, College of Engineering

Winfred M. Phillips
Dean, Graduate School